Embedding Optical Sensors Within Additive Manufactured High Melting Point Metals for Condition Measurement Within Harsh Environments

A dissertation submitted for the degree of Doctor of Philosophy

Benjamin Michie

Heriot-Watt University
School of Engineering and Physical Sciences

February 2023

Abstract

The use of optical fibre sensors, such as fibre Bragg gratings (FBG), provides opportunity for condition health monitoring of a structure or process. FBGs allow for in-situ measurement of temperature and strain. The measurement of these parameters is important for advanced and complex structures where these sensors can provide real-time information to support lifetime condition monitoring.

In general, sensor reliability drops as the temperature, moisture content and environmental corrosiveness increases. These limitations can be overcome by embedding sensors in high melting point metals to extend their operation for use at elevated temperatures and within harsh environments.

A fibre embedding process chain has been devised to facilitate embedding of optical fibres within additive layer manufactured (ALM) stainless steel (SS) components. The ALM process provides access to any point of the component during manufacture, which is beneficial for the embedding of sensors inside a functional component. Furthermore, parts with complex geometries and internal features, unattainable with other forms of manufacture, become feasible using ALM technologies, but pose additional challenges for accurate modelling and external monitoring. Embedding sensors directly into such structures is a possible solution to this challenge.

Selective laser melting is a powder bed fusion ALM technique where a laser selectively melts metallic powder in accordance with the geometrical data of the build layer, defined by a 3D model. The small spot sizes achievable by selective laser melting (SLM) systems are well suited for fibre embedding as the localised melt pools limits interaction through conduction with the surrounding material. A system has been set up for use with SS-316 powder, that is capable of embedding fibres in test structures. The high nickel content within SS-316 allows for intermixing of the host material with the fibre protective nickel jacket thereby bonding the fibre to the surrounding material.

The work of this thesis defines process parameters suitable for repeatable and reliable embedding of FBG sensors inside SS-316 coupons. 5µm thick Cr layers are deposited onto lengths of stripped optical fibres containing FBGs using the RF sputter deposition system (RF power 100W, deposition time 30mins, processing pressure 4×10^{-4}mBar). This is followed by a ≥300 µm Ni coating using the developed Ni plating system (current density 2-7 A/dm^2, voltage 30V max, plating time ≥16hrs). The SLM build parameters for building SS-316 coupons (100W Laser power, 300mm/s scanning velocity, 60µm hatch spacing, 200µs pulse duration, 1kHz modulation frequency and scan orientation rotated by 90° between layers) and the modified build parameters for the embedding process (90W laser power, 300mm/s scan velocity, 100µm hatch spacing, 200µs pulse duration, 1kHz modulation frequency and a scan orientation parallel to fibre profile) are defined with respect to optimisation of the available equipment for fibre embedding procedures.

Acknowledgements

I would like to express my thanks to Dr Bill MacPherson for his continued academic support, supervision, and guidance throughout the project. I am extremely grateful to the time he has dedicated to me and my research project.

I would additionally like to thank my industrial supervisors Dr Simon Brooks and Dr Matthew Kingston for their support and input, and Dr Robert Maier who initiated the project and gave me the opportunity to conduct the research.

Lastly, I would like to thank the members of the Applied Optics and Photonics research group and all associated technical and support staff.

Research Thesis Submission

Please note this form should be bound into the submitted thesis.

Name*:*	**STUDENT NAME Benjamin J Michie**		
School:	**STUDENT SCHOOL Engineering and Physical Sciences**		
Version: *(i.e. First, Resubmission, Final)*	**FINAL**	Degree Sought:	**PHD**

Declaration

In accordance with the appropriate regulations I hereby submit my thesis and I declare that:

1. The thesis embodies the results of my own work and has been composed by myself
2. Where appropriate, I have made acknowledgement of the work of others
3. The thesis is the correct version for submission and is the same version as any electronic versions submitted*.
4. My thesis for the award referred to, deposited in the Heriot-Watt University Library, should be made available for loan or photocopying and be available via the Institutional Repository, subject to such conditions as the Librarian may require
5. I understand that as a student of the University I am required to abide by the Regulations of the University and to conform to its discipline.
6. I confirm that the thesis has been verified against plagiarism via an approved plagiarism detection application e.g. Turnitin.

ONLY for submissions including published works

Please note you are only required to complete the Inclusion of Published Works Form (page 2) if your thesis contains published works)

7. Where the thesis contains published outputs under Regulation 6 (9.1.2) or Regulation 43 (9) these are accompanied by a critical review which accurately describes my contribution to the research and, for multi-author outputs, a signed declaration indicating the contribution of each author (complete)
8. Inclusion of published outputs under Regulation 6 (9.1.2) or Regulation 43 (9) shall not constitute plagiarism.

* *Please note that it is the responsibility of the candidate to ensure that the correct version of the thesis is submitted.*

Signature of Candidate:	BMichie	Date:	**01/02/2023**

Submission

Submitted By *(name in capitals):*	BENJAMIN J MICHIE
Signature of Individual Submitting:	BMichie
Date Submitted:	**01/02/2023**

For Completion in the Student Service Centre (SSC)

Limited Access	Requested	Yes		No		Approved	Yes		No	
*E-thesis Submitted (**mandatory for final theses)***										
Received in the SSC by *(name in capitals):*						Date:				

Inclusion of Published Works

Please note you are only required to complete the Inclusion of Published Works Form if your thesis contains published works under Regulation 6 (9.1.2)

Declaration

This thesis contains one or more multi-author published works. In accordance with Regulation 6 (9.1.2) I hereby declare that the contributions of each author to these publications is as follows:

Please included additional citations as required.

Table of Nomenclature

Symbol	Meaning
n	Refractive index
θ_c	Critical angle
θ_i	Angle of incidence
λ	Wavelength
λ_B	Bragg Wavelength
Λ	Grating Period
$\lambda_{incident}$	Wavelength of incident light
$\Delta\lambda$	Bragg wavelength shift
α	Thermal expansion coefficient
ε	Applied strain
p_e	Photoelastic coefficient
p_{nn}	Photoelastic contributions
ζ	Thermo-optic coefficient
p_{11}, p_{12}	Pockels coefficients
ε_{zz0}^{s}	Axial thermal strain
ε_{rr0}^{s}	Radial thermal strain
Q	Energy
T	Temperature
c_p	Specific heat capacity
ρ	Density
V	Volume
d	Diameter
t	Time
P	Power
T_m	Material melting temperature
H_m	Melting enthalpy
v	Speed
E	Energy density
h	Hatch spacing
w	Layer thickness
O	Overlap index
s_t	Step over distance
R_a	Average profile surface roughness
R_t	Maximum peak to valley height
R_z	Mean peak to valley height
S_a	Average surface roughness
A	Area
R	Resistance
ρ_R	Resistivity
m	Mass

M	Atomic weight
F	Faraday's constant
n_e	Number of electrons
a	Cathode current efficiency
ρ	Density
s	Average coating thickness
ω	Frequency of AC field
μ	Relative magnetic permeability
δ	Depth of heating

Table of Acronyms

Acronym	Meaning
FBG	Fibre Bragg Grating
ALM	Additive Layer Manufacturing
SS	Stainless Steel
SLM	Selective Laser Melting
CAD	Computer Aided Drawing
LOM	Laminated Object Manufacturing
FFF	Fused Filament Fabrication
FDM	Fused Deposition Modelling
SL	Stereolithography
DLP	Digital Light Processing
SLS	Selective Laser Sintering
TIR	Total Internal Reflection
UV	Ultraviolet
OSA	Optical Spectrum Analyser
Ni	Nickel
RF	Radio Frequency
Cr	Chromium
WDM	Wavelength Division Multiplexing

Table of Contents

Chapter 1 - Introduction

Surface mounted sensors are often used for failure prevention schemes by sensing external stimuli within components and high-risk processes. These forms of sensors typically operate as point-based sensors which are capable of reporting an accurate reading for a region within the immediate vicinity of the sensor.

With the advent of 3-dimensional (3D) component printing, it is now possible to manufacture highly complex shapes with properties that can vary throughout the structure, and therefore there is a need to be able to monitor conditions inside structures to fully understand them. Encapsulating the sensor inside a functional component, or part, aids in extending the operational boundaries of the component and provides a more accurate representation of sensed stimuli in comparison with surface measurement and inferring the internal conditions.

Various types of sensor and embedding techniques exist, [1, 2, 3, 4], but few are applicable for the operational requirements of providing accurate condition measurement within harsh environments, corrosive atmospheres and at elevated temperatures ($>200℃$), in the presence of electromagnetic interference. These specific requirements set the foundations of this project, defining a sensor embedding process that can be taken forward into commercial manufacture (repeatable batch manufacture of embedded sensors) for the purpose of embedding optical sensors within high melting point metals with the desired end goal of achieving embedded sensor networks within high melting point ($\sim 1400℃$) metals that retain reliable operation within harsh environments while remaining immune to electromagnetic interference.

1.1 Motivation

It is part of human nature to learn from failure. It is what drives our collective development as a species. If one were to view human history through the lens of engineering, you would find development succeeds failure at all turns. It takes a suspension bridge to collapse for engineers to learn to compensate for wind in its design [5]. A gas explosion leads to an understanding of the susceptibility of underground iron pipes to the propagation of cracks, leading towards catastrophic fracture [6]. Entire fleets have sunk because ship designs did not cater for turbulent seas [7].

As is often the case in such events, the only point of blame is a simple lack of understanding. Engineers can only accommodate for what collective society understands about the physical world. After each failure event, society learns and develops with the aim of preventing repetition. To some, this learning from failure is a necessary risk. But as scientific and engineering understanding has developed we increasingly see systems in which consequences of failure are beyond acceptable. This is due to the high severity and cost of failure in advanced systems. A potential solution to mitigate against this is to incorporate real-time structural health monitoring during operation. Being able to determine component properties in situ allows for the early detection of operational conditions that may lead to failure.

As the scale of catastrophe rises, so does our ingenuity to prevent it. We manufacture robots to venture into places too dangerous for humans [8]. Create smart materials that can sense like human skin [4], providing real time condition measurement of processes and environment to allow remediation before actual component failure [9]. Creating such 'Smart' components requires them to be instrumented in a way to allow them to sense their environment and its effect on the component. To accomplish this capability within inanimate objects, we use sensors.

Sensors have existed since humans first poked their fingers into a fire and realised it was hot. They now allow us to determine a wide range of environmental conditions such as temperature, pressure, strain, moisture content and the gas constituents of an atmosphere. Modern sensors commonly use electricity or the propagation of light as a sensing medium.

Electrical sensors have seen many decades of development, and for most sensing applications remain a highly competitive solution. But conventional sensing techniques have their limitations. The applicability of electrical sensors degrades in applications involving electromagnetic fields and high temperatures [10]. Optical sensors are comparatively new compared to their electrical counterparts and typically see application in situations where electrical sensors may be unsuitable, such as within high temperature, situations requiring contactless sensing and applications requiring non-conductive sensors. Further to this, they can be lightweight, retain small form factor, and can be multiplexed into distributed sensor arrays. But their reliability drops as the temperature, moisture content and environmental corrosiveness increases [11], albeit with better performance within these regimes than their electrical counterparts.

A method for extending the operational capabilities of optical sensors is to embed them inside high melting point metals. This extends the useful temperature range while providing protection against corrosive environments [12]. This promotes the ability to provide in situ condition measurement within harsh environments, an important facet for supporting lifetime condition monitoring of advanced, complex structures and implementing failure-prevention schemes within high-risk processes.

1.2 Applications

By design, optical sensors are electrically insulated and are considered less susceptible to electromagnetic interference than electrical sensors. This promotes applications within sensor arrays within complex systems inducing electromagnetic fields. This is due to the low optical loss within optical sensors allowing for relatively long connection leads with minimal electrical noise pick up, which allows for extended sensor networks within these applications. For example, surface mounted and embedded Fibre Bragg Gratings (FBG) can be used in place of electrical strain gauges for structural health monitoring and failure diagnostic applications [13].

Successful embedding of optical sensors to date relates to using composites and plastics as the host material. These are only suited for low temperature applications, typically below 200°C [14]. However, embedding sensors within high melting point metals requires the sensor element to survive the higher temperatures associated with the embedding process. While such embedded sensors may still be used for low temperature sensing applications, it is the embedding process itself that poses new challenges, specifically within ALM manufactured metallic components because here the sensor must survive temperatures required to melt metal. Embedding optical sensors within high melting point metals, such as SS, extends their operation to applications outside of their operational capability without embedding. This is vital for implementing failure prevention schemes and providing lifetime condition monitoring within high-risk processes.

Embedded sensors allow determination of changes inside complex structures induced by external parameters. The use of FBGs as sensor elements holds the prospect of forming multi-sensor sensing networks. This offers benefits for achieving a better understanding of component parameters by making multiple measurements across an entire surface or through a component's internal structure.

1.3 Challenges

The use of embedded FBGs within polymers and ceramics for structural health monitoring is widely documented in literature [1, 4, 15, 16]. However, embedding materials such as polymers are unsuited for high temperature applications exceeding 200°C [14]. Ceramic materials are suitable for higher temperature applications, but difficulties arise for embedding optical sensors, as high temperature processes (typically above 1200°C) are required to produce fully dense ceramic parts, [3], which is approaching the glass transition temperature of fused silica glass [17].

Embedding within high melting point metals extends the operational temperature range of optical sensors, [18], but introduces new challenges. Optical fibres are susceptible to damage within any embedding process involving molten metal as temperatures may exceed the glass transition temperature of fused silica glass ($\approx 1700°C$) [17]. Further challenges to the embedding process arise from the thermal expansion coefficient mismatch between the bulk metal and the optical fibre. This can result in poor bonding of the fibre to the surrounding material that in turn reduces the accuracy for strain sensing due to poor or unreliable strain transfer. It also has implications for applications requiring a hermetic bond.

Conventional embedding techniques for high-melting point metals, such as welding and sintering, have limitations in terms of part access and process interruption for sensor placement inside of the bulk material [2]. Further, such metal forming process would require the sensor to be subject to high temperatures for extended periods of time. ALM manufactured metallic components using laser-based manufacturing techniques significantly reduce the heating time required to melt metals, while allowing for access to the part at any point of the manufacturing process, a useful feature for sensor embedding procedures, [1].

Defining a reliable process for fibre embedding in ALM components poses additional challenges as it requires the successful operation of multiple subprocesses to be conducted successfully. These processes relate to the ALM of metallic components, fibre metallisation, dissimilar joining processes and sensor calibration and testing procedures. Each of these steps introduces risk of sensor damage which must be understood and mitigated in order for the process to be repeatable and reliable.

1.4 Thesis Outline

The following thesis will start with a literature and background review in order to understand the current state of the art when it comes to embedding optical fibre sensors within metallic components for the purpose of condition measurements within harsh environments. This review will be used to gain an understanding of complications of achieving successful sensor embedding and also define a fibre embedding process chain in order to achieve it successfully within the project parameters (timescales, budget and availability of equipment).

Following the literature and background review, the thesis is split into chapters following sequentially through the fibre embedding process chain, initiating with developing and categorizing a selective laser melting (SLM) system for use with SS-316 powder, see Chapter 3, and characterisation of process parameters in order to achieve suitably dense parts with low surface roughness. This will be followed by chapters detailing the relevant investigations and systems required for fibre metallisation and protection, see Chapter 4. This is achieved first by depositing a uniform conductive thin film ($\approx 5\mu m$) of chromium onto a fused silica fibre, see Chapter 4 Section 2. This conductive coating is then used as a seed layer for electroplating a protective nickel jacket onto the fibre, which will be achieved by the design, development and calibration of a nickel electroplating system capable of depositing a 350-500μm thick uniform nickel coating onto a 130μm chrome-coated fibre, see Chapter 4 Section 3.

The fibre metallisation process is followed by fibre embedding investigations that require all of the above analysis in order to be conducted, see Chapter 5. Once this process is defined, the same embedding procedure is used for embedding FBGs within SS-316 coupons, for the primary purpose of temperature sensing within the required operational temperature range ($-10℃ - 180℃$). Following on from this, the feasibility of incorporating dissimilar metal joining processes such as brazing into the embedding process was also investigated, see Chapter 6.

The success of the entire fibre embedding process chain will be achieved by conducting extensive testing of FBGs embedded inside SS-316 coupons, consisting primarily of elevated and extended temperature cycling experiments, see Chapter 5 Section 3. This will allow for the correlation of the grating sensitivity, which can be used for temperature correlation within operation while ensuring the applicability for using the embedded FBGs within the projected operational temperature range. Finally, further work will be discussed which could extend the project further towards the goal of achieving an embedded distributed sensing networks capable of temperature and strain discrimination, with the view of achieving strain measurements using the embedded assembly and developing a reliable and repeatable process that can be taken forward into commercialisation.

Chapter 2 – Literature Review and Background

Developing an embedding process for the purpose of producing instrumented additive manufactured metallic components requires an understanding of optical fibres, optical sensors, and ALM fabrication. Current literature describing the embedding of fibre sensors for use in high temperature applications, different sensor types and embedding processes, materials and design requirements is discussed. The design of a process to facilitate ALM embedding is considered as well as processes and process parameters of relevance for the purpose of embedding optical sensors within high melting point metals for use in corrosive or high temperature environments.

2.1 Additive Layer Manufacturing

ALM technologies relate to manufacturing processes that build up three-dimensional parts by the deposition of sequential two-dimensional layers. Historically, they are used for rapid prototyping, but have since developed to be capable of producing fully functioning components for industrial applications.

2.1.1 Technology Overview

ALM technologies allow for complex geometries and internal features which would be otherwise difficult or unattainable to manufacture using traditional machining approaches. This approach also has the benefit of being able to access the internal structure during the build, thereby facilitating the insertion of sensing elements inside the structure. The use of computer aided drawing (CAD) allows for designers to visualise the full form and functionality of components prior to printing, while additionally retaining all the necessary geometrical information required for the ALM process to be conducted. As the process can be entirely automated, manufacturing mistakes in account of human error are mitigated entirely, so long as suitable care is taken within the pre-manufacturing process steps and component design.

All ALM technologies retain commonalities in terms of manufacturing components on a layer-by-layer basis and the requirement of pre-manufacture preparation steps. These steps are typically the creation of a three-dimensional virtual model, setting the process parameters depending on the technique in use, and the division of the 3D model into two-dimensional “slices” of a defined layer thickness. Most of these parameters are considered with respect to the ALM technique and material to be used for manufacture.

2.1.2 Material Types and Build Considerations

ALM technologies can be differentiated by their material type and form. For instance, different technologies are used depending on whether the starter material is in solid, liquid or powdered state. Solid form technologies often involve the gluing together of solid materials or the melting and extrusion of a solid material. Manufacturing techniques within the branch of ALM include laminated object manufacturing (LOM), fused filament fabrication (FFF) and fused deposition modelling (FDM) and are typically the most common 3D printing technologies available [19].

ALM techniques using liquid pre-cursor materials, typically photosensitive resins, and involve the polymerization of liquid photopolymer materials, often photocuring the resin into the desired form. Common approaches include stereolithography (SL) and digital light processing (DLP).

Powder based ALM techniques use powdered material deposited in a thin layer before a binding, sintering or melting process is used produce the desired part via a layer-by-layer process. This includes techniques such as selective laser sintering (SLS) and selective laser melting (SLM) [19, 20]. This technique has benefits above and beyond other ALM processes as it opens up the possibility of fabricating metal components. Metal components have application in a range of industrial sectors, such as medical and defense, while aiding the perceptive change in using ALM for visualisation tools to the production of fully functional industrial components.

To date, no single ALM technique can be used for all material types or forms and therefore, they can be further differentiated by the type of form material with systems typically based on a single 3D printing technique, using one type of material. Traditionally, the most common materials used for ALM are polymers (including photosensitive resin), polyamide, polystyrene, acrylic, wax, and thermoplastics such as ABS and polycarbonate. Polymers such as polycarbonate and ABS are suited for FFF and FDM based ALM techniques, while photosensitive resins are suited for SL and DLP based techniques [19].

As ALM technologies advance, so to do the applicability of other materials such as ceramics, composites and metals. Ceramics find their place within FDM and SLM techniques. Composites are often used for LOM and FDM based techniques, while metallic materials are typically unique to SLS and SLM processes [19, 20].

While many ALM technologies can be used for embedding sensors, such as FDM using polymer form materials, this thesis is specifically looking into the embedding of optical sensors within high melting point metal additive layer manufactured components. Therefore, metallic based ALM techniques such as SLS and SLM are most relevant to this work.

2.2 Optical Fibres Principle of Operation

In essence, optical fibres are non-conducting cylindrical waveguides. They typically consist of a light guiding core surrounded by a cladding of lower refractive index that constrains the light in the core region, Figure 1. The most common types of optical fibres are single-mode and multi-mode fibres. Single-mode optical fibres typically have a small core ($\sim 8\mu m$) and are designed to propagate a single monochromatic beam of light, Figure 1(a) . Multi-mode optical fibres have a larger core diameter ($> 50\mu m$), allowing them to propagate more than one ray of light Figure 1(b). a first approximation, this guiding light can be explained through the mechanism of total internal reflection (TIR) [21]. TIR occurs when light propagating through an optically dense material is incident on a boundary of a material with a lower refractive index, as illustrated in Figure 2. If light is incident at an angle larger than the threshold condition defined by equation (1), derived from Snell's law, the light is reflected back into the optically denser medium with negligible loss [22].

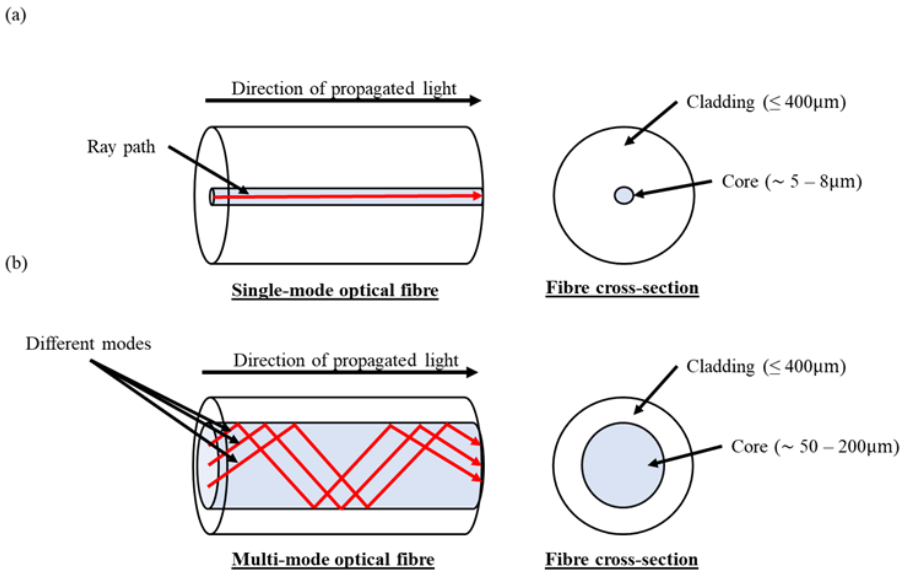

Figure 1 - Cross section of (a) single-mode and (b) multi-mode optical fibres illustrating the ray paths inside the core and typical dimension ranges.

$$n_1 sin\theta_c = n_2 sin90° \quad (1)$$

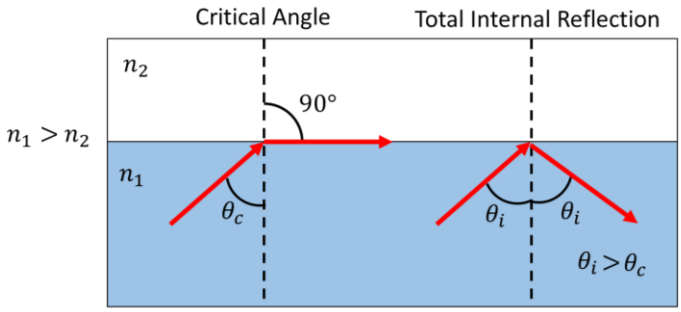

Figure 2 - Principle of total internal reflection. Angles of incidence (θ_i) greater than the critical angle (θ_c) will be totally internally reflected at the interface between the two media.

For light propagating through an optical fibre, this provides a simple model that can be used to understand the light guiding mechanism. TIR will occur at the boundary of the core and the cladding if the refractive index of the core is greater than that of the cladding and the angle of incidence is greater than the critical angle. In terms of optical fibres, this relates to the function of refractive indices within the cladding and core, the acceptance angle, the sine of which is the numerical aperture [23].

2.2.1 Mechanical and Optical Properties of Optical Fibres

Optical fibres are widely used within the telecommunications industry due to optical communication networks requiring a high data bandwidth and low propagation loss over long distances in comparison to electrical based transmission. Optical fibres are typically manufactured using fused silica glass due to significantly lower losses than polymer fibres (typically less than 1dB/km for single mode fibres, compared to 50-100dB/km for polymer fibres [24]) which exhibit larger material attenuation leading to lower data rate and limitations within long distance transmission [25]. Benefits of fused silica relate to its highly developed and commercialised manufacture and low thermal expansion coefficient that is well suited to being subject to rapid temperature changes, without detrimental features such as cracks occurring on the fibre surface. Further, the drawing process results in good surface finish that is protected by a compliant polymer, shielding it from damage [22]. Fibre strength is inversely proportional to crack size, so mitigating their occurrence is important for successful fibre operation [22].

Light attenuation in fused silica is caused by absorption in the ultraviolet and infrared regions due to electronic transitions and molecule excitation respectively, and loss due to Rayleigh scattering [22]. The lowest absorption losses for fused silica fibres occurs at an operational wavelength of 1.5µm, which is why long-haul optical communications links commonly operate around this wavelength [22].

Most commercial optical fibres are specified for use in operating temperatures between -60 and 85°C, and exposure to high process temperatures may directly affect the mechanical strength of optical fibres [11]. Fused silica fibres are limited to temperature applications up to around 1000°C as temperatures beyond this value promote discontinuities in the fibre's form and structure as temperatures approach the softening point of fused silica glass (≥1200°C) [26]. Other dielectric materials that can be used to fabricate optical fibres can provide desirable characteristics that outperform fused silica, depending on the application [22]. Sapphire is transparent for wavelengths extending from the ultraviolet region to the infrared region of the light spectrum. Furthermore, it is significantly more durable than silica and retains a higher melting temperature, extending fibre operation into high temperature and high-power applications, [22, 27]. Busch et al., 2009, developed a process for manufacturing Bragg gratings within single-crystal sapphire optical fibres. These gratings retained high thermal stability for temperatures up to 1745°C [28], which is a significant increase when compared to the temperatures capable of fused silica fibre sensors [29]. For applications within elevated temperatures and harsh environments, sapphire derived optical fibres are of interest as an alternative fibre material to fused silica. However, these types of fibre are not single mode, which make sensing applications more difficult, are significantly more expensive than fused silica fibres and are not provided in long lengths reducing their operational viability.

2.3 Sensor Types for In-situ Condition Measurement

Sensors are devices that are sensitive to one or more external stimuli and produce a signal that alters in a known and repeatable manner with respect to the changing parameter(s). They come in a variety of forms and configurations for the purpose of condition measurement, allowing for the measurement of parameters such as temperature, strain, pressure and the constituent components of an atmosphere or environment. Furthermore, they allow investigations into such parameters to be conducted outside of the limitations of human safety or convenience. This is important for incorporation into failure prevention mechanisms and condition monitoring within harsh environments. The two primary sensor types used for this type of measurement are electrical and optical sensors.

2.3.1 Electrical Sensors

An electrical sensor is a device that translates a physical parameter, such as temperature or strain (using a thermocouple or strain gauge) into an electrical signal that can be in the form of charge, current, frequency or voltage. They come in many forms and varieties, but their operation is typically achieved via either passive or active sensing, as explained in the following.

Passive electrical sensors do not require any additional energy to function and produce an electrical signal based on external stimuli, directly converting input energy into output energy. This dictates that they can only be used for sensing when naturally occurring energy is available. For instance, a light sensor changes resistance when the intensity of light changes and a piezo sensor generates a voltage under an applied pressure. Examples of such sensors include thermal (thermocouples), infrared, electric field and chemical sensors.

By contrast, active sensors provide their own energy source for sensing purposes. The sensor emits energy, such as electromagnetic radiation, which is directed towards a target that is to be investigated. This radiation is then reflected back from the target and measured by an appropriate detector. These types of sensors have applications within metrology, RADAR and observational purposes [30], and have the benefit of not being limited to requiring naturally occurring energy in order to conduct sensing. Due to this they are more applicable for sensing within dark environments, are less sensitive to undesired external parameters and have more control over noise levels when compared to passive sensors. They do, however, require an energy source and as a result exhibit a higher cost than passive sensors [30].

Electrical sensors can be further differentiated by their detection mechanisms and can be viewed as either analogue or digital. Analogue sensors produce continuous output signals proportional to the measurand, whereas digital sensors produce a discrete binary signal, encompassing sensors where the signal conversion and transmission is done digitally [30].

The applicability of electrical sensors falls away within applications that require resistance to electromagnetic interference [10], which opens up the possibility for optical-based sensors. Optical sensors come in a variety of forms, from cameras detectors to free space interferometers. This thesis will focus on a subset of optical sensors relating to optical fibre-based sensors, which allow for light to routed where it is required with ease and a smaller form factor, when compared to their free-space optical counterparts.

2.3.2 Optical Fibre Sensors

Optical fibre sensors are a form of sensor that exploits light as the sensing medium. Such sensors fall under two distinct categories: intrinsic and extrinsic sensors. Intrinsic sensors exploit the fibre itself as the sensing element where the parameter of interest affects the fibre and results in a change in the guided light properties [11]. Extrinsic sensors use the fibre to relay a signal to and from the required sensing component, utilising the fibre only as a transmission medium [21].

Optical fibre based sensors offer the potential for a high sensitivity, a compact size and a dielectric architecture that extends their applications into high voltage, high temperature and corrosive environments [21]. Further to this, fibre sensors can operate as point sensors, that can be multiplexed together to form a series of point sensors over an extended region to produce quasi-distributed sensing capabilities. Within this arrangement, the fibre retains multiple sensing elements connected in series that provides continuous monitoring of a structure's condition as a function of its length [31]. This can be coupled with wavelength division multiplexing (WDM) to provide unique wavelengths to different sensing elements in order to provide real-time multi-parameter sensing [32], or optical time division multiplexing (OTDM). OTDM divides the bandwidth of a link into separate time slots. Ultrashort pulses are used to transfer digital data which have an inherent time delay between each pulse. Additional pulses can be inserted into these time slots which can be seen as separate channels. Channels at the same wavelength can be transmitted through the same fibre [33].

Quasi-distributed sensor networks operate by taking measurements at predetermined distances along the fibre, decreasing the overall sensor cost and size of the sensor while still providing good results for continuous spatial measurements [31]. Distributed sensor networks allow for the manufacture of smart structures capable of providing in-situ structural health monitoring during manufacture and operation. Being able to monitor a component during the manufacturing procedure allows designers to assess and optimise the part or process to suit their needs, allowing them to work closer to mechanical reliability limits safely, while real-time structural health monitoring in operation has significant implications for cost and safety and allows for integration into failure prevention schemes [31].

Providing structural health monitoring for processes in harsh environments and at elevated temperatures becomes increasingly important as these conditions often result in a high severity and cost of failure while also being more difficult to inspect regularly. Determining the conditions within these processes allows for the early detection of operational conditions that may lead to potential failures. Hoffmann et al., 2007, demonstrate the feasibility of temperature measurement using methodologies based on Raman scattering, interferometric point sensors and FBGs [34]. Each method retains various benefits depending on the desired application of the sensing device. However, FBGs are well suited for applications requiring many temperature measurement points, the capability for strain and temperature discrimination and to allow for multiplexing into distributed sensor networks. As a result, FBGs are deemed the most suitable sensing technique for the project work [34].

2.4 Fibre Bragg Gratings

A FBG is a periodic modulation of the refractive index within the core of an optical fibre. This structure will reflect light at a wavelength that is resonant with the grating spacing (the Bragg wavelength) and allow other wavelengths to pass. It operates as a sensor in situations where external stimuli affect the refractive index and/or the physical spacing of the grating structure [35]. Such changes result in a shift in the Bragg wavelength.

FBGs were first reported by the physicist Kenneth Hill. Continuous wave light (488nm) from an Argon-ion source coupled into the fibre caused an unexpected increasing intensity of light reflected from the end of the fibre. It is this observation of photo-induced refractivity modulation of fibres, termed photosensitivity, which allows gratings to be in written inside fibre cores, [1, 36].

FBGs are a form of distributed Bragg reflector located inside the core of an optical fibre. In essence, a FBG functions much like an optical filter. If broadband light illuminates the grating, then the grating reflects light over a narrow wavelength range related to the grating spacing while transmitting the remainder of the light spectrum. This arises because reflection of incident light occurs at every change in the refractive index and the modulation of the refractive index promotes multiple back reflections of the incident light [36]. Where the spacing allows for constructive interference, there is a strong back reflection, known as the Bragg wavelength. This narrowband reflected light satisfies the Bragg condition defined by equation (2), which relates the dependence of the Bragg wavelength (λ_B) to that of the effective refractive index (n_0) and the Bragg grating period (Λ) [1, 36]. Incident light that does not satisfy the Bragg condition is transmitted along the fibre with little loss.

$$\lambda_B = 2n_0\Lambda \tag{2}$$

Figure 3 illustrates the concept of a FBG inscribed within an optical fibre. A broadband source is incident upon the grating and light at the Bragg wavelength is reflected back along the fibre. The remainder of the broadband source, $\lambda_{incident} - \lambda_B$, passes through the grating. This allows for the prospect of wavelength division multiplexing, with different gratings operating inside different distinct wavelength 'windows'.

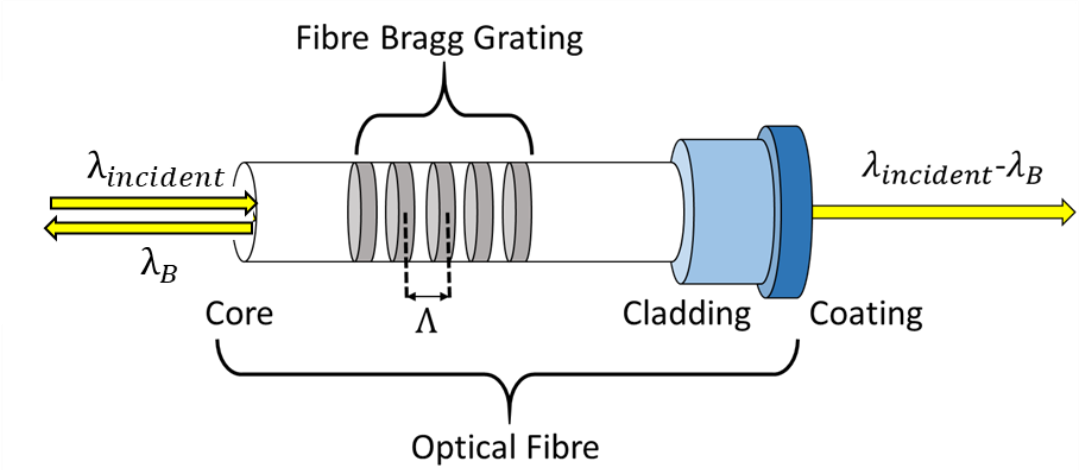

Figure 3 - Illustration of FBG inside a typical single core optical fibre. Broadband light enters the grating and light at the Bragg wavelength is reflected while the remainder is transmitted, derived from [37].

2.4.1 FBG Inscription

In order to inscribe FBGs using UV illumination to modify the refractive index requires a periodic pattern to be created inside the fibre core. This can be done using a variety of methods including interferometry, phase-mask, and point-by-point writing.

Holographic FBG inscription involves splitting a UV laser beam into two beams that are aligned to produce an intensity modulation at the overlapping region due to the resulting interference pattern, see Figure 4(a). This form of inscription caters for fast, flexible production of FBG sensors, however, drawbacks of holographic techniques stem from and the requirement for high mechanical stability and isolation from external parameters, in particular vibration, during manufacture and also the sensitivity of the interference fringe pattern to the optical alignment of the system [38].

Non-holographic FBG inscription techniques involve the periodic illumination of the optical fibre from a laser source. One such technique uses an amplitude phase mask, acting as a surface relief structure, placed within close proximity to the fibre [38]. The phase mask spatially modulates the incident UV beam, splitting it into several diffractive orders. This creates an interference pattern inside the fibre core that defines the index modulation and strength of the grating, Figure 4(b) [39]. The phase mask method allows for multiple gratings to be manufactured in quick succession, reducing the unit cost per sensor, promoting its viability for applications requiring multiple sensors manufactured with consistent parameters. Further, it reduces vibration sensitivity and minimizes alignment sensitivity. However, a drawback of the technique stems from the requirement of a new phase mask for each Bragg wavelength. G.Lee et al., 2012, demonstrate a method for producing highly complex, reproducible phase masks using a femtosecond source for inscription [39]. Lee's technique allows for high levels of control of the phase mask production process which is important for producing masks at the required Bragg wavelengths. The phase mask technique for FBG inscription is more repeatable and produces gratings with a higher sensitivity, when compared to other inscription techniques [36, 38].

Point-by-point inscription operates by irradiating one point of the fibre core with UV light before moving on by a distance defined by the grating period, see Figure 4(b). Point-by-point inscription provides high levels of control over the location of the index modulations and allows for the production of gratings with complex transmission and reflection spectra. However, the process is time intensive, requires displacements with an accuracy on a sub-micrometre scale and requires a high intensity, short pulse length laser source [40].

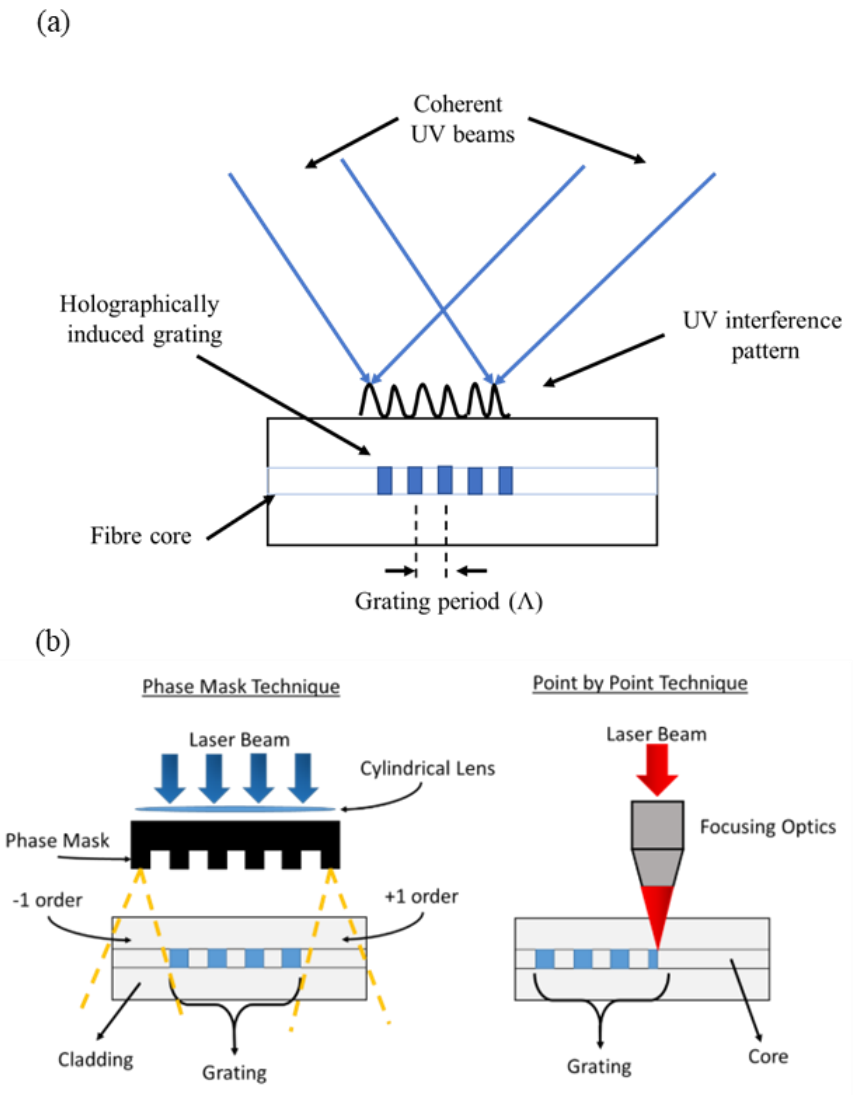

Figure 4 – (a) Schematic illustration of holographic FBG inscription. (b) Schematic illustration of non-holographic inscription techniques, phase mask and point by point, derived from [41].

Each of the inscription methods described above have beneficial characteristics for different manufacturing requirements. Holographic inscription allows for changes to be made to the grating properties quickly for rapid prototyping of sensors. The phase mask method reduces the cost of systems incorporating multiple embedded sensors and increases the reliability of manufacturing sensors with consistent characteristics due to the repeatability of the process [38]. The point-by-point method promotes the highest degree of flexibility of the inscription process, allowing for gratings to be manufactured fully optimised for their required application but is a time intensive process unsuited for production of multiple sensors with reliable characteristics.

In light of these considerations, where reliable and repeatable sensor arrays are required, this suggests that gratings fabricated using the phase mask technique is the most suitable for distributed sensing arrays embedded within metallic structures. This requires many FBG sensors connected in series that are able to provide accurate condition monitoring over the length of a component. Manufacturing these sensors within a single process ensures that the embedded sensor array retains consistent sensing characteristics across the entire sensor network.

Classical FBGs, such as Type 1 UV inscribed FBGs retain poor temperature stability at elevated temperatures and are subject to annealing effects that see them erased completely at around 700°C [42]. It is the introduction of femtosecond lasers into the FBG inscription process that allows for gratings to be written that are resistant to harsh conditions and high operating temperatures. When a pulse from a femtosecond laser interacts with a dielectric material, nonlinear multiphoton photoionization causes a localised change in the fibre, negating the requirement for photosensitivity of fused silica at the wavelength of inscription [40]. This increases the viability of other dielectric materials and inscription wavelengths for writing FBG sensors. Furthermore, using femtosecond lasers allows FBGs to be written that exhibit enhanced grating stability and temperature resistance for temperatures approaching the softening point of fused silica glass [40], promoting their viability for use within high temperature environments.

2.4.2 FBG Properties and Sensitivity to External Parameters

The FBG is an intrinsic sensor because perturbations in the properties of the fibre, induced by external parameters such as temperature and strain, will cause the Bragg wavelength to shift as a result of induced changes in the refractive index and the grating period. FBG sensor interrogator systems are designed to monitor this change in wavelength.

A typical interrogator system is illustrated schematically in Figure 5 and includes light from a broadband source that is coupled into an optical fibre containing the FBG. According to Bragg's law, light traveling at the Bragg wavelength will be reflected and the coupler directs this reflected signal to an optical spectrum analyser (OSA) so that this reflected light can be analysed [35].

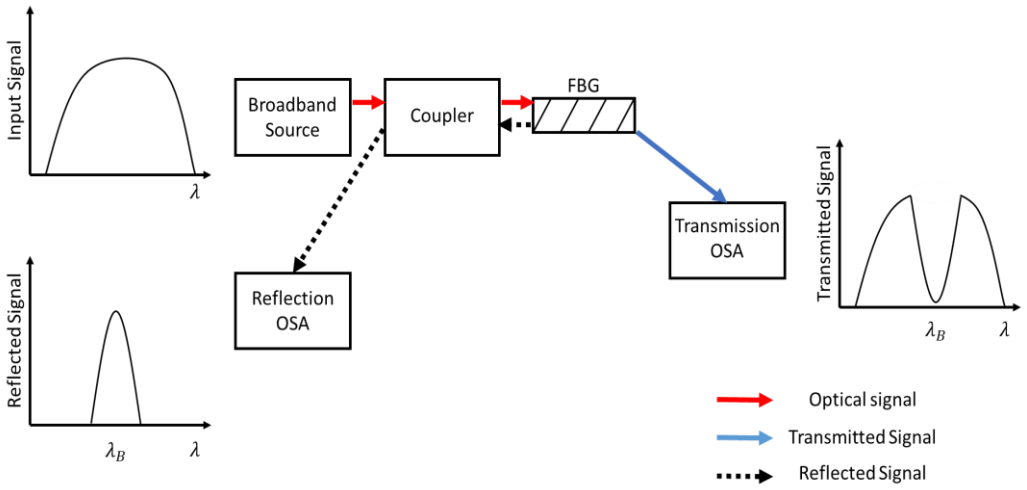

Figure 5 - Schematic illustration of an FBG interrogator and the associated optical spectra, derived from [35].

FBG sensitivity is governed by the fibre elastic, elasto-optic and thermo-optic properties that are affected by the induced load, strain and temperature on the structure that the sensor is embedded within. Equation (2) highlights the relationship between the Bragg wavelength and the temperature dependence of the effective refractive index and grating period. The differentiation of this relationship with respect to temperature leads to an expression for the Bragg wavelength shift, equation (3), where $\Delta\lambda$ denotes the Bragg wavelength shift, n denotes the refractive index inside the core, $n_0$denotes the grating refractive index and Λ denotes the grating period. Equation (3) can be correlated to a change in the environmental temperature in which the grating is operational [1].

$$\lambda_B = 2n_0\Lambda$$

$$\frac{\partial\lambda_B}{\partial T} = 2n_0\frac{\partial\Lambda}{\partial T} + 2\Lambda\frac{\partial n_0}{\partial T}$$

$$\frac{\partial\lambda_B}{\partial T} = 2n_0\Lambda\left(\frac{1}{\Lambda}\frac{\partial\Lambda}{\partial T} + \frac{1}{n_0}\frac{\partial n_0}{\partial T}\right)$$

$$\Delta\lambda = 2n_0\Delta\Lambda + 2\Lambda\Delta\mathrm{n} \quad (3)$$

The temperature sensitivity of a bare fibre is dominated by the thermo-optic effect and is given by equation (4), where α denotes the thermal expansion coefficient and L denotes the grating length.

$$\frac{\delta\lambda_B}{\lambda_B} = \alpha + \frac{1}{n}\frac{dn}{dT} \tag{4}$$

Where,

$$\alpha = \frac{1}{L}\frac{dL}{dT}$$

As the temperature is increased, the temperature sensitivity of the grating changes resulting in the relationship between the wavelength shift and temperature being slightly nonlinear, see Figure 6. The wavelength shift of an uncoated FBG was tested at elevated temperatures, for temperature below 150℃, the sensitivity is $7\mathrm{pm}/℃$ but increased to $11.5\mathrm{pm}/℃$ above this temperature for a Bragg wavelength of $1556\mathrm{nm}$ [36]. This alteration in sensitivity can be accommodated for in operation if the gratings are jacketed in a material with the appropriate properties in account of the effects of the surrounding material on the thermal expansion coefficient [36].

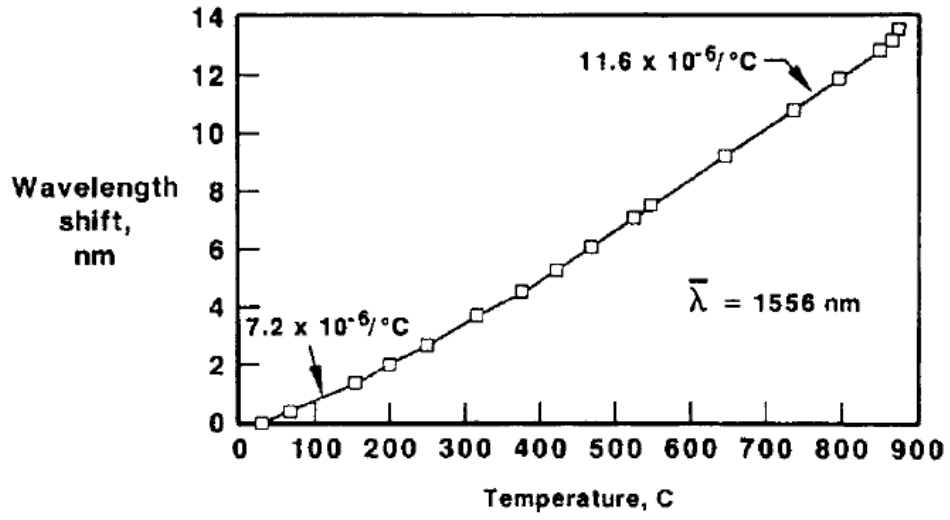

Figure 6 - Bragg wavelength shift against tempreature for an uncoated FBG at a Bragg wavelength of 1556nm, taken from [36].

The Bragg wavelength's strain dependence is another characteristic that explains the widespread use of FBG sensors [43, 44]. This dependence arises from the physical elongation or compression of the fibre and the resulting refractive index modulation and physical change in spacing that occurs in account of photo-elastic effects [36]. The Bragg wavelength shift in account of induced strain is given by equation (5) which assumes the strain to be homogeneous and isotropic [1].

$$\Delta\lambda = (1 - p_e)\lambda_B \varepsilon \tag{5}$$

Where ε denotes the applied strain and p_e is the photoelastic coefficient which includes the individual photoelastic contributions, p_{11} and p_{12} are defined by equation (6), [1].

$$p_e = \left(\frac{n_0^2}{2}\right)[p_{12} - \upsilon(p_{11} + p_{12})] \tag{6}$$

Applying longitudinal strain only, the spectrum of the FBG shifts while the width of the reflected spectra remains constant. Conversely, transverse strain applied to the FBG mitigates longitudinal straining, inducing a negative wavelength shift, broadening of the spectra and inducing a second transmission peak due to the effects of birefringence [45]. It is difficult to separate the effects of temperature and strain using a single FBG sensor. However, additional gratings can be incorporated that are strain isolated and therefore only measure temperature. If the sensors are isothermal then the FBG temperature measurements can be used to compensate for thermal effects in the strain measurements [45].

2.4.3 FBG Sensors for Condition Measurement at Elevated Temperatures

Type I grating index changes are associated with changes around oxygen deficiency defect centres (ODCs) excited by radiation from UV light or multiphoton processes [46]. The refractive index modulation of type I gratings is annealed out at 450°C , therefore they are not applicable for use at temperatures above this value [47].

Type II gratings, often referred to as damage gratings, are formed using high power pulsed ultraviolet laser sources. The formation process results from the threshold dependent multiphoton ionization of electrons, the heating of free electrons and the sudden transfer of energy to the lattice [46]. Type II gratings have been produced that retain stability for temperatures exceeding 1000°C, however, the processes used in their formation can induce diffractive scattering loss and detrimental effects on the integrity of the fibre structure [47]. Although more applicable for high temperature applications, Type II gratings compromise the beneficial sensing characteristics of Type I gratings due to a broader spectral width and increased losses for wavelengths below the Bragg wavelength.

Regenerated gratings form as a result of the high temperature annealing of hydrogen loaded Type I gratings [47]. Under UV irradiation, the dissociation of hydrogen occurs resulting in the formation of Si-OH or Ge-OH defects. After annealing at temperatures within the range of 600°C-700°C, the hydroxyl groups diffuse, forming water molecules in the glass that retain high thermal stability [47].

The annealing procedure erases the Type I seed grating and further heating at increased temperatures forms a new grating with similar spectral characteristics. Regenerated gratings have a low index modulation and therefore are not as susceptible to the large scattering losses associated with Type II gratings. They also retain a high thermal stability when subject to repeated cyclic temperatures up to 1000°C. However, the generated grating is weaker in comparison to the original seed grating by an order of magnitude which has implications for grating sensing characteristics [46].

Chong et al., 2012, demonstrated a regenerated FBG capable of repeatable high temperature response up to a temperature of 1200°C using a hydrogen loaded, highly germanium doped and photosensitive optical fibre [48]. The regenerated FBG was subject to heating and cooling cycles in a temperature range of 400°C-1200°C without degradation of the 3dB bandwidth and the temperature sensitives for the heating and cooling cycles were determined to be 17 pm/°C and 17.4 pm/°C respectively [48]. The degradation in performance for temperatures above 1200°C is believed to be due to the temperatures approaching the softening point of fused silica glass. The demonstration of the high stability of regenerated FBGs, fabricated in high germanium concentration photosensitive fibres, up to a temperature of 1200°C, suggests that regenerated FBGs are suitable for high temperature sensing applications.

Canning et al., 2008, demonstrated regenerated germanosilicate fibre gratings capable of surviving temperature cycling up to 1295°C [29].

The use of germanosilicate fibres is desirable as they are readily available, retain good optical properties and allow for gratings to be written at low cost [29]. These characteristics promote the viability for using regenerated FBGs for the embedment of distributed sensor arrays within high melting point metals.

2.5 Protective Fibre Coatings

When operating within corrosive environments where the fibre is exposed to abrasion and high moisture content, fibre degradation may occur resulting in detrimental effects on the operational lifetime of the system [11]. Furthermore, non-uniform stress, strain and thermal loads, induced during embedding and operation, can result in destruction of the fibre structure [49]. For the application of embedding fibres within metal components, the fibre requires a coating to protect it during the embedding process and mitigates the effects of the thermal expansion coefficient mismatch between the fibre and embedding material [50].

Antunes et al., 2012, measured the rupture limit, the stress level beyond which rupture occurs, and Young's modulus for a standard optical fibre, a photosensitive optical fibre and a standard optical fibre with an acrylate protective coating by bending the fibre until rupture occurs [11]. The measured rupture limit of the coated fibre was significantly larger than that of the two uncoated fibres due to the coating strength, and the Young's modulus is significantly lower see Table 1. The determination of parameters such as the Young's modulus and rupture limit provide useful data for the characterisation of optical fibre sensors where the fibre is subject to a perturbation or force [11]. However, fibre coatings do not fully protect the fibre from external factors and the degradation of fibre strength with aging is a function of both the presence of moisture and the diffusion rate of ions across the coating [11]. The successful operation of optical fibre sensors is heavily reliant on their resistance to high temperatures and abrasive environments.

Fibre	E_g**(Gpa)**	**Rupture Limit (N)**
Standard fibre without coating	69.22 ± 0.42	4.35 ± 1.45
Photosensitive coated fibre	68.56 ± 1.47	7.57 ± 2.51
Standard fibre with Acrylate coating	16.56 ± 0.39	24.60 ± 2.38

Table 1 -Young's modulus and Rupture limit for a standard uncoated fibre, photosensitive fibre and a standard coated fibre, taken from [11].

Metallic protective fibre jackets can be used to protect fibres that are to be embedded into metallic components. Methods for the metallisation process include dip coating, electroplating and sputtering techniques that coat the optical fibre in a metallic material [49]. Li et al., 2009, demonstrated a technique for plating nickel (Ni) onto optical fibres whereby the Ni coating is applied via the reduction of nickel sulphate complex with sodium phosphate, propionic acid and boric acid. The fibre then undergoes an electroplating process and the resulting thickness of the Ni layer changes with respect to the electroplating process time [49]. Other metal coating techniques exist for this purpose, such as electroless plating and RF sputter deposition, but electroplating remains the most suitable for depositing thick layers ($> 100\mu m$) of nickel onto lengths of optical fibre, providing they have a conductive "seed" layer to deposit onto.

2.5.1 Temperature Sensitivity of Nickel Coated FBG Sensors

Control of the coating thickness is important for optimising the performance of the embedded fibre sensor. The mismatch in the thermal expansion coefficients between the fibre and the Ni layer results in significant change in the temperature sensitivity of the FBG senor when compared to the case of a bare fibre as the fibre takes on the effective bulk properties of the Ni layer [51].

Jian-Feng Xie et al., 2007**,** characterised the temperature sensitivity of Ni coated FBG sensors for varying thicknesses of the coating layer. The results of which coincided well with a theoretical characterisation of the temperature sensitivity of a Ni coated FBG, $\frac{\Delta\lambda_B}{\Delta T}$, expressed by equation (7) [51].

$$\frac{\Delta\lambda_B}{\Delta T} = (\alpha_0 + \zeta)\lambda_B + [\varepsilon^s_{zz0} - \frac{n^2_{eff}}{2}[(p_{11} + p_{12)\varepsilon^s_{rr0}} + p_{12}\varepsilon^s_{zz0}]]\frac{\lambda_B}{\Delta T} \quad (7)$$

Where α_0 is the thermal expansion coefficient of the FBG, ζ is the thermo-optic coefficient of the FBG, p_{11} and p_{12} are the FBG fibre Pockels coefficients, ε^s_{zz0} and ε^s_{rr0} are the axial and radial thermal strains respectively, induced by thermal stress on the FBG [51]. Figure 7 illustrates the experimental measurements compared against the theoretical relationship between the thickness of the Ni coating and the resulting temperature sensitivity of the FBGs. The points dictating the experimental results coincide well with the predicted theoretical curve showing that equation (7) provides an important correlation for defining the temperature sensitivity FBG sensors coated in a comparatively thick Ni layer.

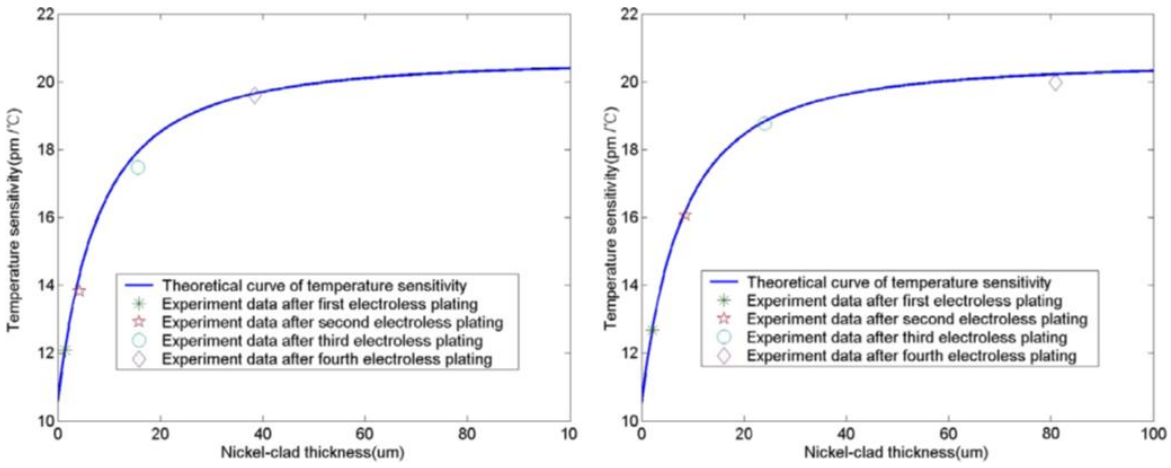

Figure 7 - Temperature sensitivities of Ni-coated FBG sensors with different coating thicknesses. Left hand figure is for a FBG wavelength of 1544nm and the right-hand figure is for a FBG wavelength of 1538nm, taken from [47].

Ni is a desirable coating material for embedding sensors within stainless steel (SS) components. The alloy SS-316 contains a high concentration of Ni in its constituent composition, see Table 2. This is beneficial for embedding into SS as the Ni retains similar thermal properties to SS and readily mixes with the melt pool during the embedding process, resulting in a good mechanical bond between the Ni coating and surrounding bulk SS-316 material [50]. This promotes its viability as a coating material for fibre sensors integrated within SS components manufactured using techniques such as SLM.

Constituent	Composition Percentage
Sulphur	0.03
Carbon	0.08
Phosphorus	0.045
Manganese	2
Silicon	0.75
Chromium	16-18
Nickel	10-14
Molybdenum	2-3
Nitrogen	0.1
Iron	balance

Table 2 - Constituent composition of stainless steel 316 alloy, taken from [52].

2.6 Embedding Optical Fibres in Metals

Embedding optical fibres in components allows for process control and condition monitoring within a manufactured structure [53]. It also provides a method for monitoring changes inside a material and offers protection against sensor damage from external chemical, enviromental, and mechanical sources [2]. Embedding fibre sensors within polymer materials is widely documented for temperature, strain and pressure sensing and has applications within low temperature structural health monitoring, [1, 4]. Within polymer-embedded sensors, the host polymer melting point is significantly lower than that of silica glass [1], which reduces complexity in the embedding process. However, the temperature stability of polymer-based materials limits operational temperature ranges of sensors embedded within polymers to below 350℃ [12]. Therefore, in order for fibre-based sensors to be viable for high temperature condition monitoring applications, embedding fibres into high melting-point metals, such as SS alloys, is required [2].

Fibre sensors embedded in metal components retain high sensitivity, accuracy and temperature capacity [2]. This allows for reliable temperature measurements and operation within high temperature and corrosive environments. In regards to strain measurements, metal-embedded sensors retain good accuracy, linearity and a sensitivity that is comparable to that of bare FBGs. However, the complexity of the embedding process increases due to the high melting points of the metal alloys [2].

There is a significant mismatch in the coefficients of thermal expansion for the fibre and the metal alloy within which it will be embedded. Furthermore, this difference will increase with temperature, creating further mismatch between the two values [2]. Other material properties are also mismatched, for example the Young's modulus and Poisson's ratio, which are discussed below.

The lower Poisson's ratio of the fibre dictates that the fibre will contract less radially than the surrounding embedding material when subject to longitudinal stretching, inducing pressure points at the fibre-alloy interface [2]. This interfacial stress is reduced when the structure is subject to longitudinal compression as the Young's modulus of the embedding alloy is less than that of the fibre [2]. The difference in thermal expansion coefficients induces thermal stresses when embedding fused silica fibres within metal alloys that are detrimental to the fibre-alloy attachment as the metal and fused silica will expand and contract at different rates. Furthermore, the material properties mismatch can also induce detrimental effects of the light-guiding properties of the fibre that will inhibit their use within sensing applications [2].

Sandlin et al., 2003, demonstrated the embedment of a fused silica FBG in a nickel-based alloy using high temperature vacuum brazing technique [2]. As a result of the high temperatures reached within this process, the fibre ended up in a longitudinal and transversal compressive state. Additionally, the Ni coating dissolved completely into the embedding alloy during the embedding process, which caters for a stable fibre-alloy attachment as it promotes a good compressive joint between the fibre and the metal alloy as it cools down [2]. Figure 8 illustrates cross sections of three embedded fibres, taken from [2]. Figure 8(a) depicts a Ni coated fibre and the complete dissolving of the coating layer into the embedding substrate. Figure 8(b) depicts a copper coated fibre, which still retains good conformity and bonding, however, dissolution of the coating material is incomplete. The bare fibre, Figure 8(c), shows alterations to the fibre structure and the insufficient contact between it and the embedding material resulting in voids. If the fibre contained an FBG within the embedding region, this would still be suitable for temperature sensing purposes, but its applicability for strains sensing would be reduced as the poor adhesion would result in calibration errors as it could lead to hysteresis or unpredictable response to stimuli. As Ni is a constituent of SS-316, dissolution of the fibre coating will occur if embedded within a SS-316 substrate, promoting good contact with the embedding material and mitigating detrimental effects on the fibre structure and light guiding properties.

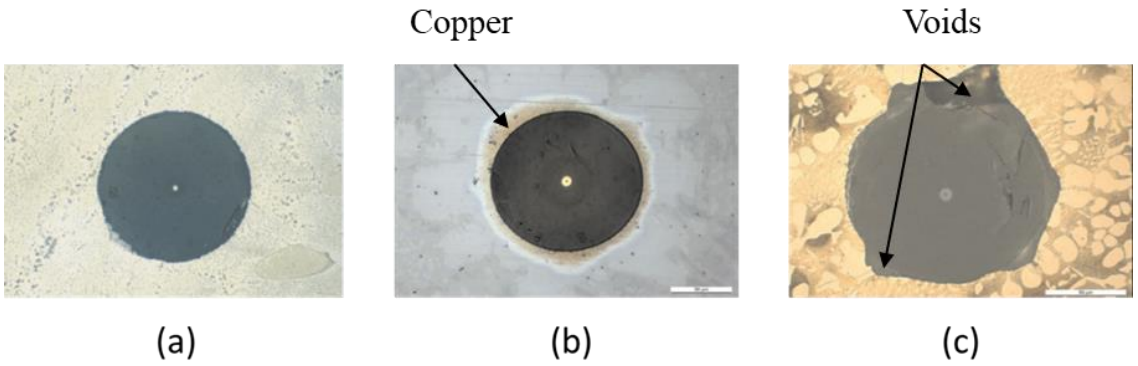

Figure 8 - fibres embedded in Ni alloy, (a) - Ni coated fibre embedded into SS-316 substrate, (b) - copper coated fibre embedded into SS-316 substrate, (c) - bare fibre embedded into SS-316 substrate with voids around the fibre circumference highlighted, taken from [2].

Maintaining the fibre-alloy interface in compression promotes cylindrically symmetric stress states at this boundary. This has multiple beneficial characteristics when considering the performance of fibre sensors embedded within metallic structures. Optical fibres are stronger in compression than they are in tension [2], which is important for ensuring robustness and longevity of sensor systems. Furthermore, polarisation and micro-bending effects are minimised [2]. An additional benefit pertains to the fact that the compressive interfacial stress reduces with respect to increasing temperature, which improves sensor reliability at higher temperatures [2].

For applications within high temperature environments, fibre sensors embedded within metallic alloys is the most viable option. Further to this, the research conducted by Sandlin et al., 2003, illustrates the importance of metallic fibre coatings for protecting the fibre during the embedding process within high melting point metal alloys [2].

2.7 Embedding Optical Fibre Sensors in Additive Layer Manufactured Metallic Components

The layer-by-layer approach of ALM opens up opportunities to incorporate sensing elements *inside* components in a way generally unattainable using traditional fabrication routes. The ALM process provides access to any point of the component during manufacture [1].

Embedding sensors in ALM components allows for the manufacture of 'smart' components that are able to provide condition and health monitoring of the component structure during manufacture and service [50]. Embedded sensor networks in components allows for parameters such as temperature and strain to be monitored during service [50]. The monitoring of these parameters is vital for producing structures approaching the limits of their mechanical stability safely, allowing engineers to design components with a smaller safety-margin without detriment to performance and intervene when appropriate to avoid catastrophic failure. Furthermore, these sensors would provide real-time feedback during component failure, such as during product testing, providing key insights into the events leading up to the failure events [1].

In order to retain the manufacturing benefits of ALM techniques for sensor embedding within high melting point metals, a suitable metallic ALM approach, such as SLM or SLS, must be used.

2.7.1 Selective Laser Melting

In powder bed fusion (PBF) ALM, a three-dimensional component is manufactured by stacking of many two-dimensional layers. To achieve this, a thin layer of powder is deposited on a build plate within a controlled inert environment. The powder is selectively melted (using either a laser or electron beam source) to form a solid part 'layer' with geometrical form required by that build layer. The build plate lowers by a set amount that defines the layer thickness, and a fresh powder layer is deposited, and the process is repeated until a final part is produced [20, 54]. Figure 9 illustrates a schematic of a typical PBF manufacturing system. PBF manufacturing allows for the production of high-resolution parts (with resolutions corresponding to laser spot size, typically in the order of μm) and internal features such as cavities while maintaining high levels of dimensional accuracy and control throughout the build process [20].

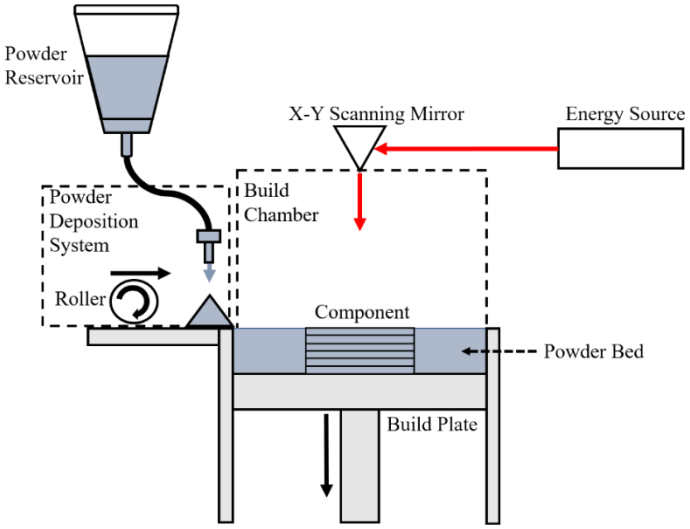

Figure 9- Illustration of a typical powder bed fusion additive layer manufacturing system.

SLM systems refer to PBF manufacturing systems that utilise one or more lasers as the energy source. The laser selectively fuses the powder particles of each layer in addition to fusing it to the previous layer underneath it [54, 55]. The build process takes place in an inert atmosphere, often composed of argon or nitrogen gas, in order to limit oxygen levels during the manufacturing procedure, which combined with the high temperatures could lead to material oxidation. Electron beam melting (EBM) systems operate under a similar mechanism to SLM systems but use high voltage (typically 30kV-60kV) electron beam to melt the powder material [56]. EBM systems can achieve higher scanning speeds and energy density than SLM but are less suited for achieving high dimensional accuracy and surface quality. This is due to to thicker applicable layer heights (50-200µm compared to 20-100µm for SLM), larger melt pool size (200-1200µm compared to 100-500µm for SLM) owing to larger minimum feature size, poorer surface finish, and worse geometrical tolerance (±200µm compared to ±0.05-0.1µm for SLM) [54]. Therefore, for parts with complex external and internal geometries, SLM is the preferred methodology. Figure 10 highlights the process steps necessary to produce a manufactured part from a three-dimensional CAD model using the SLM method.

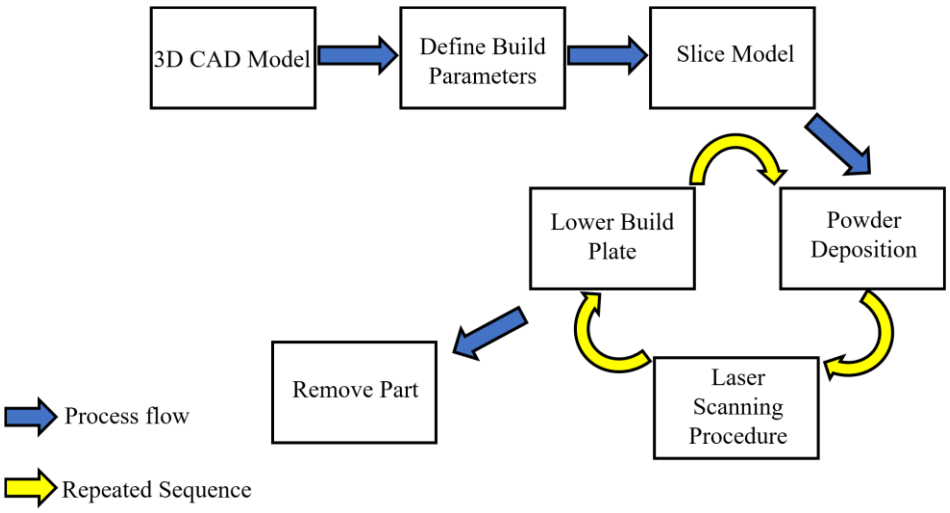

Figure 10 - process steps required to manufacture components using SLM.

2.8 Selective Laser Melting Build Considerations

SLM offers a high level of control of parameters within the build process and optimal parameters will differ depending on the desired feature. For instance, outer-boundary scans require different parameters to inner hatch scans as they do not overlap with previous scans resulting in powder material being drawn into the melt pool from both sides of the laser scan and increased layer thickness. Careful consideration of the parameters involved within the SLM process is imperative for achieving successful results in terms of part density and surface quality. This has specific relevance to the embedding of optical fibre sensors, which introduce further complexities into the manufacturing procedure in order to ensure the sensor survives the embedding process and is sufficiently bonded within the bulk printed material.

2.8.1 Underlying Process Mechanisms

When energy from a laser beam is incident on a material surface, the surface undergoes an increase in temperature. Equation (8) defines the process power required to achieve a certain temperature change for a laser beam moving across a material surface [57].

$$P_{process} = \frac{d\Delta Q}{dt} = \Delta T c_p \rho \frac{V}{t} \tag{8}$$

Where ΔQ defines the energy required to raise the temperature of a volume of material, ΔT is the change in temperature, c_p is the specific heat capacity,ρ and V are the material density and volume respectively, and t denotes the time the laser is in contact with the material. When the area of material is large in respect to the diameter of the laser beam, the width of the melt pool can be approximated as the beam diameter (d). The laser power required to achieve successful melting of the powder material is defined by equation (9) [57, 58].

$$P_{Laser} = \frac{P_{process}}{A_m} = \left(c_p(T_m - T_i) + H_m\right)\rho\left(\frac{\pi d^2}{8}v\right) \tag{9}$$

Where T_m is the material melting temperature, $T_i$is the initial temperature, H_m is the melting enthalpy, A_m is the material's absorption coefficient and v is the beam speed [12]. Defining the laser power allows for the determination of the laser energy density (E), in $\mathrm{J/mm^3}$, of the SLM manufacturing process [59] see equation (10).

$$E = \frac{P_{Laser}}{v\ h\ w} \tag{10}$$

Where h is the hatch spacing and w is the layer thickness, both input in mm. For a typical system operating at 100W laser power, scanning speed of 400mm/s and hatch spacing and layer thickness of 100µm, the energy density would be 25 $\mathrm{J/mm^3}$. In practice, this is suitable for melting SS-316, see Chapter 3.

Understanding the SLM process involves considering multiple physical phenomena. These include; the absorption and scattering of laser radiation, heat transfer, phase formation, evaporation and emission of material, surface tension induced fluid flow within the melt pool and chemical reactions [60]. Furthermore, the mechanisms dictating heat interactions of the material with the laser radiation significantly differ from an opaque metallic structure to that of metallic powder material. The absorptivity of a metallic powder is dependent not only on the physical and chemical properties of the powder material but also its granular form and apparent density. During the initial stages of the SLM process, the powder is still in a solid state and the powder material properties influence the process through thermal conductivity. As the process continues, the powder is re-melted and the ratio of thermal conductivity to the material absorptivity must be taken into account [60]. The laser power must be sufficient in order to promote re-melting of the material, as this is important for achieving suitable bonding to preceding layers.

2.8.2 Build Atmosphere Considerations

The exothermic oxidation of iron-based alloys, when heated in the presence of oxygen results in discoloration and poor surface finish during the SLM process. This is significant because in a layer-based fabrication approach this would lead to oxidation inside the sample. Oxygen in the atmosphere increases the melt pool volume, reducing surface quality and achievable resolution [61]. Furthermore, surface oxides and slags form as the powder undergoes heating and melting by the laser, which has detrimental effects on the quality of single tracks and adhesion to preceding layers [61]. In order to counteract these phenomena, the oxygen concentration in the build atmosphere is reduced. Studies have shown that to achieve a sufficiently small melt pool volume to ensure that surface tensions do not dominate during the manufacturing process, the atmosphere needs to be void of any oxygen content ($< 1\%$) [61]. Therefore, a build atmosphere composed of an inert gas, such as argon or nitrogen, is required to build parts with good surface quality and high geometric complexity.

Argon is a popular choice in this regard as at induces less porosity than a nitrogen based atmosphere and allows for the manufacture of steel components that retain the martensitic properties of steel [62]. This is important for achieving fully dense parts with mechanical properties similar to components manufactured using other manufacturing techniques. Operating the SLM under vacuum further works to reduce the porosity in printed parts when compared to inert gas techniques, but poses significant technical challenges in order to conduct successfully [63].

2.8.3 Powder Material Considerations

The SLM process involves heat conduction, melting, densification and cooling within a very short space of time [64]. Therefore, different metals will exhibit different characteristics during these process mechanisms. SS is a desirable material for high temperature sensing applications as it exhibits melting temperature in the order of 1400°C. This promotes its operational viability within high temperature applications such as high temperature condition monitoring but is still below the melting point of silica glass, which is important for the successful embedding of optical fibres [50]. Further austenitic variants of SS such as SS-316 couple well with optical sensors as they are applicable for use in applications involving electromagnetic fields due to their low magnetic and relative permeability [52].

The required grain size of the material powder is related to the desired layer thickness of the component fabrication process. For the same overall build height, parts composed of more layers generally exhibit better surface quality. As a result of improved interlayer surface quality, smaller grain sizes allow for achieving higher part densities [65].

The particle size of the powder material has a direct effect on the flow-ability and packing density of the powder. Smaller particles promote higher packing densities as they can fill voids between larger particle sizes. However, finer particles have a larger surface area resulting in the absorption of more laser energy, increasing the particle temperature and altering the heat interactions of the material with the radiation [60]. Furthermore, non-uniform particles may induce anisotropic shrinkage as the particles tend to be orientated in a non-random fashion [64]. Manufacturing difficulties can stem from density packing and structure of the powder material, which can be mitigated if finer grain sizes are used in conjunction with uniform or spherical shaped powder particles [64].

2.8.4 Single Track Formation

SLM allows for the production of functional components with high mechanical properties and geometric complexity. The overall component properties depend upon the formation of individual tracks and layers. During the SLM process, the laser melts the powder particles in a line that is directed to form the geometry dictated by the 3D CAD model and build process parameters. Controlled and reliable formation of these single tracks is imperative in achieving high dimensional accuracy, good structural integrity and high density of components. For instance, overlapping tracks may induce balling effects in account of the surface tension from the molten powder material and promote instabilities within the track formation [60], however, insufficient overlap will create porous layers and could result in a structural weakness. Process parameters such as the laser power and scanning speed have a direct effect on the stability of single track formation. Defining a scanning speed that is too low may induce distortions within the track formation due to excessive heating of the melt pool. In contrast, if the scanning speed is set to high, balling effects can occur that lead to poor surface quality and increased porosity [60].

Yadriotsev et al., 2013, demonstrated that the scanning speed directly affected the width of single tracks produced by SLM. It was demonstrated that a scanning speed of $0.24\ m/s$ correlated to a track thickness of $90\mu m$ where as a scanning speed of $0.08\ m/s$ produced track widths of $140\ \mu m$ [66]. This was conducted when all other process parameters were maintained consistent and demonstrates the direct relationship between scanning speed and track thickness [66].

Figure 11 illustrates the relationship between the scanning speed and preheating temperature to the thickness of a single track. Increasing the scanning speed reduces the thickness of the layers, however, it also reduces the depth of the melt-pool into the substrate, which limits the bond between the powder material and the substrate, as shown in Figure 12. To achieve good intermixing of the powder material and the substrate, the melt-pool depth should be similar to the thickness of each subsequent material layer.

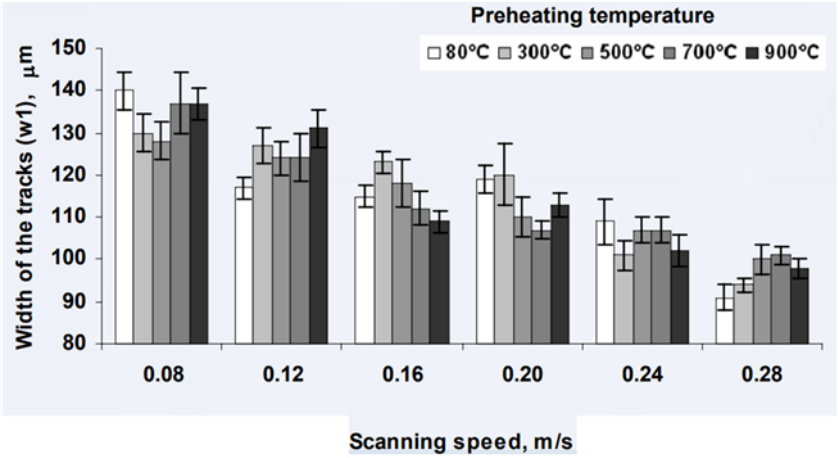

Figure 11 - Track width for different scanning speeds and preheating temperatures. Layer thickness maintained at 80µm, laser power maintained at 50W, taken from [66].

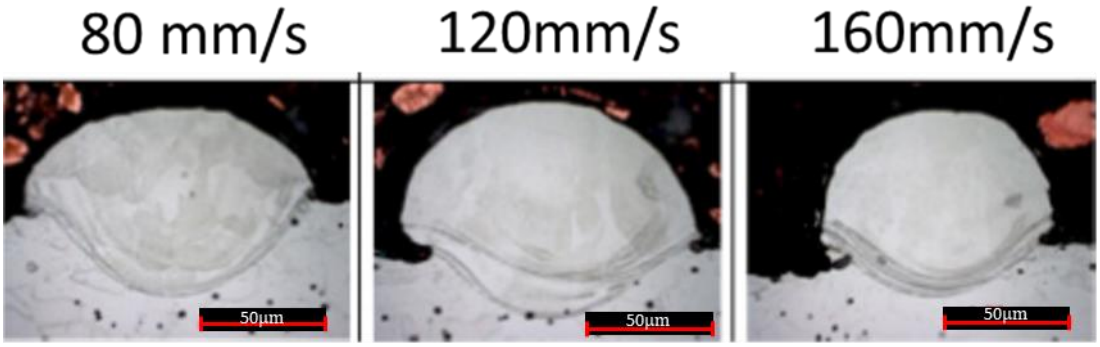

Figure 12 - Track cross sections for increasing laser-scanning speed. Layer thickness 80µm, laser Power 50W, preheating temperature 80°C, taken from [67].

Similar considerations are required for the bonding of subsequent material layers during the SLM process. The intensity of the laser radiation decreases with an increasing penetration depth, inducing different heat characteristics depending on the depth of interest [64]. Therefore, increasing the laser power and preheating temperature would induce a higher penetration depth and promote suitable bonding to preceding layers. This does however cause widening of the melt pool, which would be in detriment to the quality of the manufactured component and the applicability of achieving stable tracks at reduced thicknesses.

2.8.5 Laser Scanning Parameters for Achieving Fully Dense Parts

The hatch spacing defines the line-to-line distance between each individual track of melted powder material and as a result has a direct influence on the layer surface morphology and relative density of manufactured parts. If this value is large in comparison to the track thickness, then pockets of unmolten powder remain in the gap, increasing the overall porosity of the structure. Furthermore, this inhibits the overlapping of individual tracks which can prohibit the intra-layer bonding of the material, which is in detriment to the density and structural integrity of manufactured components [68]. Figure 13 illustrates the increase in relative density of manufactured components in relation to an increasing hatch spacing. The dark features correspond to unwanted pores within the material layers. The size of the hatch spacing has a direct influence on the manufacturing time of the SLM process. However, it must be balanced with the energy density in order to promote efficient manufacture of components with suitable material properties for their application.

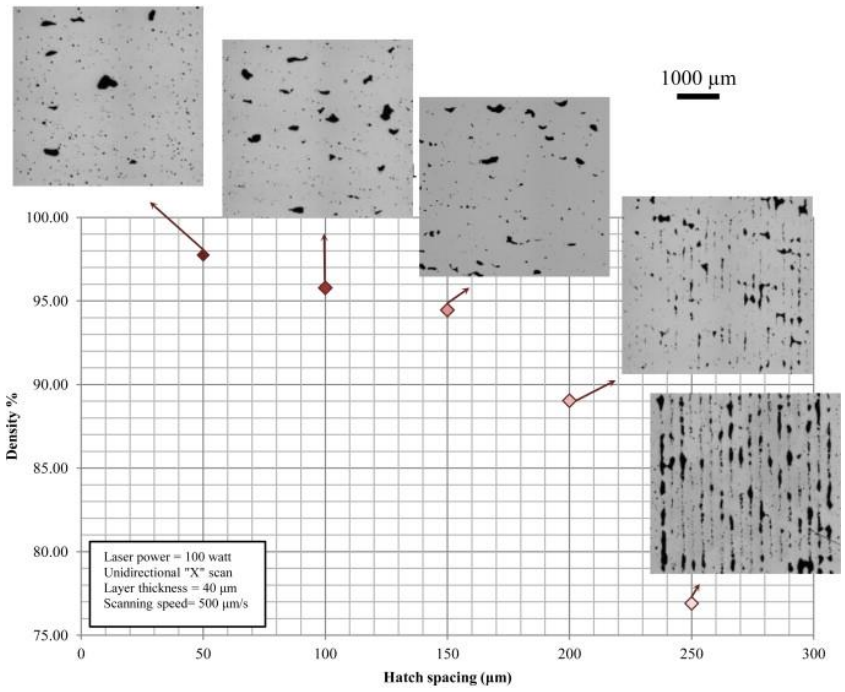

Figure 13 - Relative density against hatch spacing for SLM manufactured parts, taken from [68].

The scanning speed also has a direct effect on the density of manufactured components. Metallurgical pores can form at lower scanning speeds in account of gases trapped within the melt pool, whereas keyhole pores - due to the rapid solidification of the metal without sufficient molten material within the gaps - occur at higher scanning speeds [68]. Higher scanning speeds additionally promotes capillary instability in the melt pool and produce balling effects in account of liquid droplets forming on the material surface, see Figure 14 [68] . These effects promote complexity in the definition of the laser parameters within the build process in light of achieving fully dense parts with SLM as a balance must be found that mitigates the occurrence of each.

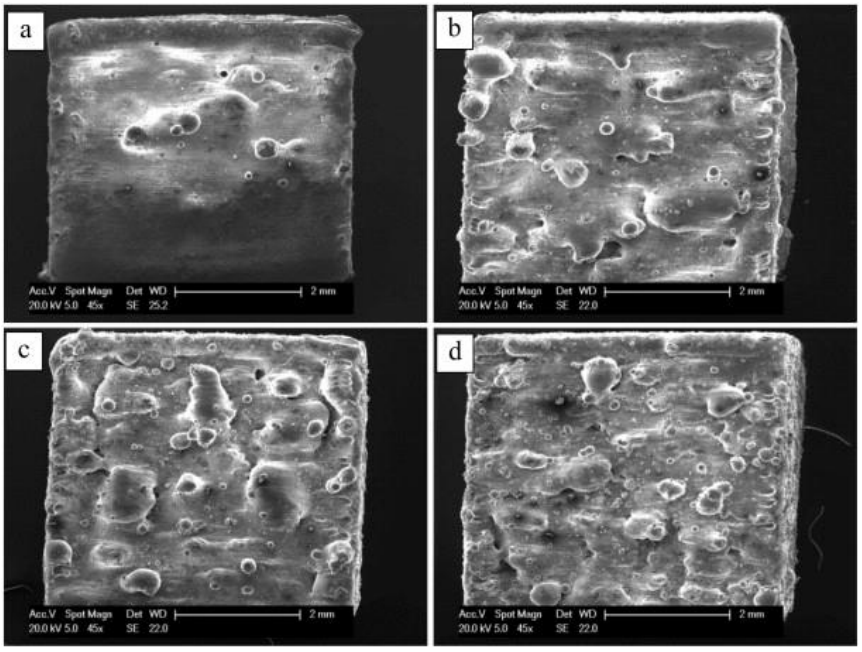

Figure 14- Micrographs illustrating the effect of scanning speed on the occurrence of balling artifacts, with an increase in balling features from a-d, corresponding to an increasing scanning speed. Taken from [68].

Defining a scanning strategy can work towards mitigating the aforementioned detrimental effects. Aboulkhair et al., 2014, studied the effects on varying scan strategies on producing fully dense parts with good structural integrity and surface quality. The highest densities were achieved when incorporating a double unidirectional scan with differing laser powers but a consistent scanning speed, essentially incorporating a re-melting procedure at each layer of the SLM build. By scanning each layer twice, the occurrence of keyhole pores and metallurgical pores were mitigated at a scanning speed of $500mm/s$. As a result, components retaining a density of 99.82% were produced which is a significant increase when compared to the results obtained for a single scanning procedure (97.74%) [68].

2.9 Embedding FBG Sensors in Additive Manufactured Stainless Steel-316

Li, 2001, demonstrated an embedding approach using shape deposition manufacturing that is applicable for high temperature sensing applications [3]. Figure 15 illustrates the embedding procedure proposed by Li; U-shaped grooves are built into a component formed of SS-316, the ALM process is then interrupted and a chromium-rf sputtered fibre is placed into the groove. The fibre is coated in Ni by electroplating until the groove is filled and powder material is pre-placed onto the surface of the coating layer before the part is returned to the ALM machine to finish the manufacturing procedure [3]. Li demonstrates the feasibility of embedding optical fibre sensors within SS-316 components. The proposed method is applicable for operation at high temperatures and demonstrates the applicability for measuring temperature and strain from inside the component [3].

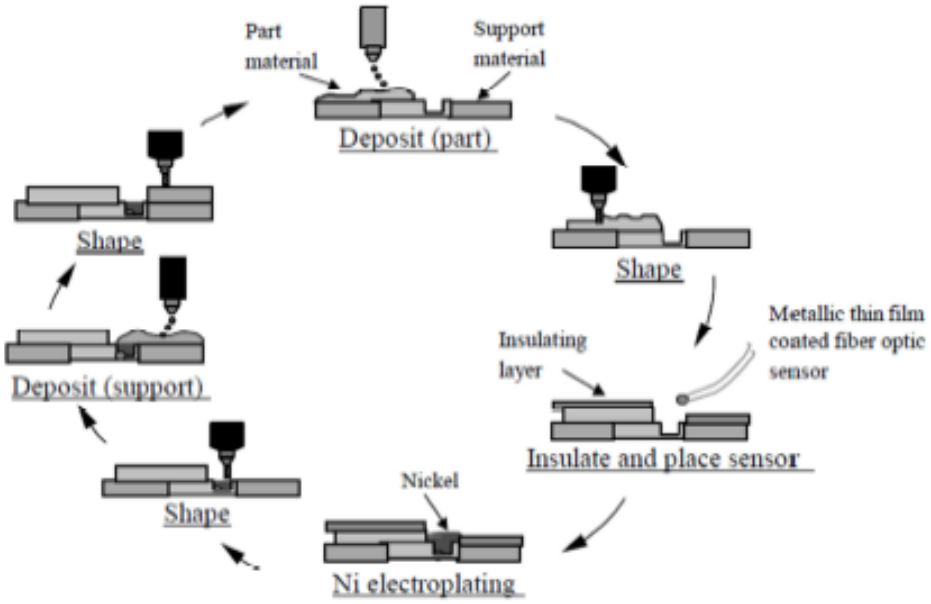

Figure 15 - Process diagram of fused deposition modelling manufacturing as used by Li, taken from [3].

Maier, et al., 2013, demonstrated the successful integration of nickel jacketed single mode fused silica fibres into SS-316 using SLS [50]. However, a large spot size during the manufacturing process induced a low powder density, inhibiting access close to the fibre due to the large size of the resulting melt pool. The methods described by Li and Maier require a thick protective Ni coating on the fibre which can have significant effects on the manufactured components material properties. Decreasing the diameter of the Ni layer would limit these material property and operational alterations.

Havermann et al., 2015, demonstrated the embedment of Ni coated FBG sensors into SS-316 components without detriment to their mechanical properties using SLM [43]. The small spot sizes achievable by SLM systems are well suited for the application of fibre embedding as the melt pools are small, limiting heat interaction through conduction with the surrounding material [43]. This method provides promising results in regards to condition monitoring of components at elevated temperatures. However, stresses induced at high temperatures induced slippage between the glass metal bonding mechanism, limiting the operational temperature ranges achievable by the FBG sensor. As a result, the sensors were not able to operate at temperatures exceeding 400°C. Overcoming this glass-metal bonding issue is important in achieving SS-361 embedded FBG sensors applicable for operating at elevated temperatures.

2.10 Intermediary Metal Joining Process

Direct embedding of the fibre sensor using SLM results in poor bonding of the underside and side walls of the fibre coating-base metal interface. Additional process steps in the form of metal joining processes such as brazing, soldering and welding can be performed to improve the bonding at these interfaces, important for achieving reliability of the sensor and for determining strain measurements. The feasibility of these joining processes for fibre embedding within high melting point stainless steels is investigated.

2.10.1 Soldering

Soft soldering relates to low temperature soldering techniques and can be used when strength of joint is not a major factor, but a seal is still required. Different grades of stainless steel and surface finishes have unique solderability characteristics. Stainless steels with a high carbon content, such as the 400 series, may be difficult to solder. In general, the 300 series of stainless steels can be soldered, however, molybdenum and titanium bearing stainless steels may prove difficult to solder, which may inhibit the solderability of type 316 stainless steel [69]. Tinning (the application of solder to the metal prior to the soldering process) enhances the strength and corrosion resistance of soldered joints [69].

The recommended maximum permissible service temperature for a solder alloy under stress is 40°C below the solid-state melting temperature [70]. Therefore, typical solder alloys have insufficient operational temperature limits to be reliable at temperatures> 180°C. The application of silver to the alloy constituents increases the strength, wetting power and melting point of the solder alloy when compared to conventional tin/lead or pure tin solder [70]. Soldering alloys exist that retain sufficient operational temperature limits but may suffer from long term aging effects if subjected to elevated temperatures close to this limit for extended periods of time which has implications for the integrity of parts in operation.

2.10.2 Brazing

Brazing is a thermal material bonding process in which dissimilar metals can be bonded together by application of a filler metal with a liquid transformation temperature lower than that of the base metal. Brazing typically defines metal thermal bonding at temperatures greater than 450°C. Soldering is a low temperature variant of brazing in which a non-ferrous filler metal with a liquidus temperature less than 450°C is used.

In comparison with welding, where two metals are fused together by applying a concentrated heat source to the joint area, and the temperatures are excessive due the process requires the melting of both the filler metal and the base metal, brazing offers benefits for precise and small scale joining of two metals. Component distortion is minimized as the base metal is not heated to its melting point, the process thermal cycles are predictable, dissimilar metals can be joined and a variety of joint designs and gap sizes can be accommodated for [71, 72].

Brazing works by manually feeding or pre-placing brazing filler material into a joint and applying heat to melt the brazing material into the joint by capillary attraction [71]. Larger capillary attraction forces occur as the size of the gaps to be joined is decreased. Brazed joints retain a comparatively high tensile strength, can repel liquid and gas and withstand vibration and shock during operation [72].

Successful brazing will occur if the filler metal sufficiently wets the parent material. Wetting defines the spread of a drop of liquid filler metal touching a solid metal surface [72]. To promote sufficient wetting of the parent material, the material surface must be clean and oxide free. Further, sufficient heating of the filler and base metals and low-viscous capacities of the molten filler metal will promote good wetting of the base metal. Another mechanism important for successful brazing is diffusion. During the brazing process, the filler metal partially alloys with a thin layer of the base metal surface and the migration of metal atoms between the metals is termed diffusion. As a result, the filler metal should contain a metal that is a constituent part or contains an alloying element of the base material [72, 73].

2.10.2.1 Filler Metal Considerations for Joining Stainless Steel

Considerations for selection of an appropriate filler metal include the component operating temperature, the types of metals to be joined, type of brazing process and atmosphere, the required strength of the joint and the required corrosion resistance for successful operation. There are various filler metals that can be used for the joining of stainless steels with melting points ranging from 620 - 1205℃, see Table 3. Low temperature silver-brazing alloys, containing at least 40% silver, produce good results owing to good capillary flow and the ability to bond to most stainless steels [69]. Silver based brazing alloys are categorized as low temperature brazing alloys, requiring less heat input into the joining process than other alloys with different metal constituents.

Nickel based brazing alloys require a significantly higher brazing temperature for the bonding process but retain suitable high temperature chemical and physical properties while remaining compatible with other alloying elements [71]. Copper is another filler metal used for the joining of stainless steel, providing good wetting of the base metal and good corrosion resistance. Gold based filler alloys provide good oxidation and corrosion resistance while additionally being applicable for operation within elevated temperatures, but suffers from a significant market price, limiting the viability of its use [71].

All of the aforementioned filler metals are applicable for the desired operating temperature (>180℃) but the high process temperatures required may induce difficulties in providing the required equipment and process requirements to facilitate the joining process. Further, excessive heating at high temperatures may induce annealing effects in the base metal and cause additional detrimental effects to the mechanical and thermal properties of the coated fibre itself. Nickel would be the most suitable alloy base material for bonding stainless steel to the nickel coated fibre and likewise, a copper-based alloy would be beneficial for joining a copper coated fibre. However, both these metals have high brazing temperature ranges, see Table 3. When considering an achievable brazing process, silver-based alloys are the most intriguing in terms of their physical properties and process temperatures with a brazing temperature range of around 620-980℃. However, the strength of silver based soldered or brazed joints falls off significantly as the operational temperature approaches around 260℃ which remains a good estimation of the maximum permissible operating temperature of silver based brazing alloys [70].

Filler base material	Nickel	Silver	Gold	Copper
Braze temperature range	927-1205℃	620-980℃	890-1230℃	705-1150℃

Maximum operating temperature	980°C	370°C	800°C	370°C
Features	• Good corrosion resistance. • High service temperature • Requires vacuum. • Brittle	• Does not require an inert atmosphere. • Can be used with all brazing techniques	• Good corrosion resistance and strength at high temperatures • Applications in electronics and aerospace • Expensive	• Require inert atmosphere. • Cheaper alternative to other filler materials

Table 3 - Brazing temperature range and maximum safe operating temperature for brazing alloys used for stainless steel joining, data taken from [70] and [74].

2.10.2.2 Brazing Atmosphere

High temperature brazing processes conducted in open air induce chemical changes in the heated metals such as oxide formation, scaling and carbon buildup on the part surfaces [73]. Fluxes are used within soldering and brazing to remove surface oxides and inhibit the effects of oxygen on the brazing surfaces, preventing renewed oxide formation. However, the flux must be fully removed post-brazing as flux residue is chemically corrosive and will weaken the material bond [72]. This cleaning procedure may induce complications with removing the flux from underneath the fibre after the thermal joining process.

A controlled atmosphere composed of an inert gas, such as argon or nitrogen, can mitigate the issues associated with open air brazing and eliminate the requirement of a flux and post-process cleaning procedure. The composition of the gas used depends on the metals to be brazed and the chosen brazing method. Further, certain steels may react with nitrogen at high temperatures, limiting its viability for use as a shielding gas for joining metals of this type. Conducting the brazing procedure within a vacuum furnace further aids in this regard while remaining more suitable for higher melting point filler metals such as nickel based brazing alloys.

2.10.2.3 Incorporating High Temperature Brazing into Fibre Embedding Procedure

Direct embedding of metal coated fibres into SLM manufactured parts results in voids below the fibre, weakening the bond of the fibre and the overall strength of the part, see Figure 16, left image. This degree of bonding may be sufficient for temperature sensing applications, where the sensing fibre is strain isolated from the structure. However, the fibre-metal interfacial bond must be without voids or pores for strain sensing applications [75].Brazing can be incorporated into the embedding process to help counteract the underside bonding issue.

Mathew et al., improved the bonding between a nickel coated capillary and a groove manufactured from SS-316L by introducing an intermediary high temperature vacuum brazing process using a Ni-Cr-Si-B-Fe filler metal, applied to the groove in paste form [18]. The nickel coated capillary was damaged during the continued SLM process, but the bonding of the underside of the capillary to the groove was significantly improved. Ni based brazing alloys are well suited to high temperature applications with a maximum service temperature of around 980°C. Further to this, high Ni content will allow for good intermixing with the Ni fibre coating and SS-316L groove but requires significant brazing temperatures to achieve.

Silver based brazing alloys offer a low temperature alternative but retain a reduced maximum service temperature when compared to other brazing alloy base metals [71]. Similar work was conducted by D. Havermann [12], whereby a nickel-based filler material was applied underneath the fibre in the form of a thin amorphous brazing foil. After the brazing procedure, the bonding of the underside of the fibre to the groove was substantial when compared to direct embedding procedures, Figure 16. This work demonstrates the feasibility of incorporating high temperature brazing into the fibre embedding process chain.

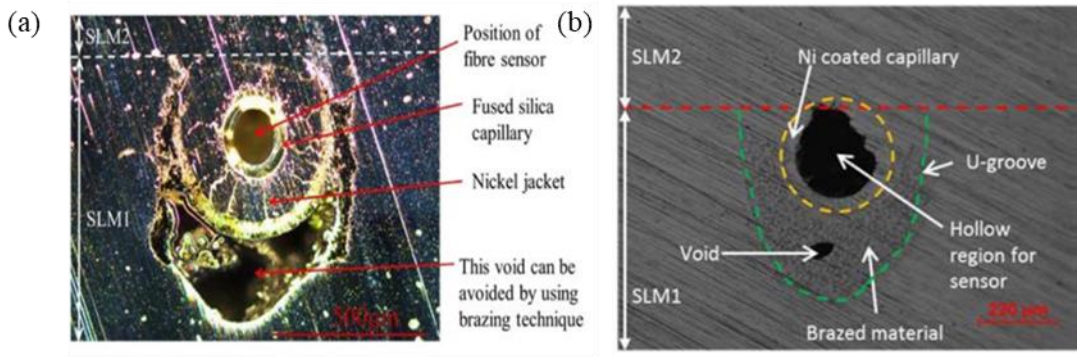

Figure 16 – Comparison of direct embedding resulting in (a) a void beneath Ni fibre and (b) improvement as a result of addition of brazing process [18].

2.10.2.4 Brazing Methods and Heat Sources

The selection of a suitable heating method for brazing must be conducted with relevance to the required properties of the joint, availability of equipment and the parent metals to be joined. The most applicable forms of brazing for bonding a metalized fibre into a groove are furnace brazing, induction brazing and vacuum brazing. Within furnace brazing, parts are typically loaded into the heated space containing a protective atmosphere, usually formed of a hydrogen-rich gas. This gas reacts with films on the parts being brazed and aids in their removal. However, suitable fume extraction must be present due to an explosion risk associated with highly reducing atmospheres [76].

Disadvantages associated with this technique are the potential for uneven part heating, extended heating cycle, inefficient operation, fibre survivability and operating costs and furnace size which influence practical sample sizes. Vacuum brazing is typically used for high temperature brazing of corrosion and heat-resisting alloys. As a result it is suitable for brazing high alloy steels, nickel alloys and other reactive metals [76]. However, the technique suffers from a high capital cost and slow heating cycle times. The purpose of the vacuum is simply to ensure surface cleanliness of the part and to allow the filler metal to flow without the use of a flux. Induction brazing holds the most promise as a potential heat source for the application of fibre embedding. Induction heating works by passing an alternating current through a coil placed close to the part to be heated. Passing an alternating current through the coil in this way creates a secondary current that is induced into the part, producing heat. Benefits of this technique are the ability to braze all electrically conducting materials within all the required temperature ranges. Further, it is also suitable for both open air and protective atmosphere brazing which promotes its viability for investigating different parent material and filler alloy combinations [73, 76].

Using induction brazing, the heat can be localised to the area of interest on the part, uniform part heating can be achieved and heating cycle times are fast in comparison to other brazing techniques [76]. These advantages coincide with the desirable process parameters required for successful brazing of a metalized fibre into a groove that demands fast and controllable heating cycles and uniform part heating.

2.11 Chapter Discussion

The literature and background review provides a detailed review into the state of the art of embedding optical fibre sensors within additive layer manufactured components. It highlights the complications and difficulties associated with embedding sensors within high melting point metals such as SS-316 and provides a basis for the ensuing thesis that will look to devise a fibre embedding process procedure for the purpose of embedding optical sensors within SS-316 coupons for the application of condition measurement within harsh environments.

Further to this, the review ascertained the most applicable sensor type (FBG) and ALM process (SLM) required to achieve its objective. In addition, it was possible to determine suitable secondary fibre metallisation and intermediary metal joining processes that will be required to meet the project needs. These additional processes require complex mechanical systems to be designed, manufactured, and characterised for the purpose of fibre embedding procedures.

ALM manufacturing retains benefits for embedding as it allows for access to all areas of the part, process interruption for sensor embedding to be performed, and modification of build parameters at each layer to accommodate certain features, such as elevated edge and balling reduction, and for sensor survivability [12, 20]. Further, when used to print metallic components, it reduces the heat interaction to the sensor when compared to other metal forming techniques, and the small spot sizes achievable allow for good resolution within part formation. Using the SLM additionally allows for the inclusion of layer re-melting procedures in-situ of the build process, which has desirable effects for reducing surface defects and porosity [77, 78, 79].

The benefits of using optical sensors were illustrated in terms of their small form factor, resistance to electromagnetic interference, and sensing performance when compared to electrical sensors. FBGs retain further benefits for embedding as they cater for multiplexed sensor networks and distributed sensing arrays by use of wavelength division multiplexing that can be used for multiple parameter sensing [44]. Further to this, some FBG types are applicable for sensing within elevated temperatures and harsh environments [28].

While sensor embedding within SS-316 structures has been reported before [43], the development of a reliable fibre embedding process procedure with specifically designed systems to allow for full investigation into the process parameters and challenges within each stage of the process would offer greater insight into the process and is an objective of this thesis.

Commercial systems do not allow for process modification or interruption, and therefore are unsuitable for this research. This challenge requires the development of bespoke systems optimised for fibre embedding in order to gain a full understanding of the associated requirements and challenges, in order to produce a repeatable and reliable fibre embedding process.

2.12 Thesis Objectives

The literature review defines the processes and associated difficulties in embedding optical sensors within high melting point metals. The thesis objectives follow on from this investigation, using the analysis to devise a fibre embedding process procedure which provides a basis for the development of systems required to conduct it effectively. Therefore, the thesis will follow the sequential process of conducting the fibre embedding procedure, each stage of which will be investigated in order to gain a better understanding of the embedding process as a whole, and the difficulties and limitations for achieving it effectively so that a reliable process chain can be defined and taken forward into commercialization.

A SLM system was designed and manufactured for the purpose of fibre embedding, see Chapter3 Section 3. It will be designed in such a way as to allow for full access and adaptability of the build at any stage of the process to ensure that the desired functionality is achieved for all the required process parameters and features present within coupon design, successful embedding, and sensor survivability. Further to this, full modifiability of the SLM parameters within each layer is desired to allow for full calibration of the system specific for fibre embedding process needs and also for laser polishing procedures to become possible using the same system, see Chapter 3 Section 6.

In addition to a bespoke laser processing system, it is imperative to modify and calibrate a pre-existing RF sputter deposition system for the purpose of depositing a uniform conductive thin film ($\approx 5\mu m$) of chromium onto a fused silica fibre, see Chapter 4 Section 2. This conductive coating will be used as a seed layer for electroplating a protective nickel jacket onto the fibre, which will be achieved by the design, development and calibration of a nickel electroplating system capable of depositing a 350-500μm thick uniform nickel coating onto a 130μm chrome-coated fibre, see Chapter 4 Section 3.

The induction brazing process will be investigated further to aid bonding of the underside of the metallised fibre into the coupon groove, see Chapter 6. This will lead to the development of an induction brazing system capable of inert-gas brazing of various different brazing alloys for the purpose of dissimilar metal joining using SS. This system will then be used to ascertain the feasibility of incorporating the induction brazing process into the fibre embedding process chain, define the limitations and required functionality of such a system required in order to conduct this effectively within the financial, logistical and safety constraints of the project.

The success of the entire fibre embedding process chain will be achieved by conducting extensive testing of FBGs embedded inside SS-316 coupons, consisting primarily of elevated and extended temperature cycling experiments, see Chapter 5 Section 3. This will allow for the correlation of the grating sensitivity, which can be used for temperature correlation within operation. In addition to this, these experiments will ensure the applicability for using the embedded FBG within the projected operational temperature requirements ($-10°C - 180°C$).

Temperature cycling experiments will be followed by the development of strain isolated embedded FBGs to allow for future work into strain testing experiments, see Chapter 5 Section 4. This will include the definition of techniques and methodologies required to provide mechanical strain isolation of embedded FBGS and therefore temperature and strain discrimination of sensed stimuli.

Chapter 3 – Metallic 3D Printing using Selective Laser Material Processing

This chapter details the design and manufacture of a SLM system suitable for fibre embedding experiments. It goes on to detail system modifications and optimisation of the process parameters for achieving good quality printed layers. Further, the benefits of incorporating a layer re-melting procedure at each material layer is illustrated, compensating for hardware limitations for achieving low porosity parts with reduced surface roughness, setting the foundations for ensuing fibre embedding investigations to take place.

3.1 Introduction

3D printing originated as a method of prototyping parts, allowing designers to visualise design concepts and features in timeframes not feasible using other prototyping methods [19]. As the industry has developed, 3D printing expanded from producing parts for visualisation of concepts to include manufacturing functional parts in a variety of materials including polymers, ceramics and metals. It is now possible for 3D printed metals to produce parts exhibiting properties similar to their martensitic material equivalent, however, defects can arise as a result of the manufacturing technique that must be quantified and mitigated in order to achieve good material properties for industrial operation.

For the manufacture of metallic components, the ALM process in principle provides access to any point of the component during manufacture, which is beneficial for the embedding of sensors inside functional components. Further to this, parts with complex geometries and internal features, unobtainable through conventional forms of metal manufacture, become feasible when using ALM technologies [20].

In the SLM manufacturing process, see Figure 17, a three-dimensional component is manufactured by building up a number of two-dimensional layers. These layers are fabricated from a powder layer deposited on a build plate within an inert atmosphere which is illuminated by a high-power laser to selectively melt the powder in accordance with the geometrical data of the build layer, as defined by the 3D CAD model. The build plate lowers within the Z coordinate plane by an amount defined by the layer thickness and the process is repeated until a final part is produced. The SLM is capable of achieving small feature resolution due to the small laser spot size and fine powders used, with micro-SLM systems capable of feature sizes of 15-20µm [80]. This promotes the suitability of SLM for the application of fibre embedding as the melt pools are small, limiting heat interaction through conduction with the surrounding material [12].

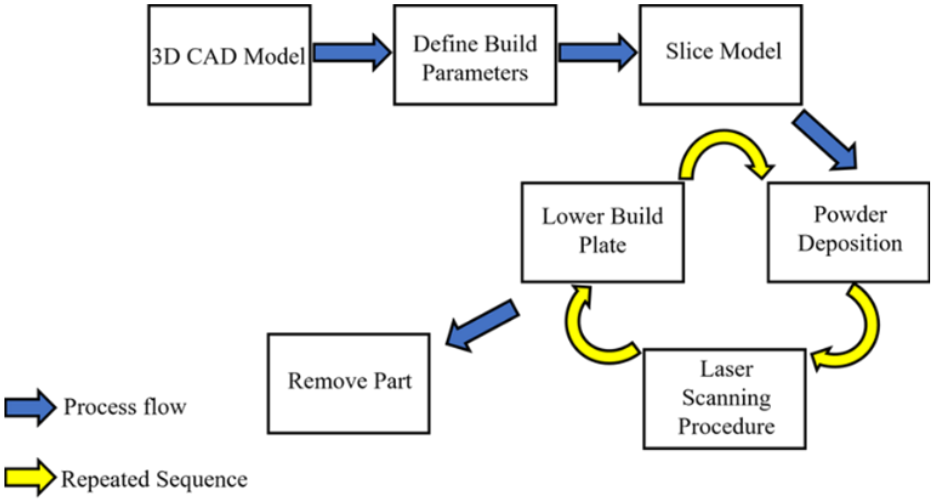

Figure 17- Process flow for the selective laser melting process.

3.2 Selective Laser Melting System Specifications

Embedding optical fibre sensors in metallic components built up using SLM requires a high degree of process accessibility and adaptability, see Chapter 2 (Section 7). Commercial SLM systems typically do not permit interruption to the build process and this dictated the need to design a bespoke SLM system with the capability to conduct fibre embedding investigations.

3.2.1 Design Specifications

It is a fundamental requirement of the system to have the capability to modify the build parameters during the build process. This has specific relevance for calibrating the optimal process parameters and additionally for altering the parameters mid-process during the embedding procedure, required to reduce the energy density for the first material layers deposited over an optical fibre. The parameters of merit for laser melting are the laser power, scan velocity, layer thickness and hatch design, see Chapter 2 (Section 9). In addition to SLM procedures, the system needs to be flexible enough to be capable of laser re-melting and polishing to improve the density of manufactured parts, reduce surface roughness and aid bonding of the fibre to the bulk material, see Chapter 3 (Section 6).

A literature review [12, 19, 20, 60, 79], allowed the parameter ranges required of the self-made system to be determined. The results of this investigation are highlighted in Table 4, giving the parameter specifications of the laser processing system. An SPI-100 100W fibre laser is used as the primary energy source for the system and is capable of continuous wave and modulated continuous wave operation. The scan head is controlled by the laser processing software Raylese weldMARK 2, allowing for full modifiability of the process parameters on a layer-by-layer basis.

Process Parameter	Value
Laser Power	10-100 W
Scan Velocity	50-300 mm/s
Layer Thickness	30-100 µm
Hatch Spacing	25-500 µm
Build Atmosphere Oxygen Concentration	< 1%
Inert Gas Volumetric Flow rate	5-25 l/min

Table 4 - Laser Processing System Required Process Parameters, data from Chapter 2 Section 7, [12], and preliminary investigations.

3.2.2 Motorized Motion Control

The SLM process dictates that the build area must be lowered in increments correlating to the desired layer thickness of the part, usually defined as an amount greater than the largest particle size of the metallic powder, given by the powder suppliers specifications. This movement must be reliable and accurate to a few microns as the lowest achievable layer heights are defined as being just greater than the largest powder particle size (36-50µm) [81]. Further to this, the powder deposition process must operate within an inert atmosphere and be capable of depositing a uniform layer of powder over the build area. Vertical movement of the build area was provided by a 'Standa motors' motorised vertical stage, 8MVT100, while transverse movement of the powder deposition system was provided by a Standa motors motorised linear stage, 8MT175. Both motor stages were connected to a Standa motors two axis motor controller, 8SMC5-USB-B9-2, which is controlled using XiLab software, allowing for the motors motion to be automated.

While the vertical stage was reliable within the negative Z-Axis with repeatable step increments for layers heights of ≥50 µm, this consistency was not transferable to the positive direction. However, as the build process only requires movement within the negative Z-axis, this was not deemed to be in detriment to the system's performance. In later tests the resulting part features and surface roughness were seen to be the dominant factor that defined the minimum achievable layer resolution, see Chapter 3 (Section 5).

3.2.3 Fibre Positioning

Reliable positioning of the fibre into the SLM part is imperative for the embedding process. It must be aligned with a groove defined in the part, while not interfering with the powder deposition and gas flushing processes. This was achieved by a groove manufactured into the centre of the base plate of the SLM system, allowing the fibre to sit within the required level of the build plane and align centrally to the coupon groove.

Furthermore, the groove caters for fibre egress from the gas shield, allowing for interrogation of the FBG during the embedding process and clamping of the fibre end to mitigate the effects of thermal stresses acting to push the fibre from the groove during the embedding process.

3.2.4 Positional Consistency and Portability

The system was designed for use within a shared laboratory space in which multiple users requiring access to the fixed scan head and laser. To accommodate this, the SLM system is designed to be portable and removable as a unit. To aid repeatable alignment, optical bread boards and magnetic triangular mounting clamps were used to ensure consistency in the system's positioning with respect to the scan head. The entire system is raised and lowered using a mechanical lab-jack, allowing for the build area to be placed within the suitable focus point of the laser for laser melting procedures. A scan head, fitted with an f15 focusing lens, and a working area of $100mm^2$ (10mm x 10mm) was used for laser scanning procedures. The build height adjusted to create a spot size of 100µm, unless otherwise stated in the build parameters.

3.3 SLM System Design

Figure 9 within Chapter 2 illustrates consistent features required of all SLM systems and was used as a base for the design of the manufactured laser processing system is shown in Figure 18, where Figure 18(a) shows the system with the gas shield in place, and Figure 18(b) removes the gas shield to show the internal features of the system. The notable features of the design are highlighted within the figure and are discussed within the following sub-sections.

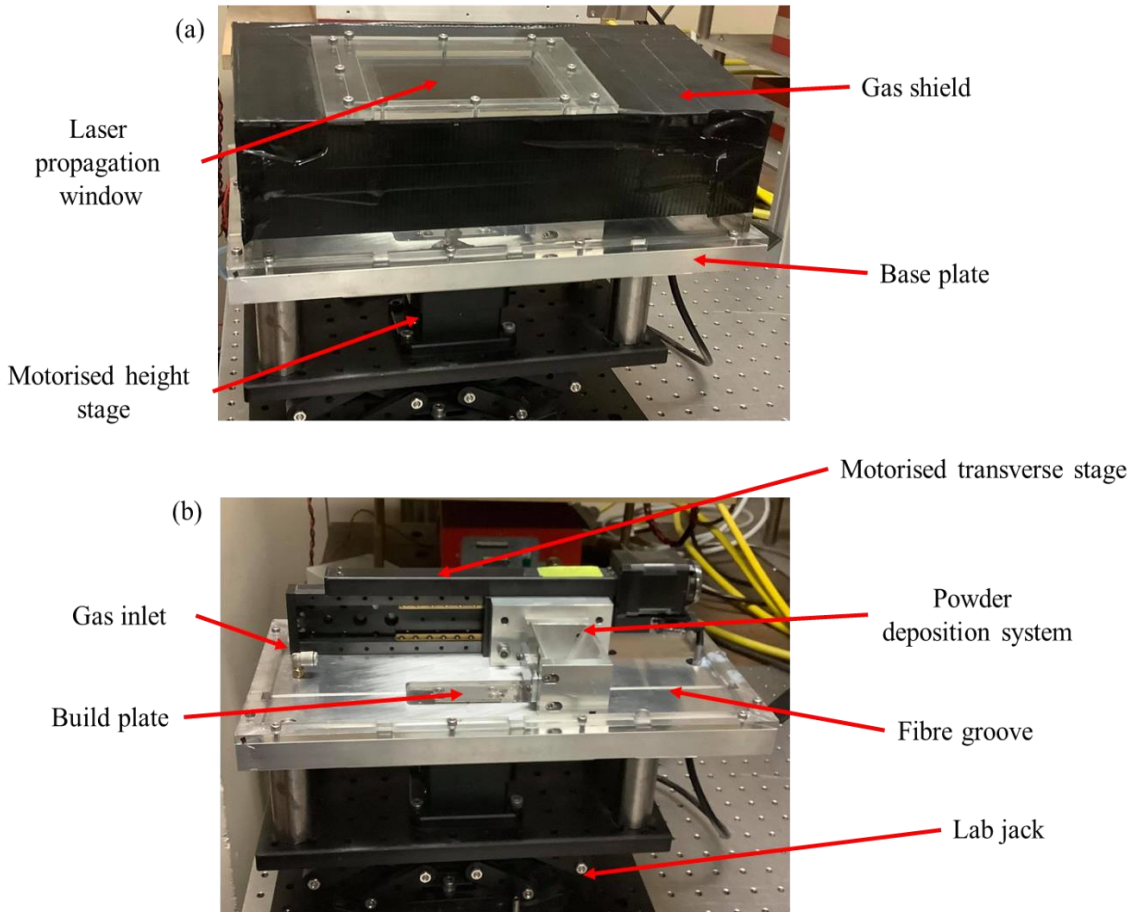

Figure 18 - Bespoke Laser Processing System Design. (a) shows the system with the gas shield with protective black tape to prevent laser light escaping through the side walls. (b) shows the system without the gas shield, illustrating the notable features of the design.

3.3.1 Base Plate

The base plate provides a platform for mounting of the powder deposition system and the gas shield. It also provides a flat reference plane for the powder scraper, important for achieving flat, uniform powder layers.

The base plate itself is manufactured from machined aluminium that was ground to ensure a flat finish. Aluminium was chosen because it provides enough toughness and heat resistance while being lightweight and easy to machine. A CAD model of the base plate is illustrated in Figure 19. Important features of the design are numerically highlighted, and their function is tabulated in Table 5.

Number	Function
1	A hole for positioning of build plate with respect to the fibre groove and fixing to motor Z stage
2	A groove for fibre alignment and for maintaining the fibre below the build height during the SLM process
3	Counter bored post fixing poles for connection of the base plate to motor stage assembly
4	M6 hole for connection of Argon gas line

5	Slot for cable access to the system
6	M6 holes for connection of powder deposition assembly via angle brackets
7	M3 holes for gas shield connection
8	M3 holes on underside of base plate for the attachment of a rubber sheet to aid in preventing metallic powder falling into the Z stage motor assembly

Table 5 - table outlining the function of the numerically indicated features of the base plate design shown in Figure 19.

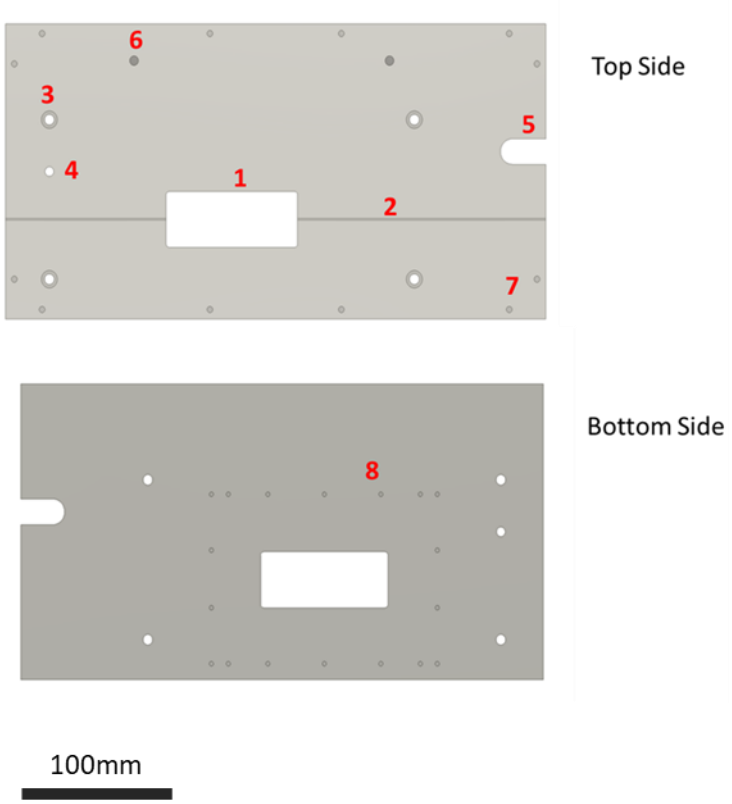

Figure 19- Base plate design with numerically marked design features, refer to Table 5 for description of the features. Design is made from ½ inch (12.7mm) thick machined aluminium, ground and polished to a flat surface.

3.3.2 Build Platform

The build plate provides connection to the Z-stage and a flat surface for the deposition of powder and defines the build region. It is manufactured from SS due to its heat resistant properties and resistance to mechanical abrasion [82]. M3 holes on the top side of the build plate allow for positioning of three different sizes of sample plates while maintaining their alignment with the fibre groove. The sample plates are made from 2.5mm thick SS-316 metal plates, used as build substrates for the SLM process.

Counter-bored holes allow for connection to the motor stage to the build plate without infringing on the build height. A 3D CAD model of the build plate is given in Figure 20a), illustrating the build plate, and bottom plate assembly required for connection to the motor stage. A rubber sheet is sandwiched between the build plate and a further plate, Figure 20b), to limit metallic dust excretion from the build area. The rubber sheet has the additional benefit of reducing leakage, aiding efforts to maintain an inert atmosphere.

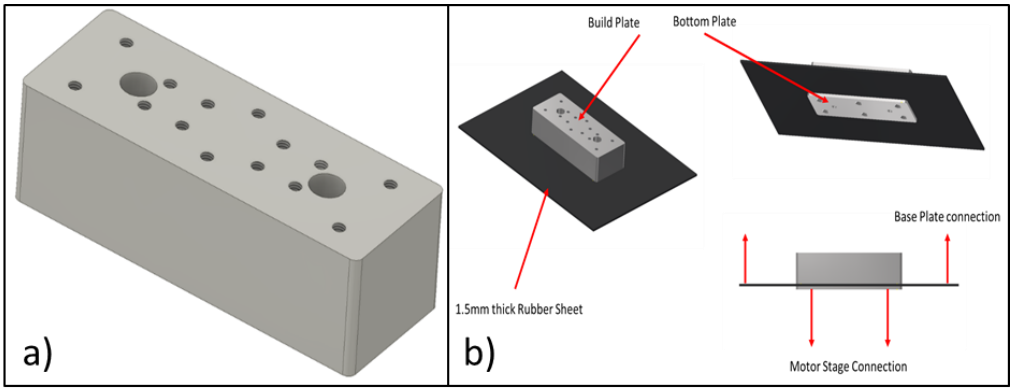

Figure 20 - a) 3D CAD model of the build plate, b) illustration of build plate, rubber sheet and bottom plate assembly to aid in sealing the system.

3.3.3 Gas Shield

The gas shield is important for achieving an inert atmosphere during the SLM process, with the ability to maintain suitable gas composition levels defined in Chapter 2 (Section 8.2).The gas shield is designed from multiple interconnecting 5mm thick Perspex sheets, laser cut into segments for assembly as shown in Figure 21. The bottom plates are screwed to the base plate, but the remainder of the gas shield is easily taken off the system for access to the build area. The top plate of the shield is angled by 10° to prohibit back reflections from entering the scan head and causing potential damage to the beam delivery optics, fibre, or laser source. This value was calculated using the spatial dimensions of the SLM system and its proximity to the scan head so that the reflected light would be directed safely into a diffuse board, see Figure 23.

To aid maintenance, the laser propagation window can be easily removed and replaced as required and is fixed in place by a simple Perspex bracket and M4 bolts, see Figure 22. The propagation window is made from Borofloat glass which is well suited for applications involving laser propagation [83].

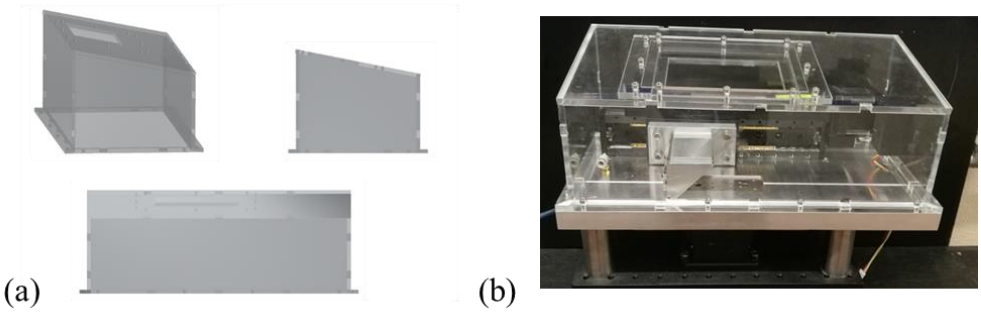

Figure 21 - a) 3D CAD model of gas shield design, b) manufactured gas shield mounted on the system.

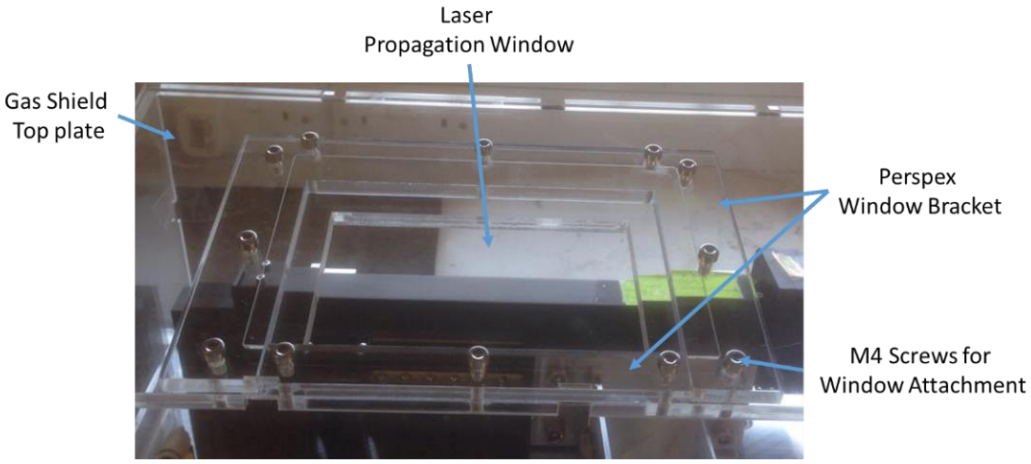

Figure 22 - Laser propagation window and bracket assembly.

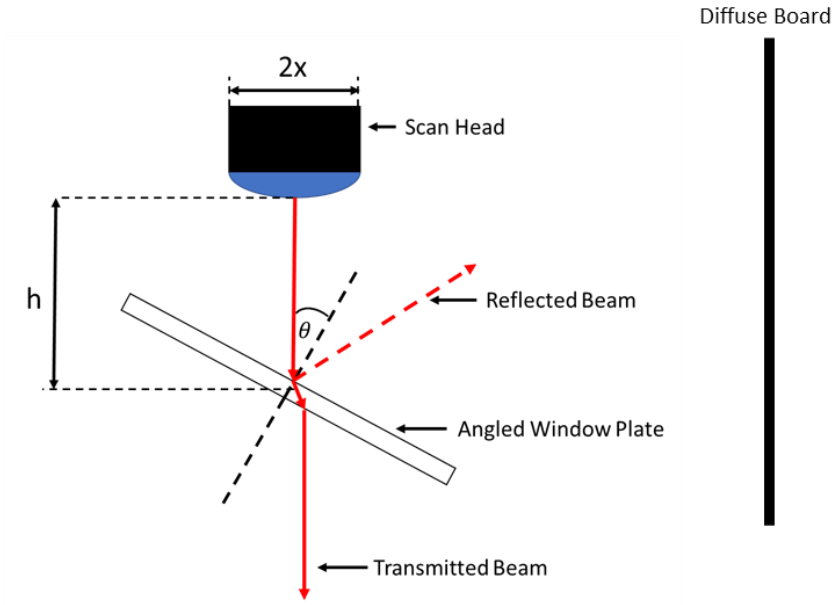

Figure 23 - Schematic illustration of angled gas shield showing method used for calculation of required angle.

3.3.4 Powder Deposition System

The powder deposition system consists of a powder spreader assembly connected to a motorized translational stage, see Figure 24. A powder reservoir deposits powder as the stage moves in one direction and the scraper blade spreads the powder flat as it traverses in the opposing direction. The scraper blade itself is interchangeable, depending on process requirements that may dictate the need for a "hard" or "soft" scraper blade. Both forms of scraper have benefits and flaws regarding the printing process in trying to achieve uniform depositions of powder.

Hard scraper blades are more suited for achieving uniform depositions. However, they are susceptible to catching on raised surfaces of the printed part. This can result in discontinuities in the powder spreading deposition and detachment of the part from the build plate during the SLM process. Further, connecting with the printing part causes indents on the scraper blade, promoting difficulties in achieving a homogenous powder layer. Soft scraper blades pass over raised features without disrupting the powder or catching on raised part surfaces that would be in detriment to the build process. However, they may not be as proficient in achieving uniform powder layers. The blade's positioning is aided by the base plate and an indented groove on the wall of the powder reservoir to ensure a flat surface for scraping powder.

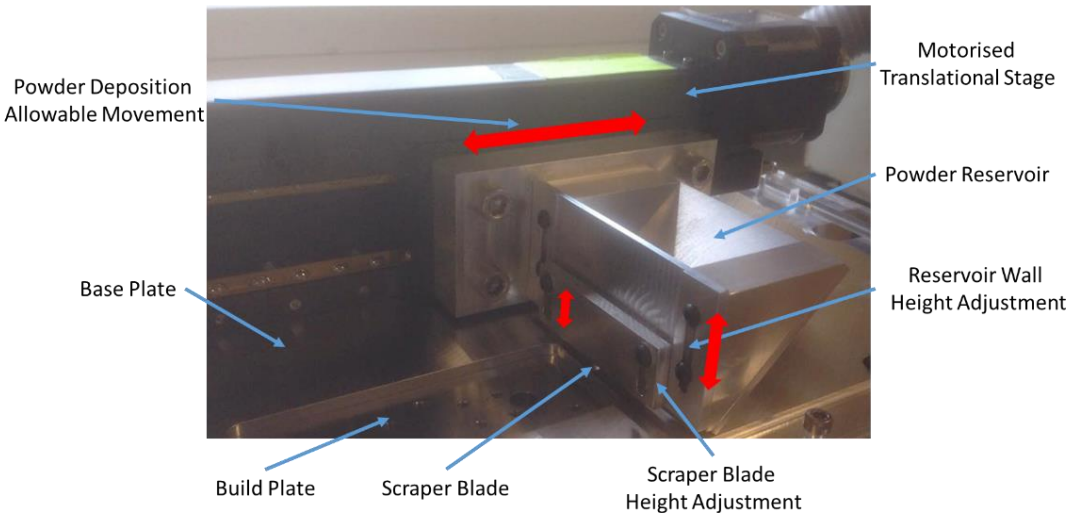

Figure 24 - Powder Deposition System Design.

3.3.5 Revised Powder Spreader Design

During initial system testing, it became clear that there was the need for design alterations to the above powder spreader system. Powder was seen to clog the exit beneath the reservoir, preventing powder from being deposited in a controlled manor. This phenomenon was directly contributed to the amount of powder within the reservoir. However, reducing the amount of powder in the reservoir was not an option as it is required to have sufficient powder available within the system to carry out the full build process without interruption (which would require removal of the gas shield and, as a result, re-purging of the build atmosphere). Alternatively, if the exit hole is too large for the powder build, then it will escape the reservoir before it is required, inhibiting the process as more powder would be required throughout the process to replace this wastage.

To counteract this issue, a redesigned powder spreader included a system in which the width of the deposition channel at the bottom of the reservoir can be varied between 2mm and 6mm, allowing for the appropriate size to be used depending on the powder characteristics and the amount of powder required by the build process.

A further iteration to the design is in relation to the scraper blade's operation. The previous design had a single scraper that could either be "hard" or "soft". The new design exhibits multiple scraper blades. The hard blade on the front of the system is still a feature, however, this is now with additional soft scrapers, defined at differing heights on the underside of the deposition system, to obtain benefits from both forms of powder scraping. This new design allows for the powder to be spread on both the forward and back motion of the system, instead of just the back motion as in the previous design. Further, the blades are defined at staggered heights, see Figure 25, to prevent contact with the hard scraper with the top of the printed part and promote a smooth deposition of the powder. Even with these design alterations it is important to regularly change out the scraper blades to ensure that the deposition process remains consistent. The new powder spreader design mounted on the laser processing system is illustrated in Figure 26(a) and a 3D model showing the individual parts of the design is illustrated in Figure 26(b).

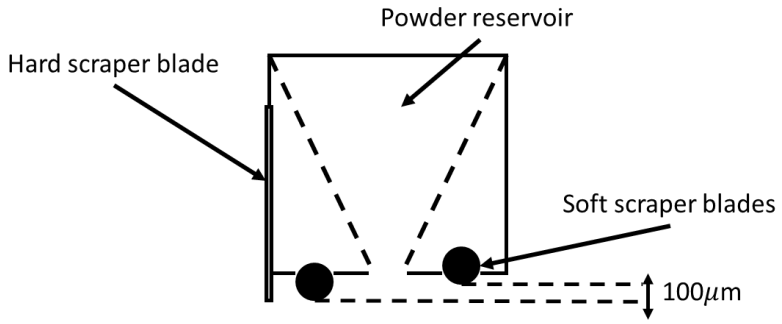

Figure 25 - schematic view of the profile of the new powder scraper system.

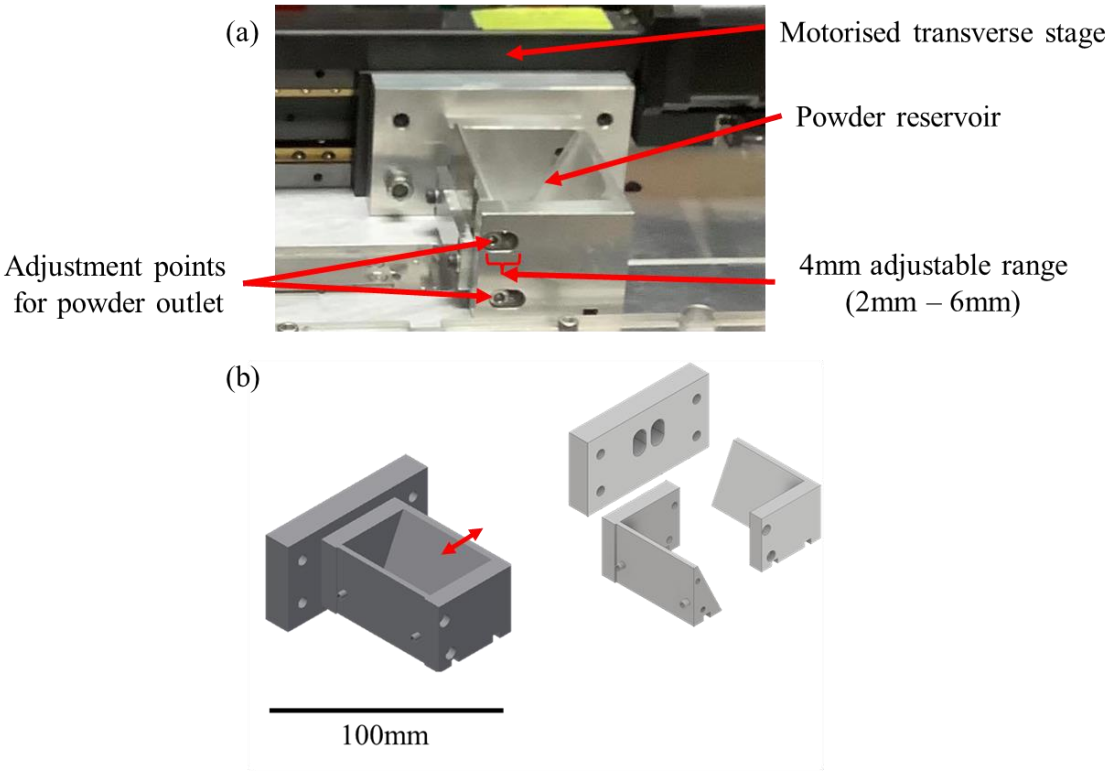

Figure 26 – (a) Image of the new powder spreader mounted onto translation stage. (b) 3D model of new powder spreader design. Red arrow indicates the plate which can move to increase/decrease width of deposition channel.

3.4 Design modifications

Over the course of the project, it became apparent that the stability of the lab jack was insufficient to maintain the required alignment with the laser over extended periods. Figure 27 illustrates a cross section of the SLM system. The base plate is required to provide a flat plane of reference for the powder deposition process and must be levelled to produce a uniform powder layer which is flat with respect to the laser scan head. Further to non-uniform powder layers, this lab jack movement results in localised discontinuities in the focal plane of the laser due to mismatch in height of different regions of the build area, resulting in poor part formation, see Figure 28.

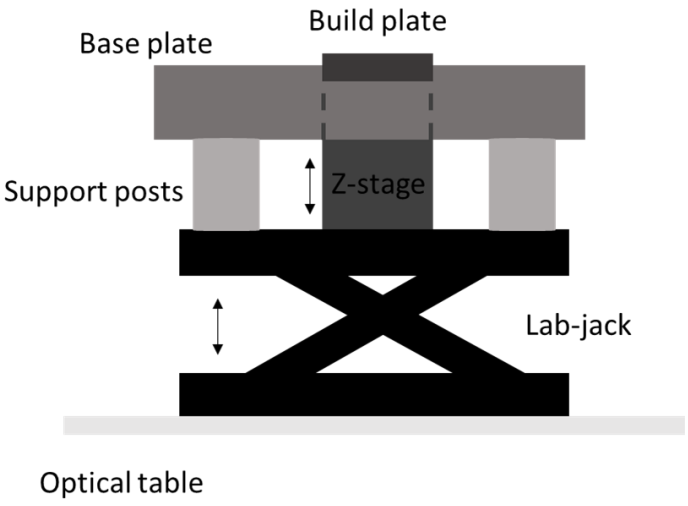

Figure 27 - Schematic illustration of the cross section of the SLM system.

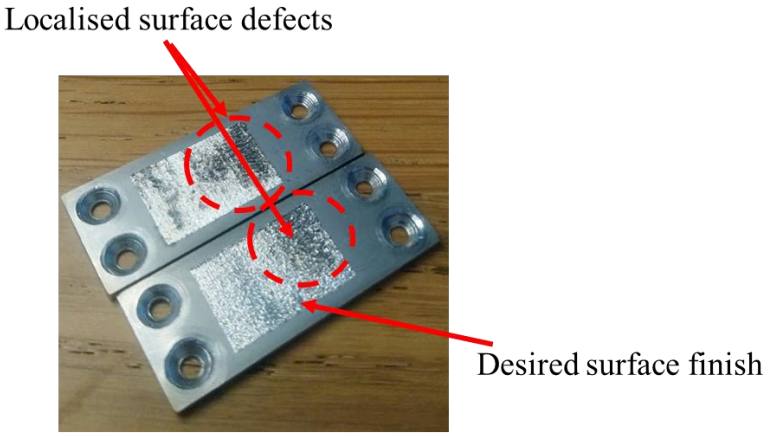

Figure 28 - Examples of printed layers containing localised discrepancies associated with system levelling and discontinuity in the focal plane of the laser. Highlighted areas feature discoloration and poor layer formation.

Because the entire system is lowered and raised using the lab-jack, the system was susceptible to external perturbations, resulting in issues with maintaining the alignment with respect to the laser source. This was addressed by the addition of a four-point locking method installed between the base plate and its support struts, as shown in Figure 29. The base plate position can be altered using the threaded rod and locked in place using locking nuts. This isolates the baseplate from external perturbations and allows for precise levelling of each corner of the base plate, ensuring a consistent focal plane for the lasing procedure. While this method required fine adjustment prior to each build process, it was successful in mitigating the poor layer formation as illustrated in Figure 28, see Figure 30.

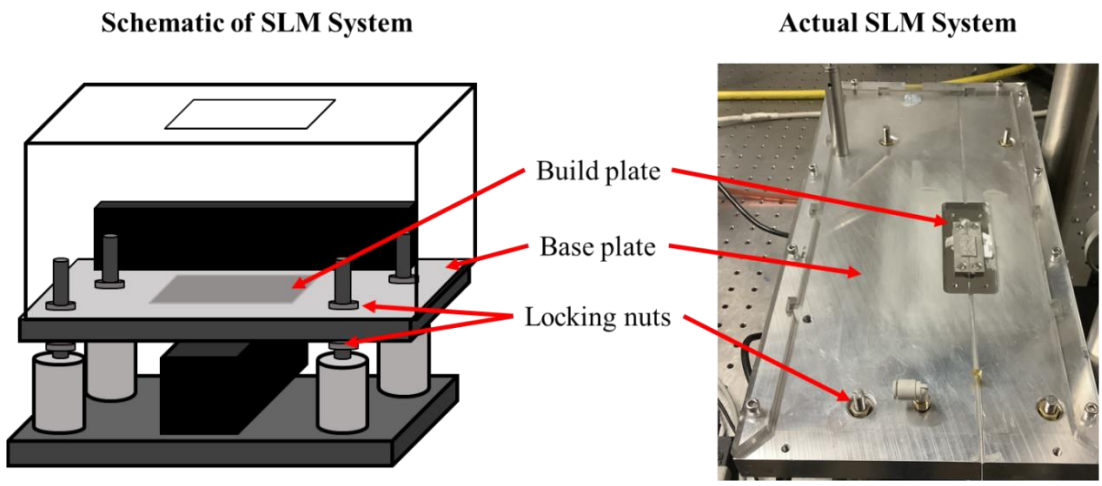

Figure 29 - Illustration of the modifications made to the SLM system to isolate the base plate for external perturbations and promote precise control of the levelling at all four corners.

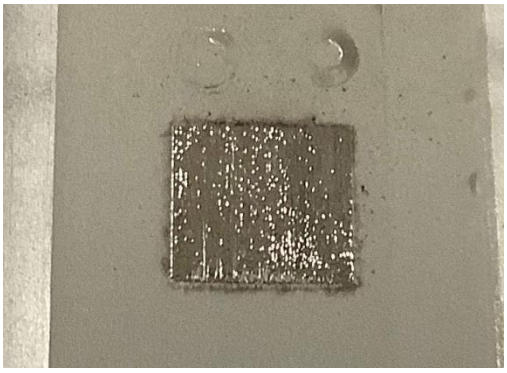

Figure 30 - Layer produced without discontinuities associated with system levelling (poor surface quality and layer formation, discoloration).

3.5 System Calibration for Optimal Process Parameters

Part density, surface roughness, geometrical accuracy and the occurrence of balling are all influenced by the build process parameters. Part density and surface roughness contribute to the final part performance. Balling is the formation of spherical and ellipsoidal balls that extend from the part surface. These can be significant in relation to the size of printed layers, with some upwards of 500µm in diameter [84], this extends higher than the build layer height and are therefore detrimental to the build process. They typically form when the melt pool becomes discontinuous, reducing the wetting ability which results in the melt pool separating into raised 'islands', forming either ellipsoidal balls approaching 500µm or spherical balls of around 10µm [84]. Their occurrence can be mitigated by limiting the oxygen within the build atmosphere, using a large laser power and a relatively low scanning velocity [84].

The laser fluence, or energy density (ED), is a useful parameter of merit for laser melting and polishing procedures, as it incorporates the laser power, scan speed and the laser spot diameter in its definition. The energy density ($\frac{\mathrm{J}}{\mathrm{cm}^2}$) is inversely proportional to the feed rate and can be calculated from equation (11) [77].

$$ED = \frac{6000P}{DV_f} \tag{11}$$

Where P is the laser power (W). V_f is the scan speed (mm/min) and D is the beam diameter (mm). As it was desired to laser polishing procedure into the SLM process with minimal interruption, the beam diameter remains consistent (100 to 200µm) for both processes.

3.5.1 Laser Power

The laser power must be sufficient to promote some re-melting of the previously deposited material, as this is important for achieving bonding between the new and preceding layers. Further, a high laser power is necessary to provide sufficient energy input to accommodate for good wetting, whereby the molten powder behaves as a liquid, and spreading, allowing reliable tracks to be deposited [84].

A diode pumped fibre laser with a maximum available average power of 100W was available for this work. The effect of optical power on the build was studied with all other build parameters held consistent. ($v = 300\frac{mm}{s}, t = 100\mu\mathrm{m}, laser\ spot\ size = 100\mu\mathrm{m}, h = 80\mu\mathrm{m}$). Where v is the scan speed, t is the layer thickness and h is the hatch spacing. At 40W laser power, there is significant balling with general poor layer formation. This is evidence of insufficient wetting and spreading characteristics of the molten powder, see Figure 31, which is still prevalent as the power is raised to 60W, see Figure 32.

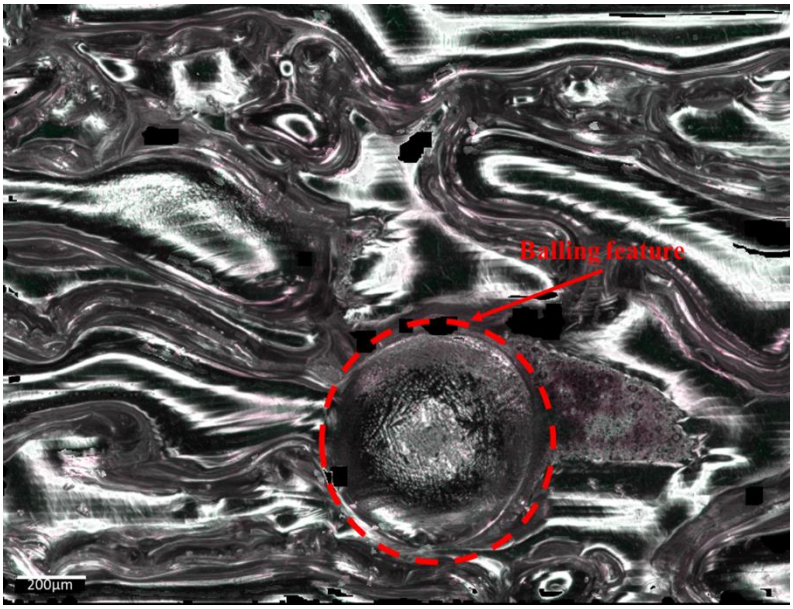

Figure 31 - Layer formation at 40W laser power illustrating balling effects. Image taken using Alicona infinite focus optical 3D measuring instrument.

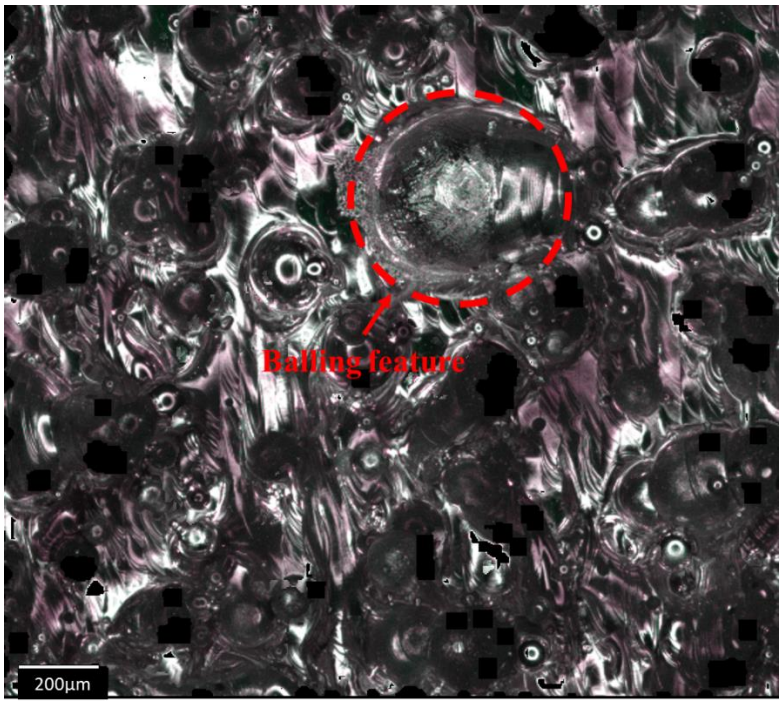

Figure 32 - Layer formation at 60W illustrating balling effects. Image taken using Alicona infinite focus optical 3D measuring instrument.

The occurrence of balling reduces as the power is raised above 60W, with improved layer formation at 80W laser power. At this power level, there is sufficient instantaneous heat input during the lasing process to promote spreading of the molten layer, with visible track formations on the part surface, Figure 33.

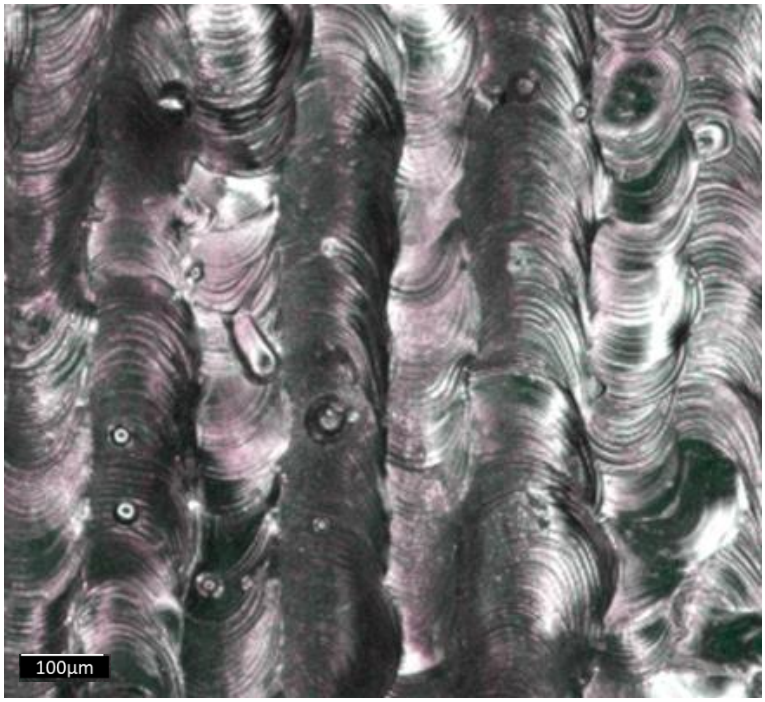

Figure 33 - Layer formation at a laser power of 80W, showing reduced levels of surface defects and visible laser scanning tracks. Image taken using Alicona infinite focus optical 3D measuring instrument.

When all other build parameters are maintained constant, the best layer formation by visual inspection (in terms of reduced balling, improved track formation and full melting of the SS-316 powder) was achieved at 100W laser power, Figure 34. The improvement in part surface compared to 80W is nominal, and it may be beneficial to maintain a lower laser power for the first layer deposited on top of the embedded sensor to improve sensor survivability at the expense of part surface finish.

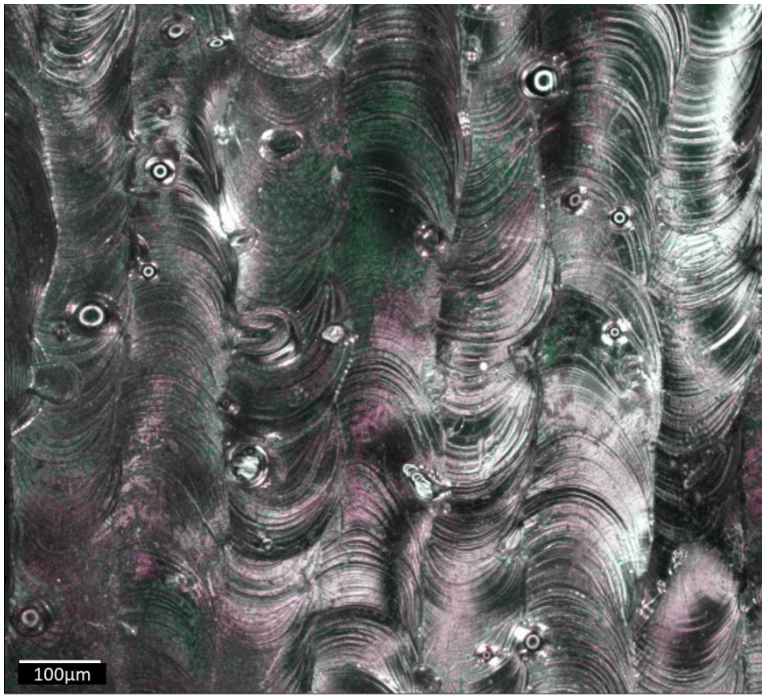

Figure 34 - Layer formation at 100W laser power. Image taken using Alicona infinite focus optical 3D measuring instrument.

3.5.2 Pulse Duration

The fibre laser used for the SLM system operates under a regime using pulsed laser light. Therefore, the pulse duration and modulation frequency must be considered as an additional process parameter. The pulse duration was varied from 50μs to the maximum permissible value of 200µs for single tracks printed using SS 316 powder, see Figure 35. The mean laser power was maintained at 100W and the scanning velocity at 50mm/s for the investigation.

With a fixed modulation frequency (1kHz), increasing the pulse duration results in the tracks becoming more uniform across their length. Therefore, maintaining the pulse duration at this value aides in achieving printed parts with good geometric accuracy and surface quality.

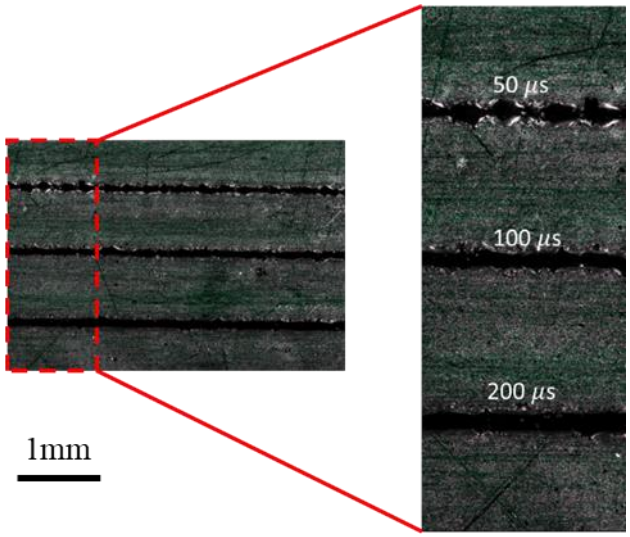

Figure 35- Single track lines printed using SS316 powder at different laser pulse durations. All other parameters remained constant (laser power 100W, scanning velocity 50mm/s). Image taken using Alicona infinite focus optical 3D measuring instrument.

3.5.3 Hatch Spacing

The hatch spacing refers to the distance between tracks within the volume of a printed layer and is an important parameter to optimise to produce good surface finish, and high density SLM parts. The optimal values are related to various build parameters and are often unique to the laser processing system's optical and mechanical set up. The most important of these are the layer resolution and the laser spot size. The laser spot size is dictated by the focal point of the build plane and the hatch spacing must be less than this value in order to avoid tracks of un-melted powder between laser scans. The difference in width of the melted track size and hatch spacing is termed the overlap percentage.

A larger overlap is ideal for reducing surface roughness ensuring suitable part density and improved layer resolution, but too large an overlap will induce excessive heat input into the part. This has specific relevance for fibre embedding, which requires limiting the heat input into the sensor during embedding in order to improve sensor survivability.

An investigation was conducted whereby the hatch spacing was reduced from 300µm to 30µm. The laser focal point was adjusted to produce a melted track width of 200µm. All other build parameters remained constant (laser power: 100W, scanning velocity: 300mm/s) in order to ensure consistent melt pool characteristics relating to the width of printed tracks. The average profile surface roughness (R_a) defines the average material height over an area defined across the part's surface. The average surface roughness was measured perpendicular to the laser scanning direction and was shown to increase with increasing hatch spacing, Figure 36. A significant increase in surface roughness occurs when the hatch spacing equals the track width ($200\mu m$) in account of trenches appearing between the melted tracks, see Figure 37. This results in poor layer formation and porous structures if the build is continued into three dimensions.

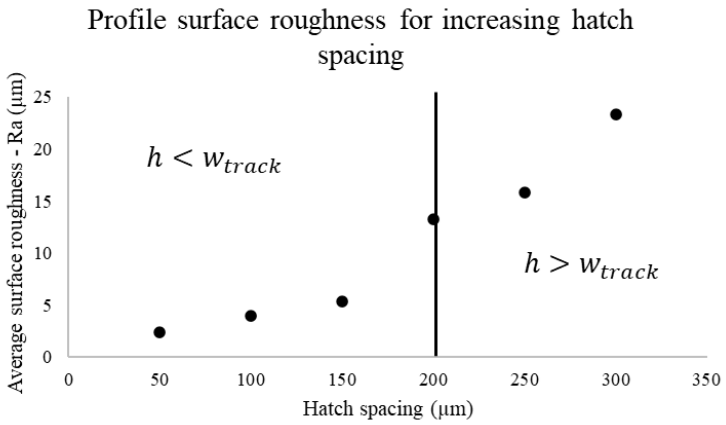

Figure 36 - Graph of average profile surface roughness against hatch spacing, illustrating point where the hatch spacing equates to the track width.

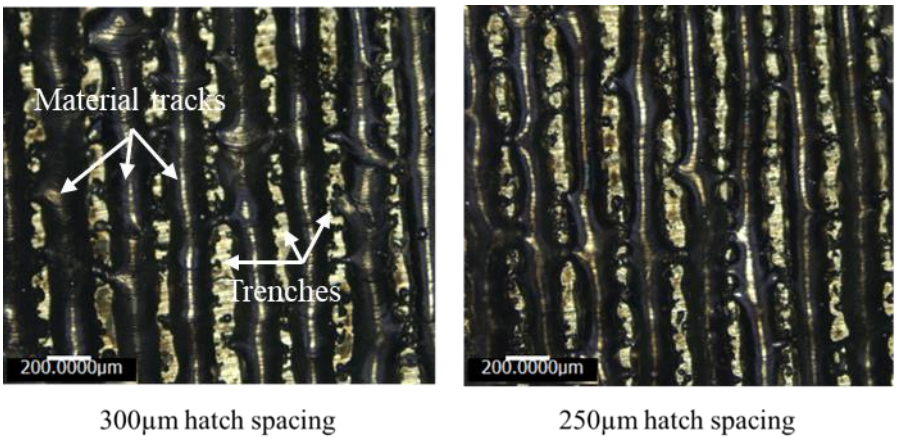

Figure 37 - Images illustrating track and layer formation for hatch spacings decreasing from 300µm to 250µm. Image taken using Alicona infinite focus optical 3D measuring instrument.

The trenches between melted tracks, Figure 37, occur due to the distance between laser scans being greater than the melted track width. This results in regions of un-melted powder between the melted tracks which form trenches once the part is removed and cleaned. An Alicona infinite focus optical 3D measuring instrument was used to measure the surface profile of the printed layers. Figure 38 illustrates the layer formation at a hatch spacing of 300µm. The trenches are clearly visible in the layer's surface profile. A cross section of the surface profile illustrates the form of the printed layer perpendicular to the laser scanning direction, illustrating the depth of trenches between each laser scan. As the bottom surface of the trench is the substrate plate, its R_a would not be a true representation of the surface roughness of a material layer and is more representative of a series of single tracks. Therefore, R_a was only measured and compared for material layers with track overlaps (the percentage by which a track overlaps the previous track) ≥ 0%.

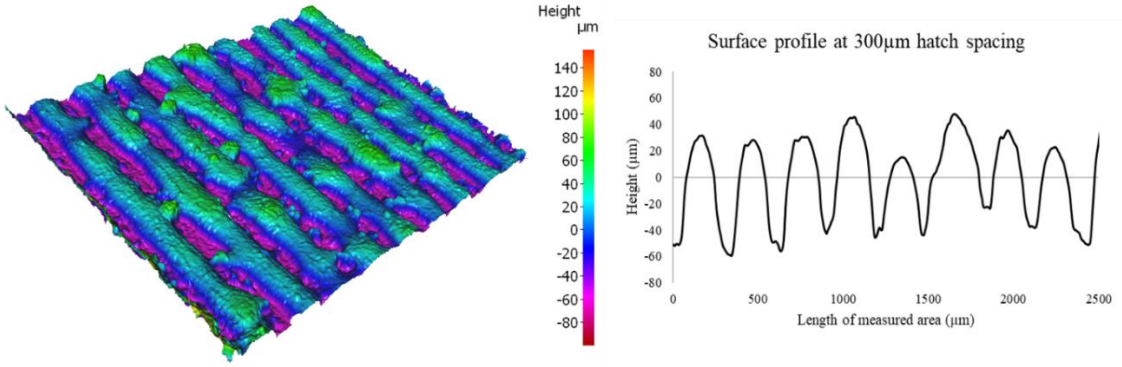

Figure 38 - Surface roughness profile at a hatch spacing of 300µm showing poor layer formation and trenches appearing between melted tracks. Surface plots generated using Alicona infinite focus optical 3D measuring instrument.

At a hatch spacing of 200µm (0% overlap), the trenches no longer reach the substrate plate, but are still prevalent as the melted tracks dip towards their outer periphery. This results in poor surface finish and a measured R_a of 13.3µm, which is significant considering material layers can be as small as 30µm. Therefore, the surface roughness is large enough to inhibit the deposition of subsequent powder layers and may affect part density. Defining a hatch spacing with 0% overlap exaggerates irregularities in track deposition, see Figure 39 and Figure 40, resulting in dips in material level between melted tracks, highlighting the need to overlap material tracks to improve surface finish.

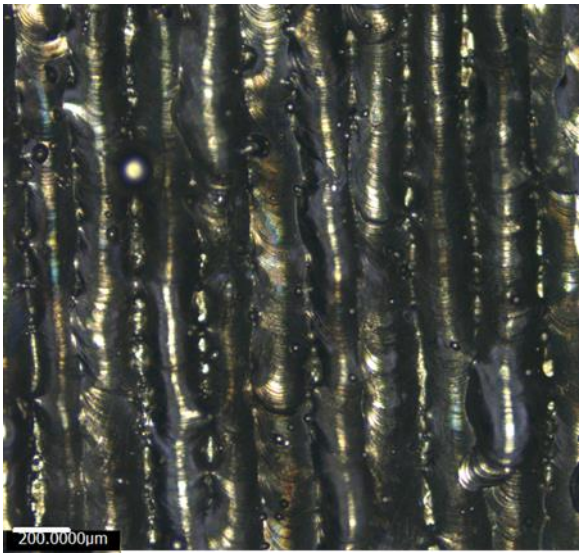

Figure 39 - Track and layer formation for a hatch spacing of 200μm (0% overlap). Image taken using Alicona infinite focus optical 3D measuring instrument.

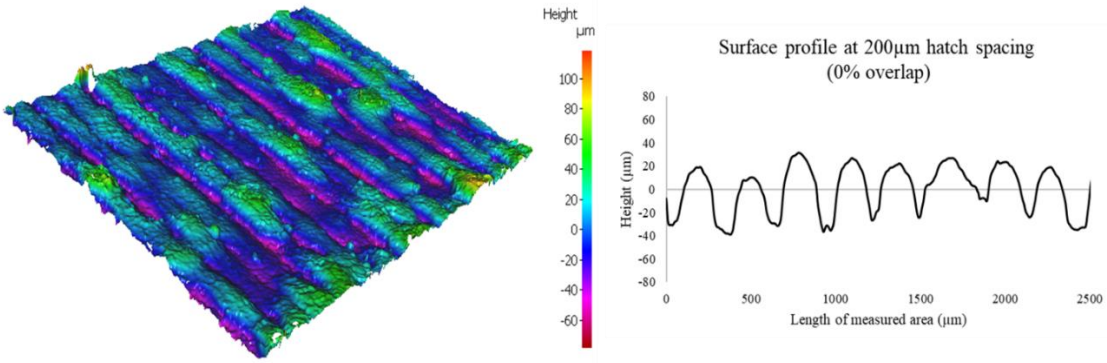

Figure 40 - Surface profile for a hatch spacing of 200µm. Surface plots generated using Alicona infinite focus optical 3D measuring instrument.

Reducing the hatch spacing below the melt-track width promotes better bonding of parallel tracks, negating the occurrence of trenches and reducing pores within the structure of 3D parts, see Figure 41. The increasing overlap percentage additionally reduces the average surface roughness of parts. However, the higher laser scanning density alters the melt pool characteristics, promoting difficulties in comparing the surface roughness improvements with respect to the overlap percentage.

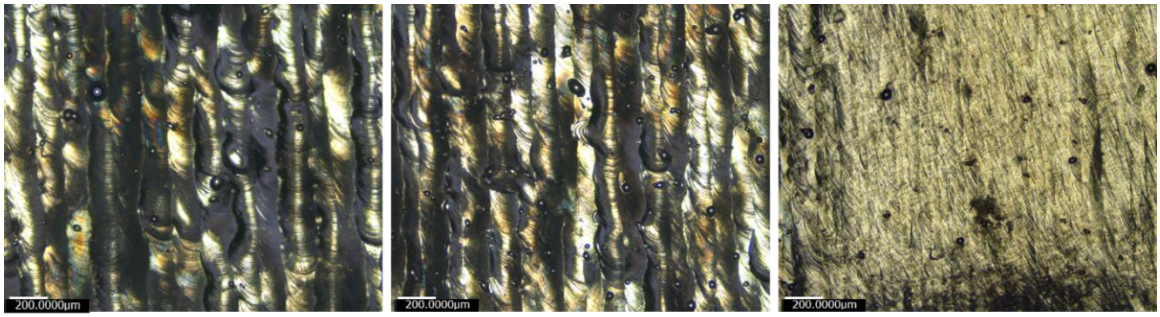

Figure 41 - Track and layer formation for varying hatch spacing and overlap percentages. Image taken using Alicona infinite focus optical 3D measuring instrument.

As trenches no longer feature with hatch spacings below the melted track width, it becomes possible to correlate and compare the average surface roughness (S_a) for the layers. Here, S_a is used because it measures roughness across the entire part surface, as opposed to incremental line profiles (R_a). S_a follows the same pattern as R_a, whereby it increases with respect to an increasing hatch spacing, Figure 42.

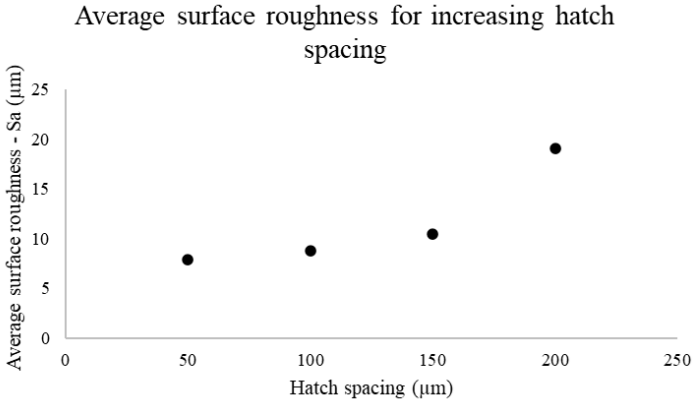

Figure 42 - Graph of average surface roughness for increasing hatch spacing.

The best surface finish as a result of differing hatch spacings was achieved at a hatch spacing of 50µm, Figure 43, equating to an average surface roughness and profile surface roughness of 7.89µm and 2.37µm respectively. This corresponds to a decrease of 58.9% and 82.2% when compared to a hatch spacing of 200µm. However, the printed layer height was also reduced from ~100µm to ~ 60µm due to the increased density of laser scans within the same area. This highlights the importance of hatch spacing for achieving good internal print resolution, imperative for producing functional, fully dense parts with the SLM process.

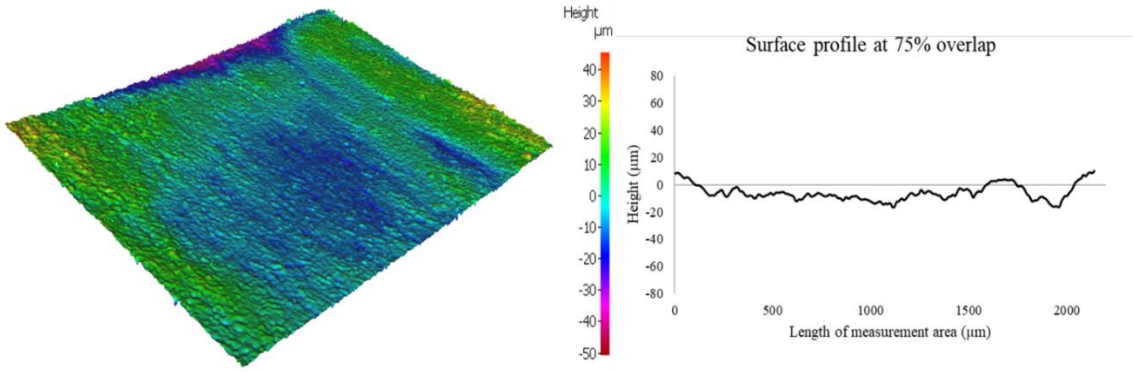

Figure 43 - Micrograph of layer printed with a hatch spacing of 50µm and respective surface profile, measured perpendicular to laser scanning direction. Surface plots generated using Alicona infinite focus optical 3D measuring instrument.

3.5.4 Elevated Edges in Printed Parts

The scanning procedure consists of a unidirectional scanning pattern, with the width between each scan equaling the hatch spacing, and a perimeter scan around the outer boundary of the printed layer. If an overlap is defined in the hatch spacing, further considerations must be made for the outer perimeter of printed parts, as they do not feature an overlap of laser scans on both sides of the edge. Further, during the outer boundary scan of the SLM process, there are powder particles on either side of the scan path, attracting more powder particles into the melt volume. This increases the size of the melt pool while limiting the amount of powder available for the next scan, therefore decreasing the size of the next track [85]. These phenomena result in elevated edges on parts manufactured by SLM, see Figure 44. These edges are detrimental to the process as they may come into contact with the powder spreader, causing vibrations which can result in waviness of the surface of the deposited powder and a poor surface finish of the manufactured part.

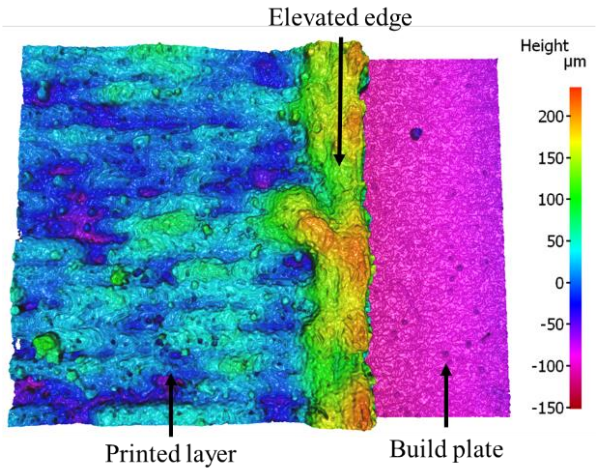

Figure 44 - Micrograph of printed layer illustrating elevated edge around periphery of printed layer. Image generated using Alicona infinite focus optical 3D measuring instrument.

Modification of the process parameters, such as the laser power and scan speed, on the outer boundary hatch can reduce the size of these edges but may weaken the connection between the outer boundary and the part's core. Laser re-melting procedures and high hatch spacing overlaps increase the edge height further if confined to the inner boundary [85]. This dictates the requirement of additional laser scans around the perimeter of printed parts or compensation within the part design around these. In regards to embedding optical fibres within SLM manufactured components, elevated edges inhibit the fitting of the fibre into the groove and can result in significant point like stress on the fibre at the egress and ingress points of the coupon. This was compensated for by increasing the width and depth of the groove within these regions [18]. In order to minimise the effects of raised edges, the outer boundary scan was repeated multiple times after the lasing process until the height of the layer edges matched that of the inner body hatch.

3.5.5 Layer Thickness

The lower limit for the layer thickness is constrained by the size of metallic powder particles used during the SLM process. In general, the lower the layer thickness, and therefore the more layers used during manufacture, the better the resolution and density of the finished part. Therefore, maintaining the layer thickness as low as practical is important when using the SLM process. The SS-316 powder used in this work contains particles in the range from 25 to 35µm diameter. Therefore, the minimum layer thickness achievable is set at 50µm.

3.5.6 Scanning Velocity

The laser scanning velocity was first investigated using single tracks, printed at varying velocities while maintaining the other build parameters the same. A lower scanning velocity promotes the formation of uniform single tracks, see Figure 45 and Figure 46. It is evident that high scanning speeds limit the heat input into the molten pool and result in part discontinuities including the initiation of balling. This parameter investigation will improve the geometrical accuracy and reduce porosity of printed parts.

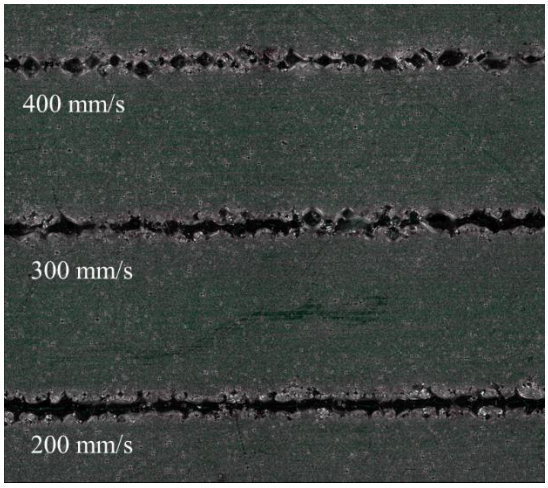

Figure 45 - Single track formation printed while varying laser scanning velocities between 400mm/s and 200mm/s. Image taken using Alicona infinite focus optical 3D measuring instrument.

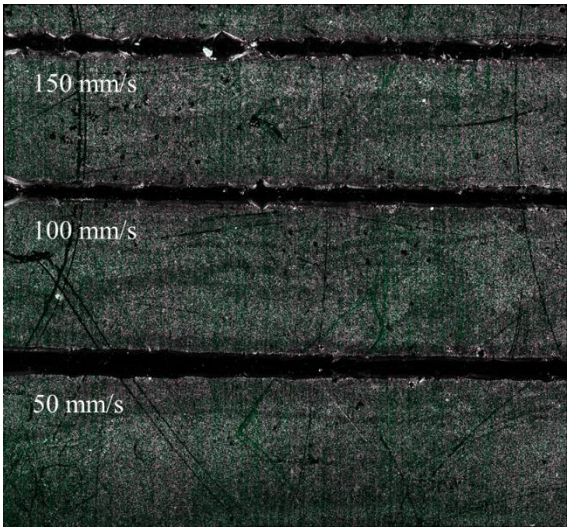

Figure 46 - Single track formation printed while varying laser scanning velocities between 150mm/s and 50mm/s. Image taken using Alicona infinite focus optical 3D measuring instrument.

As suitable build parameters depend on the balance of multiple variables, it can be difficult to definitively compare different scanning speeds, as their performance is reliant on other parameters and part features. For instance, for single track formation, lower scanning speeds promote better print quality and reduced surface defects with a constant power. However, this correlation does not cross over to parts containing a filled interior as more variables are involved in the build process, such as hatch spacing and layer overlap, that affect parameter relationships.

When building 3D parts, a slower scanning speed is defined for the outer perimeter of the part to ensure geometrical accuracy. For the hatching process, a high scanning speed is desired in order to limit excessive heat input on account of the overlap percentage defined into the hatch spacing. This induces temperature gradients within the printed part, creating thermal stresses that can detach layers from the sacrificial build plates.

When considering the maximum achievable laser power of 100W, maintaining the scanning velocity below 400mm/s was found to inhibit balling while still maintaining geometrical accuracy when building three dimensional parts. Other build parameters must be altered in order to maintain a suitable energy density for achieving fully dense parts, see Chapter 2 Section 7. For a consistent energy density, there is little difference between defining a faster or slower scan velocity, so long as the laser parameters are within the capabilities of the equipment.

3.5.7 Optimal Parameter Summary

The optimal parameters relate to the build parameters that achieve the best layer formation and surface finish of printed parts, with the custom ALM system. As the laser processing system is only capable of printing a single sample at once, the layer resolution must be balanced with print time for improved print practicality. Table 6 represents the optimal parameters and operational parameter boundaries of the manufactured laser processing system. Some parameters are displayed as ranges because their optimal value is dependent on the value of additional build parameters, see the definition of the laser energy density for SLM processes in Chapter 2 Section 7.

Parameter	**Value**
Laser power	$75 - 100$W
Scanning velocity	$200 - 400$mm/s
Layer thickness	$50 - 100\mu$m
Hatch spacing	$25 - 100\mu$m
Hatch orientation	Rotate by 45-90° at every new print layer

Pulse duration	200μs
Pulse modulation frequency	1kHz

Table 6 - Optimal parameter ranges for manufactured SLM system.

3.6 Layer Re-melting Process

One of the limitations of SLM parts without post-processing is the roughness of the outer surface. Using an additional laser re-melting process has the potential to reduce surface roughness by up to 80%, depending on the laser parameters used and the metallic material being polished [78].

Further, laser polishing can be incorporated into the SLM procedure as an additional in situ process, whereby a material layer is re-scanned by the laser without the further addition of powder material. When performed after each layer, this can improve the density of manufactured components, at the cost of an increase in build time, see Section 2.8.5 of the literature review. Applying the laser polishing process to the top layer only improves the shell density and the surface quality of the manufactured part [79]. This has important relevance to the embedding of optical fibres within SLM manufactured components as a decreased surface roughness allows for improved bonding of the fibre within the manufactured fibre groove [18].

Multiple laser re-melting scans can be incorporated to further improve the surface quality of manufactured parts. Incorporating a laser re-melting procedure into the fibre embedding process reduces the surface roughness of the groove compared to an as-built groove. The topmost layer of the part is re-scanned by the laser in a path parallel to the groove axis [18].

3.6.1 Process Parameters

Along with the energy density, equation (11), another important parameter in laser polishing is defined as the overlap index, whereby an overlap index of 100% corresponds to the laser polishing the same region as the previous scan and an overlap index of 0% corresponds to no overlap between passes of the laser. The overlap must be large enough to ensure that there are no gaps left un-processed but at the same time, must be small enough to mitigate excessive heat input that will further affect the material surface. Recommended values of between 15-30% are reported to be successful and the overlap index (%) can be calculated in terms of the beam diameter and step over distance (the distance a track overlaps another) by equation (12).

$$O = 100\frac{D - s_t}{D} \tag{12}$$

Where O is the overlap index in %, D is the diameter and s_t is the step over distance, both in mm. The overlap index will be taken into consideration when defining the hatch spacing of the laser polishing process to ensure the laser passes overlap by an amount within the aforementioned range.

The laser requirements for laser polishing procedures falls within the operational boundaries of manufactured laser processing system (10-100W power, 10-400mm/s scanning velocity, variable focus height). Therefore, a laser remelting procedure is simple to implement into the SLM embedding process.

A single layer part was manufactured using the SLM system, Figure 47, using a laser power of 100W, a scanning velocity of 400mm/s, layer height of 100µm, a hatch spacing of 100µm and a laser spot size of ~100 µm.

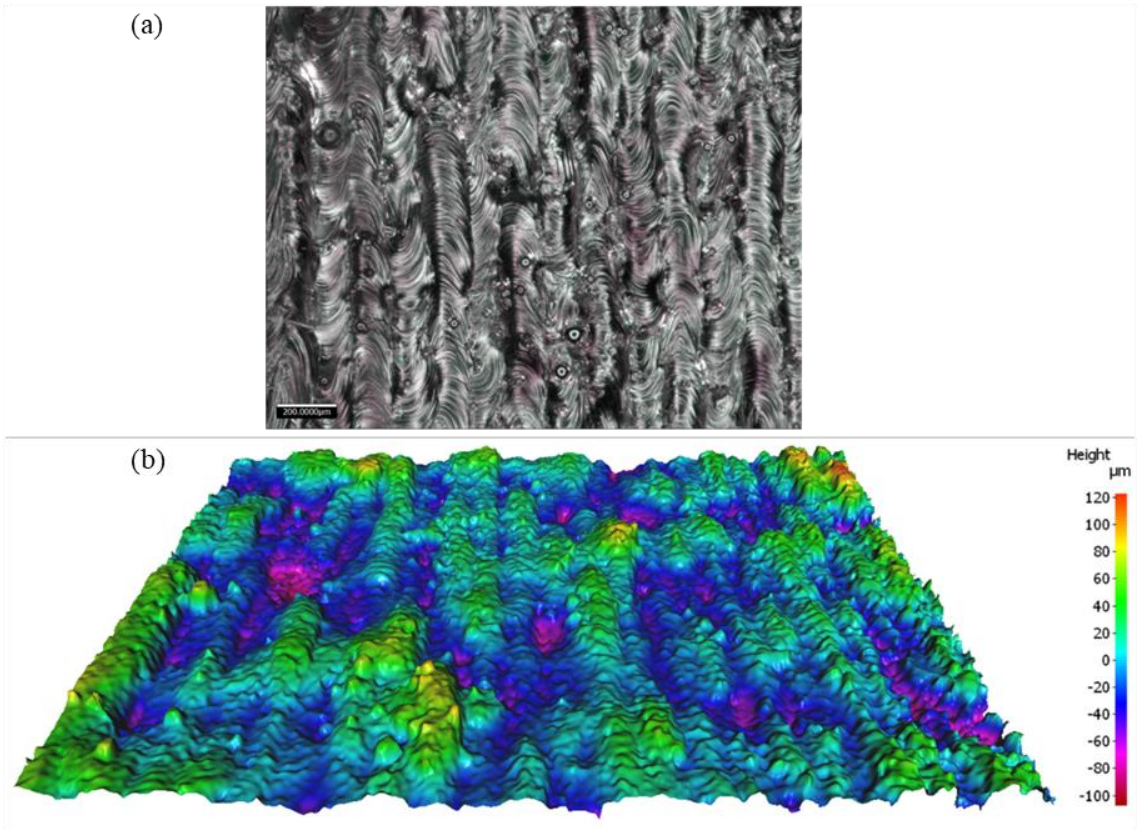

Figure 47 – Image (a) of melted layer printed using SLM system and micrograph (b) of surface profile. Image taken and surface plot generated using Alicona infinite focus optical 3D measuring instrument.

The average surface roughness of the profile (R_a) was found to be 7.4µm, measured perpendicular to the laser scanning axis, see Figure 48. The maximum peak to valley height (R_t) and mean peak to valley height (R_z) are measured as 78µm and 38µm respectively. These three values denote the parameters of interest when comparing the sample before and after the polishing procedure.

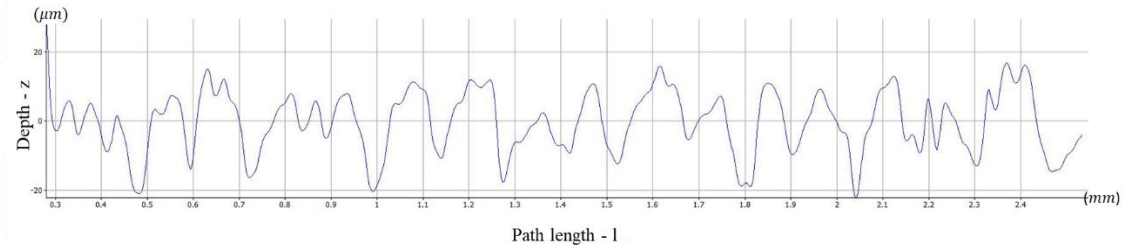

Figure 48 - R_a profile perpendicular to laser scanning axis of as built part. Surface profile generated using Alicona infinite focus optical 3D measuring instrument.

The sample was put through an intermediary laser polishing process to ascertain any improvements associated with the addition of this process step. Laser power was lowered to 60W, and a 20% overlap was defined by reducing the hatch spacing to 80µm. A raster scanning approach was used for the polishing procedure whereby the laser scanning axis is orientated by 45° every pass for four laser passes, (0°, 45°, 90°, 135°) [86].

Figure 49 illustrates an image of the polished sample and a micrograph of its surface roughness. The overall uniformity of the melted is layer is improved with a measured R_a of 2.5μm, a reduction of 65.6%. R_t was measured as 19.4µm and R_z was measured as 13.5µm, significant reductions when compared to the as built values. This is comparable to R_a values in literature for polished parts [86, 87], and is lower than typical as-built SLM layers [87], illustrating the importance of the additional polishing step in achieving low surface roughness.

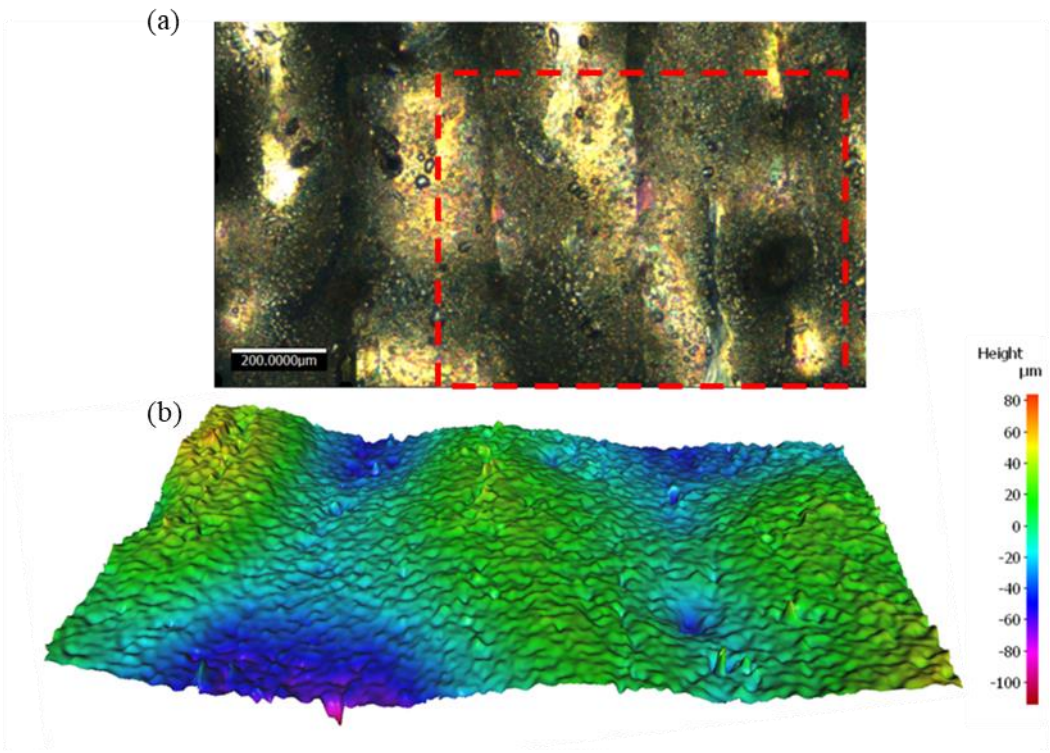

Figure 49 – Image (a) and micrograph (b) of sample (within red box) after undergoing polishing procedure. Image taken and surface plot generated using Alicona infinite focus optical 3D measuring instrument.

3.7 Chapter Discussion

The SLM was designed specifically for fibre embedding experiments, within the constraints of using the laser system and scan head available to the project. Due to the design and operational constraints of the system, it will never be able to compete with commercial of-the-shelf SLM systems in terms of raw performance but retains significant benefits for a research focused system with specific operational needs related to fibre embedding procedures. Being able to fully design and modify the system allowed for specific design requirements to be incorporated. These specifically related to build and laser parameter modifiability, system portability, full access to the build at any stage of the process, the ability to incorporate laser polishing and re-melting procedures, and ability to conduct fibre embedding investigations which include the capability of interrogating FBG sensors in-situ of the build process. Catering to all of these specifications is not currently possible using commercially available systems.

The performance of the SLM system for laser melting and re-melting procedures was demonstrated. While a certain degree of parameter balancing can take place to ensure consistent energy densities, many existing investigations define a requirement of the laser power far beyond the capabilities of the system (>100W) with many investigations approaching 200W laser power and 800mm/s scanning velocity [88, 89]. This suggests the main constraint on the system performance is the available equipment, as opposed to the mechanical and optical design.

The suitability of the system for printing layers of SS-316 is shown, justifying the extensive system design and subsequent modifications during the project work. Furthermore, the ability to use the same system for laser polishing procedures is proven with a significant reduction in surface roughness demonstrated, which goes some way to compensate for the hardware limitations for achieving dense parts with low surface roughness. In addition to this, the ability to conduct both processes in parallel without interruption has significant benefits for fibre embedding procedures.

The occurrence of balling effects on the printed surface was mitigated in line with strategies defined in literature, [84]. However, the main limitation method is to increase the laser power, which was constrained to a maximum mean power of 100W. Therefore, their occurrence could not be negated completely without post-processing re-melting procedures. More success was achieved for reducing trenches between scanning layers and the reduction of elevated edges around the periphery of printed parts, as these issues can be designed out with build set up and parameters in addition to lasing procedures within the system's capabilities [85]. The energy density (ED) range of system where suitable layers are formed is 25-50 J/mm^3. This is lower than energy densities reported in literature for laser melting SS-316(~80-300 J/mm^3) [90], which can be attributed to the availability of higher power laser systems (>100W). The higher energy densities achievable in commercial systems results in a higher relative density within the material layer than achievable by the system [90, 91].

In all, this chapter sets the foundation for later experiments into fibre embedding and demonstrates the applicability of the custom laser processing system for printing SS-316 coupons.

3.8 Chapter Review & Conclusions

The chapter provides an overview of the custom SLM and laser processing system, post-manufacture modifications and operational performance with respect to laser melting and processing high-melting point metals, such as SS-316.

The primary function of the laser processing system is to perform selective laser melting procedures in order to embed metallised optical sensors within additive manufactured SS-316 parts. The system was therefore designed to allow modification to the build parameters of each build layers, which is important for fibre embedding as different layers may require different build parameters.

The system itself was constrained by certain design parameters, such as the requirement of being portable, allowing for fibre egress and ingress, while maintaining an inert atmosphere, and the use of available laser and scan head arrangement, which dictated the upper power limitation of its process parameters. However, it was designed in such a way that if alternative laser systems became available in the future, they could be easily integrated into the SLM set up.

Despite the operational limitations, the flexibility of the system to deliver customized laser parameters for each processing layer is demonstrated by the incorporation of laser polishing procedures. Further, the parameter calibration analysis allowed the system to be optimised, within its operational boundaries, for achieving printed layers with low porosity and surface roughness. Both of which are important parameters for successful embedding of optical sensors. The definition of the optimal build parameters was conducted within the operational limitations of the system. Therefore, further improvements may require the use of a higher power laser system (around 200W), double that which was available to the project. Further to this, if portability, size constraints and spatial limitations were not factors, performance could be further improved. However, the system is more than applicable for fibre embedding investigations and the ability to print parts using SS-316 powder was demonstrated.

Potential detrimental effects and features that may occur within the SLM process such as balling, trenches and elevated edges, were illustrated along with the necessary steps and parameter modifications required to minimise their occurrence. The proposed optimal parameters were calibrated with respect to the mechanical and optical set up of the custom SLM system to allow for fibre embedding investigations.

Chapter 4 - Fibre Metallisation

This chapter details the deposition of a protective nickel (Ni) jacket onto the FBG sensor which is required to protect the fibre during the embedding process, and to provide adhesion between the fibre and the sample. This is done via a two staged process which used RF sputter deposition to deposit an initial thin film (5-10μm) of chromium onto stripped fibre lengths, and then a custom Ni electroplating system, capable of deposition of uniform coatings onto the ~130μm diameter chrome-coated fibres.

4.1 Introduction - Fibre Metallisation for Protection During Embedding

Direct embedding of optical sensors is widely documented for polymer materials, [1, 4, 16]. The temperature range the fibre is exposed to during the build process is typically $< 200℃$, which is much lower than the softening point for fused silica glass (1700°C) which would damage the fibre [92]. However, any powder-based manufacturing technique using high melting point metals requires a significant amount of heat input in order to fully melt the powder particles. For example, SS- 316, melts around 1375-1400°C [52, 82], which exceeds the glass transition temperature (the temperature a material begins transition from a hard, brittle material into a ductile material) of fused silica [92], which would be in detriment to the light-guiding properties and survivability of an optical fibre.

A further complication for direct embedding of fused silica into a metal part arises from the mismatch in thermal expansion coefficients for fused silica glass and SS-316. The mean coefficient of thermal expansion between 10-1000°C for fused silica glass is $4.7 \times 10^{-7}\ K^{-1}$ [11], this is significantly lower than the mean coefficient of thermal expansion for SS-316 within the same temperature range, $19.4 \times 10^{-6} K^{-1}$ [82]. This mismatch will create difficulties in embedding optical fibres within high-melting point metals such as SS-316 as the fibre and bulk material will expand and contract at different rates depending on the temperature, potentially creating bonding issues in applications involving extreme temperatures and/or large thermal gradients.

Encapsulating the fibre in a protective metallic jacket, see Figure 50, shields it from the heat required by the embedding process. If the jacket material is suitably matched to the embedding material, it also promotes intermixing of the metallic jacket and the surrounding material, effectively bonding the fibre in place. In the instance of embedding nickel coated fibres inside SS-316 parts, the nickel (14%) component of SS-316 promotes intermixing of the nickel jacket with the bulk SS-316 material [50]. Maintaining a coating thickness of $\geq 350\mu m$ is shown to provide suitable fibre protection during embedding, while still ensuring bonding between the fused silica fibre and metallic jacket [12, 18, 75].

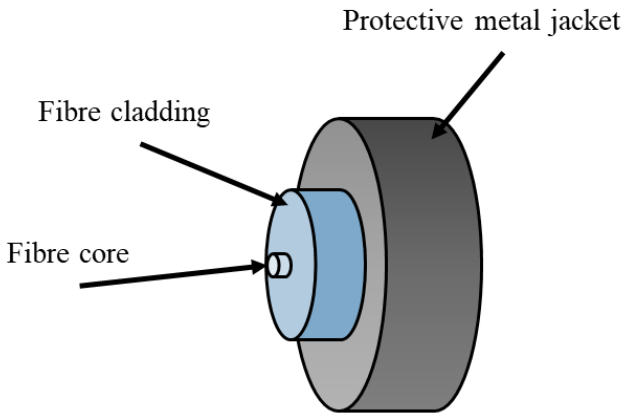

Figure 50 - Illustration of a metallised fibre cross section.

In this thesis, fibre metallisation is achieved by a combination of RF-sputter deposition of a keying Cr layer, and Ni electroplating to build up the required thickness. RF sputter deposition is necessary to deposit a thin conductive layer (≈ 5-10µm) onto a fused silica fibre. This layer is required for providing a conductive, metallic surface for subsequent electroplating to take place. After the RF sputter deposition process, the metal-coated fibre will be electroplated with a thick layer of nickel (≈350-500µm) to provide protection during the embedding process.

Prior to metallisation, the fibre is prepared by mechanically stripping the polymer cladding and cleaning with isopropanol (IPA) to remove any excess material and ensure a uniform, smooth surface for deposition. Mechanical stripping is known to cause micro-cracks on the fibre surface, creating potential failure points as the cracks propagate. This was seen to be an issue during fibre preparation with fibre breakages, but enough successful samples were created using this methodology to allow the embedding work to progress. However, potential future work within this chapter would be to incorporate chemical stripping into the fibre preparation process and ascertain its benefits in terms of repeatability and fibre survivability in comparison to mechanical stripping.

4.2 Radio Frequency Sputter Deposition of Chromium

During the RF sputter deposition process, metallic materials are coated onto nonmetallic surfaces, such as silicon, fused silica glass and ceramic, which is unobtainable using electroplating alone. The primary purpose of this layer is to adhere to the fused silica fibre and provide a conductive surface for the subsequent electroplating process. When compared to other coating materials, Cr provided the best balance for ease of deposition, deposition rate and suitable conductivity of the deposition for the electroplating process [12].

4.2.1 RF Sputter Deposition Equipment

Sputter deposition is a physical vapor deposition technique in which an induced plasma of Argon ions bombards a material source. As a result, the source material is ejected and forms a thin film on any surface on which it is incident. In this case, the deposition substrate is positioned to intercept the ejected material [93].

The sputtered particles are not subjected to gas phase collisions during transit between the source and the sputtering target [94]. The sputtering process can be powered in a variety of ways, mainly using direct current voltage for conductive materials, and radio frequency excitation (RF) which opens up the possibility of depositing non-conductive materials [93]. A schematic illustration of the RF sputter deposition system used for the project work is highlighted in Figure 51, the optimal process parameters of which are defined in Chapter 4, section 2.3.

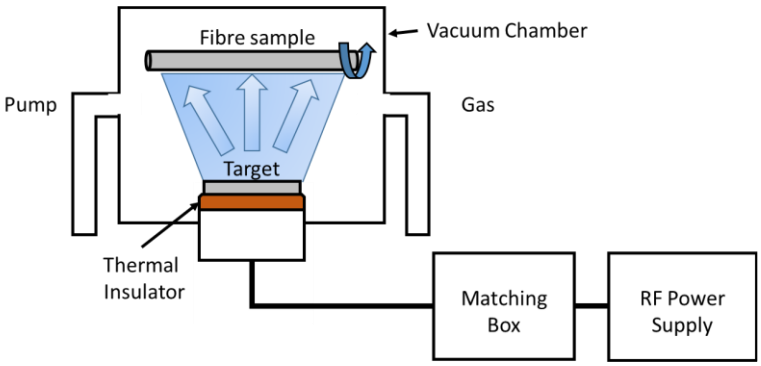

Figure 51 - Schematic Illustration of RF Sputter Deposition System.

For the subsequent electroplating process to be successful, the chromium coatings must be uniform around the circumference of the fibre. Therefore, a fibre rotator was manufactured to rotate the fibre during the sputter deposition process. A fused silica tube is used to mount the fibre onto a DC geared motor, positioned 15cm above the sputtering target. The rotational speed is set to 7rpm and all surfaces that are not required to be coated are shielded using aluminium foil. A schematic representation of fibre rotation sub-system is provided in Figure 52. Prior to metallisation, the optical fibres are mechanically stripped of their polymer coating and cleaned using isopropanol to ensure a uniform surface and remove any excess residue.

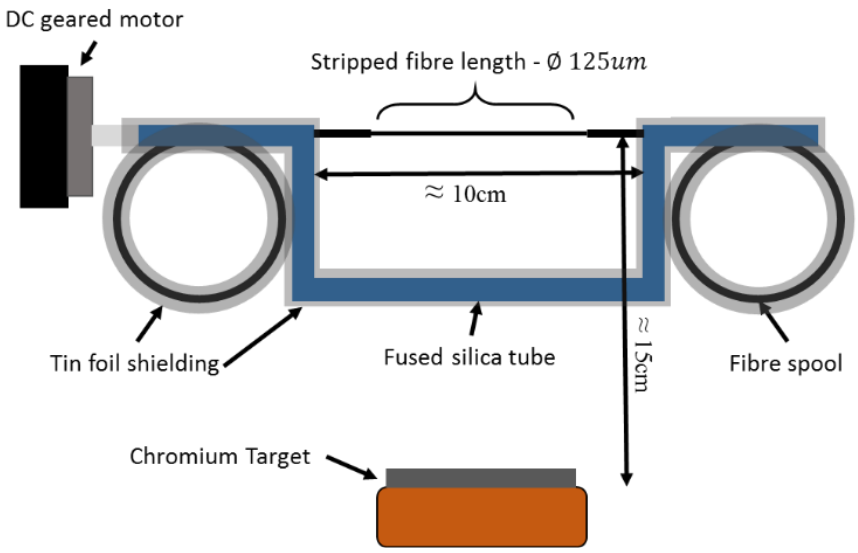

Figure 52 - Schematic illustration of fibre rotator system located inside RF sputter deposition chamber.

4.2.2 Estimating Thickness of Chromium Coatings Using Their Electrical Resistance

The purpose of depositing a thin layer of chromium onto the optical fibre is to provide a conductive keying layer for the subsequent electroplating process. The electroplating system is powered by a power supply with mA precision and voltages up to 30V. Therefore, the resistance of the coated fibre must be within a range suitable for this equipment, estimated using Ohm's law to be in the order of a few hundred ohms using the expected current range ($\leq 500mA$).

The resistance of the deposited layer can be estimated from the resistivity, ρ_R, the fibre length, L, cross-sectional area, $A_{cross-sec}$, of the coating, via equation (13).

$$R = \frac{\rho_R L}{A_{cross-sec}} \tag{13}$$

The cross sectional area of the coating is calculated by equation (14), which will increase as the outside diameter of the coating increases, resulting in a decrease in electrical resistance. From equations (13) and (14), the resistance of chromium coatings as a function of coating thickness is illustrated in Figure 53 with the suitable resistance range for the electroplating process highlighted on the graph. The threshold of 700Ω is defined as the maximum achievable by the power supply operating with currents in the mA regime.

$$A_{cross-sec} = \pi \frac{D_{coating}^2 - D_{fibre}^2}{4} \tag{14}$$

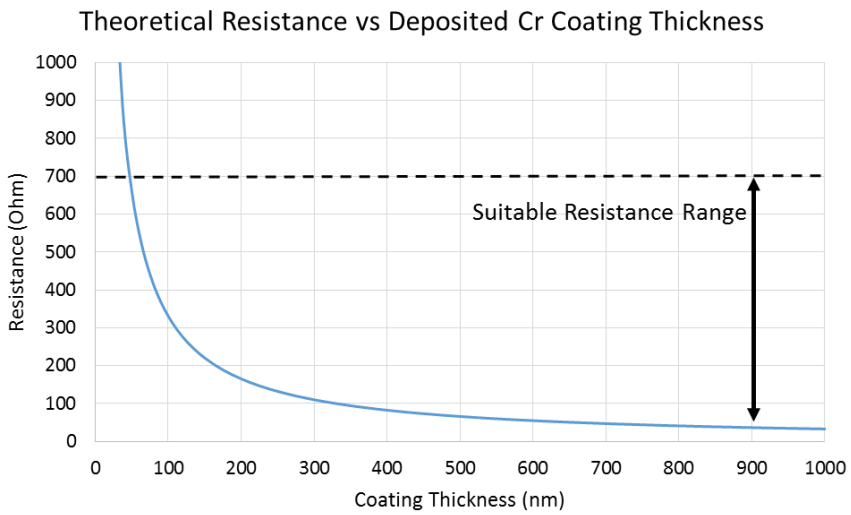

Figure 53 - Theoretical resistance as a function of coating thickness for Chromium coatings deposited by RF sputter deposition with a fibre length of 100mm. The resistivity of Chromium is taken as $125x10^{-9}$Ohm-meters at 20°C.

4.2.3 Process Parameter Characterisation

The RF sputter deposition system was characterised using fused silica microscope slides positioned 15cm above the sputter target. In order to determine the thickness, a diamond scribe was used to etch through the Cr coating and a profilometer was used to determine the difference in height between the Cr layer and the fused silica slides. The process parameters of interest are the deposition time, RF power and argon pressure. For constant power and pressure conditions, the thickness of coatings increases linearly with respect to deposition time, see Figure 54. Increasing the RF power additionally increases the coating thickness, see Figure 55(b), while increasing the argon pressure is seen to decrease the thickness of the coatings, see Figure 55(a). The relationships between the various process parameters and deposition thickness are consistent with previous literature studies [95, 96].

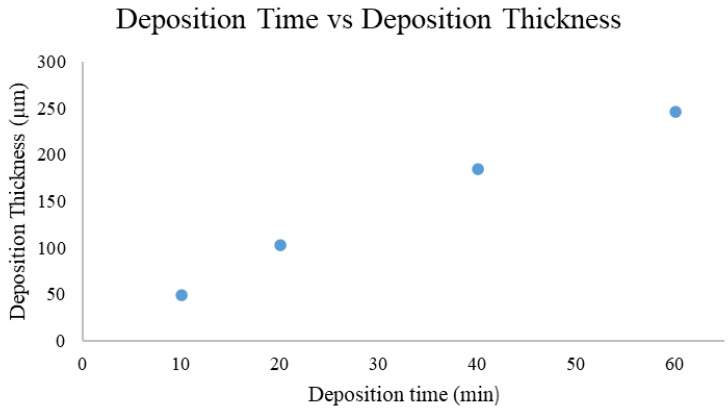

Figure 54 - Deposition thickness vs deposition time for constant power conditions.

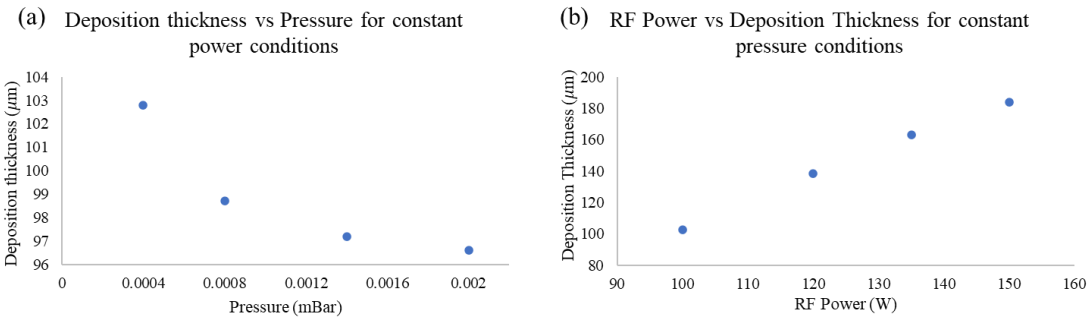

Figure 55- (a) Deposition time vs pressure. (b) RF power vs thickness.

Gas pressure in the region of 4×10^{-4}mBar is the lowest pressure achievable from the system while still allowing the plasma to strike to initiate the deposition process. In this case, vacuum pressure is measured in Bar as opposed to Pa. The magnetron sputter head is rated at 150W, constraining the maximum usable RF power to this value. Therefore, with the available equipment, deposition time remains the most suitable process parameter to vary to achieve the desired coating thickness. These deposition rates relate to flat substrates, therefore are expected to reduce when depositing onto fibre lengths with an outer diameter of 125µm.

Using the above method, coatings were deposited onto optical fibres that provided sufficient conductivity for a successful electroplating process, see Figure 56. The deposition parameters used to achieve this were 150W RF power, 4×10^{-4}mBar pressure and a deposition time of ≥30 minutes. Raising the deposition time above this value is beneficial for achieving thicker coatings that promote better performance within the electroplating process. However, extended operation of the coating chamber in this way can induce significant heat into the equipment and must be done in staggered increments, with breaks that allow the system to sufficiently cool.

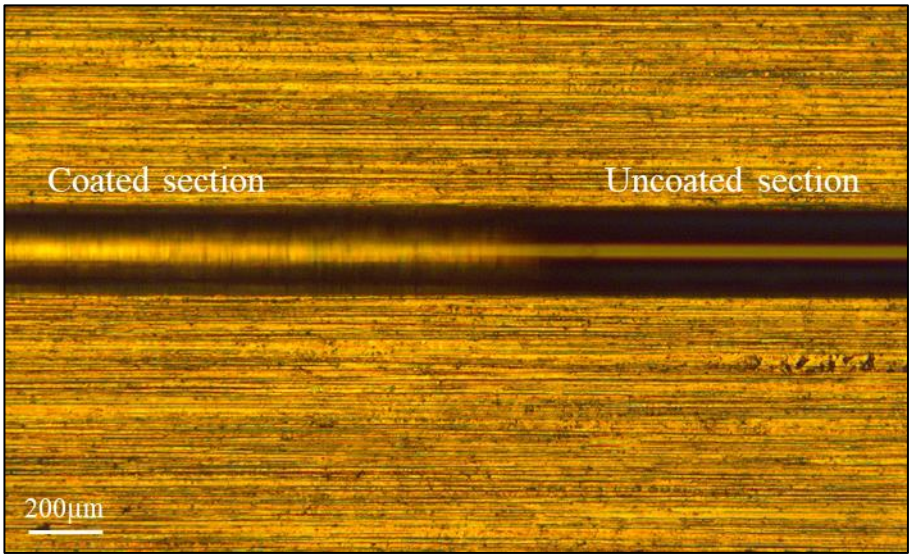

Figure 56 - Picture of chrome coated optical fibre, illustrating coated and uncoated regions. Image taken using a Leica 3D optical surface metrology system.

4.2.4 RF Sputter Deposition of Nickel

Deposition of nickel onto optical fibres as the keying layer would be beneficial as it would potentially negate the need for a secondary electroplating metallisation process if deposition time was not a constraint. The investigation used the same sputter deposition system RF source and vacuum chamber. Nickel is a magnetic material, and as a result, a higher power magnet was required in the magnetron sputter head in order to compensate for the magnetic interference caused [97].

Various deposition parameter combinations were investigated in order to promote nickel deposition, Table 7. The parameters investigated were the RF power, the substrate distance from the target, and processing pressure, while deposition time was maintained constant at 30 mins. Despite these investigations, nickel depositions were not achieved using the sputtering deposition system.

	processing pressure (mBar)			
RF power (W)	1×10^{-4}	4×10^{-4}	1×10^{-3}	
25	15	15	15	**Sample distance**
50	15	15	15	
75	15	15	15	
100	10, 15, 20	10,15,20	10,15,20	
125	15		15	
150	15		15	

Table 7 - Parameter combinations investigated for RF sputter deposition of Ni.

Deposition time was limited to 30 minutes, as extended deposition times promote heat build-up within the internal vacuum chamber and within the magnetron sputter head assembly at severe detriment to the system. Staggered depositions totaling three hours at 150W RF power and a processing pressure of approximately 2×10^{-4}mBar, no deposit was visible on the glass substrates. By comparison, for the same deposition parameters, chromium deposition upwards of 35µm were achieved.

In these trials, it was observed that the system was unsuitable for Ni deposition. This is believed to be due to the lower magnetic field above the target, inhibiting release of the plasma from the target's surface [97]. Not only does this prevent deposition, but induces excessive heat buildup within the system, at severe detriment to the sputter deposition vacuum chamber and magnetron sputter head assemblies.

As a result of this investigation, RF deposition of Ni was not taken further within this project thesis. However, if Ni as a keying layer is desired, the following discussion highlights potential routed to achieve this.

A reduction of the target thickness would promote successful deposition of nickel due to reducing the effect of the magnetic interference. However, doing so within a magnetron sputter head specifically designed for 6.35mm targets would promote further difficulties and require modifications to sputtering head assembly. Y. Mikama et al., achieved deposition of nickel using a 1.5mm target, using an unbalanced magnetron that incorporated an external magnet assembly to the magnetic circuitry to confine the efficient plasma to the sputtering target surface [97].

Sputtering targets can be made using a different target material and locating thin nickel shims on its surface during the deposition process. This would promote efficient plasma, while also limiting the field line distortion above the sputtering target. However, this would require extensive investigation, and as Cr promotes suitable results for depositing a conductive layer for the subsequent electroplating process, deemed unnecessary for the thesis goals. In addition, as Cr coatings were reliably produced within the system's parameter ranges, the required modifications to the magnetron sputter head assembly for depositing Ni were not considered further.

4.3 Electroplating Nickel

The use of a two-stage metallisation process incorporating electroplating to deposit Ni onto FBGs and other optical sensors is not new, [49, 98, 99], and is shown to provide sufficient protection for the sensor for embedding procedures [98].

Li et al., 2006, developed a process using electroless plating to deposit a thin conductive layer of copper of nickel onto the FBG before a thicker layer of Ni is deposited. The coated FBG was then embedded into 42CrMo steel by brazing [98]. This method was shown to provide sufficient protection for the FBG during the embedding process. Furthermore, the temperature sensitivity of the metallised gratings is shown to increase as the thickness of the Ni deposition increases due to the applied loading on the fibre [49].

Electroplating is a deposition process whereby metal ions migrate via an electrolyte solution from a positively charged anode(s) composed of the plating material to a negatively charged cathode, which is the material to be plated [100].

For the electroplating process to be successful, it is necessary to ensure that the current density remains within the specified values unique to the chemical composition of the electrolyte solution. In this thesis, where it is required to coat a thin cylindrical fibre, then as the diameter increases and hence the surface area of the coated fibre increases then the current density will decrease. However, by choosing a suitable starting current then adjustments to the supply parameters will not be required if the current density remains within the recommended range (~2-15 A/dm^2) [12, 100].

4.3.1 Estimating the Mass of Nickel Deposition by Application of Faraday's Laws of Electrolysis.

The mass of deposited nickel at the cathode and dissolved at the anode can be determined by application of Faraday's law of electrolysis to nickel plating. The mass of nickel in grams is directly proportional to the current and time and is expressed in equation (15) [101].

$$m = \left(\frac{M}{n_e F}\right) aIt = 1.095aIt \tag{15}$$

Where, $\frac{M}{nF}$ = 1.095 is the proportionality constant in grams per ampere hour, calculated by dividing the atomic weight of nickel (M) by the product of the number of electrons (n_e) and Faraday's constant, $9.65 \times 10^4 \mathrm{C/mol}$ (F). I and t denote the current and time respectively and the variable a corresponds to the cathode current efficiency (typically 90-97%) which relates to the amount of electric current consumed by hydrogen ions(3-10%), which form bubbles of gaseous hydrogen on the cathode surface [101].

4.3.2 Average Deposition Thickness Estimation

An expression relating to the average thickness of a nickel coating can be calculated by dividing equation(15) by the product of the density of nickel ($\rho = 8.907 \mathrm{gcm}^{-3}$) and the surface area to be plated (A) in dm^2. Equation (16) defines the average coating thickness (s) in µm, dependent on the current density (I/A) and plating time (t) [101]. This relationship was used to determine estimations of the required current and time to achieve 140 µm average coating thickness for a constant coating area. This provides a starting point from which to initiate the experimental calibration of the system.

$$s = \frac{100m}{\rho A} = \frac{12.294aIt}{A} \tag{16}$$

Figure 57 illustrates plating time against current for achieivng 140 μm thick coatings around a stripped optical fibre with an outside diameter of 125 µm, assuming a cathode current efficiency of 95.5%. The results show less deposition time is required at higher currents, but lower current densities (highlighted in green on Figure 57) are more suitable for achieving a stable plating process and uniform coatings [100].

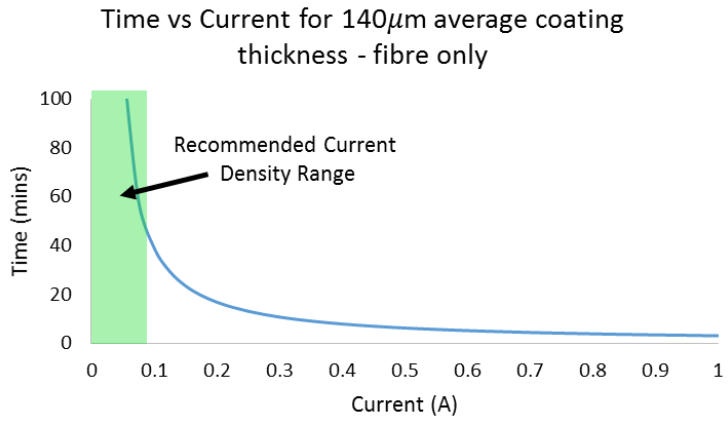

Figure 57 - Graph of time against current for an average coating thickness of 140µm, based on equation 16 and assuming a cathode current efficiency of 95.5% and 10cm long stripped optical fibre.

4.3.3 Applicable Current Range

Recommended current densities range from 2-15 A/dm² for nickel plating using Watts nickel plating solutions [100]. Keeping the current density within the correct operating range is important in order to achieving uniform depositions with suitable integrity.

Table 8 illustrates the time required to achieve depositions at various current densities. From Table 8, the range of currents that lie within the recommended range are 0.01A-0.075A based on coating a stripped length of fibre (~80mm) with an initial outside diameter of 125µm.

Current (A)	0.01	0.025	0.05	0.075	0.1	0.125	0.15
Current density (A/dm^2)	2	6	12	18	24	31	37
Thickness (µm)	Time to obtain deposit at various current densities (minutes)						
25	52	21	10	7	5	4	3
50	104	42	21	14	10	8	7
75	157	63	31	21	16	13	10
100	209	83	42	28	21	17	14
125	261	104	52	35	26	21	17
150	313	125	63	42	31	25	21
175	365	146	73	49	37	29	24
200	417	167	83	56	42	33	28
225	470	188	94	63	47	38	31
250	522	209	104	70	52	42	35
275	574	230	115	77	57	46	38
300	626	250	125	83	63	50	42

Table 8- Time to deposit various coating thicknesses at varying current densities, based on equations (15) and ((16) .

4.4 Nickel Electroplating System

An electroplating system is designed for the deposition of nickel onto Cr coated fibres, is illustrated schematically in Figure 58. Multiple Ni anodes, connected to a variable current DC power source, surround the metal coated fibre cathode during the plating process to aid uniform deposition. A magnetic stirring hotplate allows for agitation and heating of the electrolyte during the plating process, necessary to aid in the removal of hydrogen bubbles formed at the cathode [102].

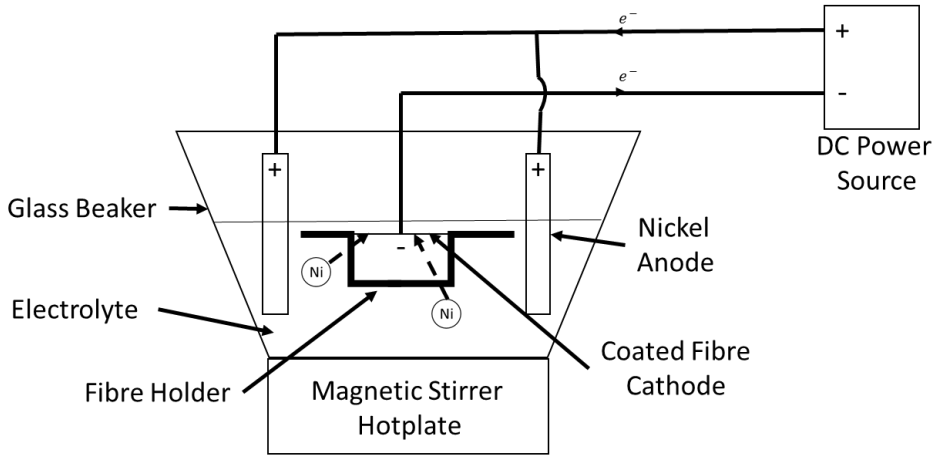

Figure 58 - Schematic diagram of electroplating set up, where *e* denotes current flow.

4.4.1 Design Specifications

The electrolyte is based on a Watts plating bath solution, an aqueous electrolyte for nickel electroplating invented by Oliver Patterson Watts [100], which contains the chemical composition and operating parameters highlighted in Table 9 [100]. This form of plating solution produces functional nickel coatings widely used in industry for engineering applications. It operates at a low voltage compared to other plating solutions and provides a high rate of deposition, [100, 102].

As is common in the Watts bath chemical composition, a small concentration of chloride is beneficial for achieving low stress levels and also helps to improve the performance of the anode. Boric acid acts as a buffer and aids in pH control of the solution as some hydrogen ions are discharged, altering the pH of the solution as hydrogen gas is liberated [100].

The tank size is constrained by the dimensions of the fibre holder (23cm) and surrounding anodes. Ideally, a smaller tank is better suited as less electrolyte solution is required to submerge the required components. There must also be enough room to maneuver components inside the tank into the desired position. Therefore, in order to cater for these constraints, a cubic tank with a minimum length of 25cm was used to house the electrolyte solution.

Nickel Sulphate ($NiSO_4 6H_2O$)	240-300 $\frac{g}{L}$
Nickel Chloride ($NiCl_2 6H_2O$)	30-90 $\frac{g}{L}$
Boric Acid (H_3BO_3)	30-45 $\frac{g}{L}$
Temperature	40-60℃

pH	3.5-4.5
Cathode Current Density	2-7 A/dm^{-2}
Deposition Rate	25-85 $\mu m/h$

Table 9- Typical chemical composition and operating parameters for Watts nickel plating solution, taken from [100].

4.4.2 System Design

The above design specifications were taken into account for the manufacture of the electroplating system, see Figure 59. Two 10×10cm nickel plates act as the anodes, submerged either side of the fibre holder, as close as is feasible while allowing fluid flow. The anodes are connected to the negative output of a low voltage DC power supply, capable of current control with the milliamp resolution up to a maximum current of 2A (subject to sufficient drive voltage limited at 30V).

Submersible water tank heaters, 100W HITOP adjustable aquarium heaters, were added to the system to reduce the amount of heating required by the hotplate, as this was initially observed to introduce large temperature gradients across the bottom surface of the tank, increasing its susceptibility to failure. Conductive copper tape is used to bridge the electrical connection between the optical fibre and the negative output of the DC power supply, while Polytetrafluoroethylene (PTFE) tape is used to shield any surfaces not to be plated, see Figure 60.

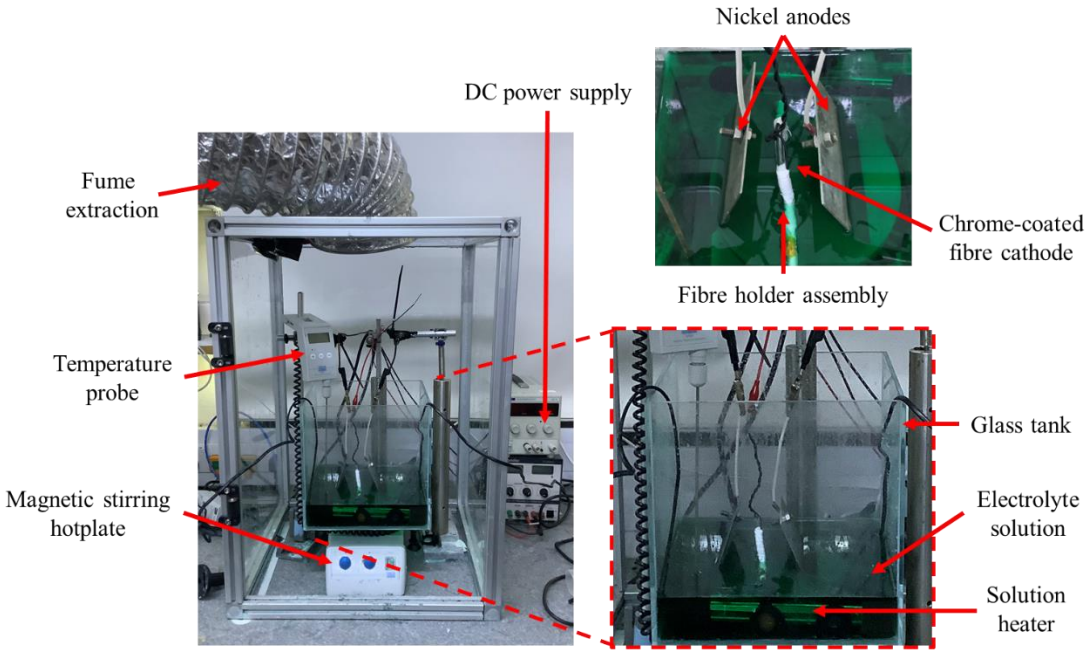

Figure 59 - Manufactured Electroplating system. Close up image of the plating tank is shown inside the red dashed square. A close up image of the submerged fibre holder assembly containing the chrome-coated FBG (cathode) and nickel plates (anodes) is illustrated in the upper right section of the figure.

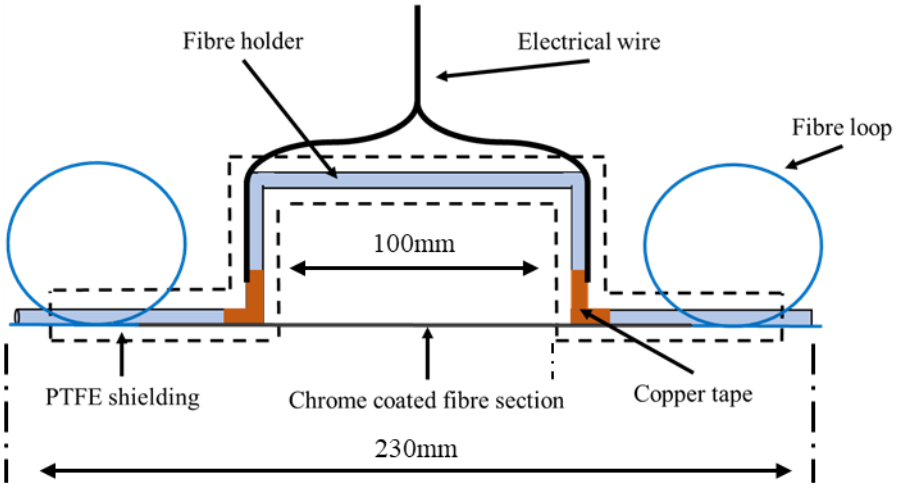

Figure 60 - Schematic illustration of the fibre holder assembly showing how copper tape is used to bridge electrical connection between power supply and fibre. Dashed line represents PTFE shielding.

Sandwiching the Cr coated fibre between two segments of copper tape achieved the best electrical connection. However, this induced difficulties in removing the plated fibre from the fibre holder/ prompting the method for resting the Cr coated fibre against a single layer and shielding it in PTFE tape, as illustrated in Figure 60. The addition of small amounts of petroleum jelly around these locations prevented deposition over the electrical connection points that would otherwise bond the fibre onto the mounting assembly. Agitation is induced into the solution via a magnetic stirrer driven by the hotplate below the tank. This is important to reduce hydrogen bubble formation at the cathode (fibre) surface. These bubbles inhibit deposition where they attach to the cathode, creating pits on the plated surface, see Figure 61. The magnetic stirrer is set to a low rotational speed in order to maintain slight agitation of the electrolyte. If the stirrer speed is too high, it creates a vortex flow around the cathode-anode assembly, situated directly above the magnetic stirrer [100]. This could inhibit deposition potentially dislodge or misalign the submerged assembly anode/cathode assembly.

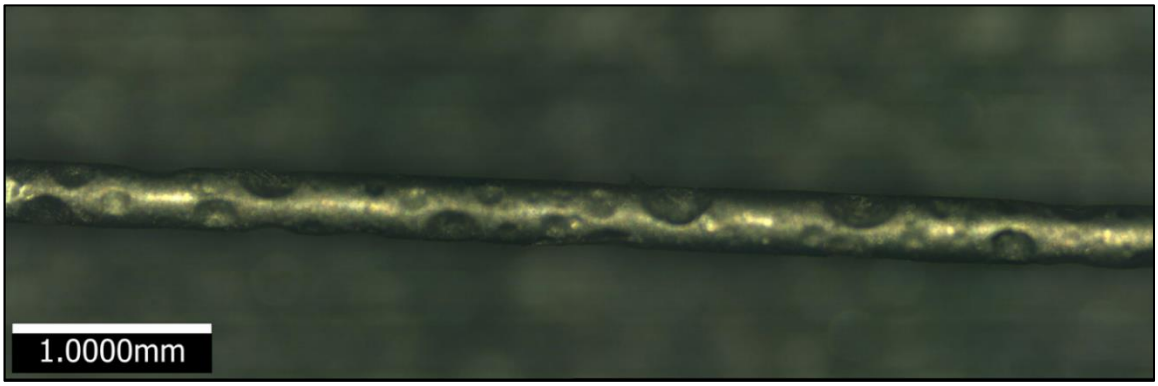

Figure 61 - Figure illustrating pits on Ni plated surface due to hydrogen bubble formation. Image taken using a Leica 3D optical surface metrology system.

The average deposition time of the system for depositing onto Cr coated fibres was 16.7µm/hr, see section 4.4.3.2. Therefore, a second plating tank was incorporated into the electroplating system, see Figure 62, to increase sample throughput.

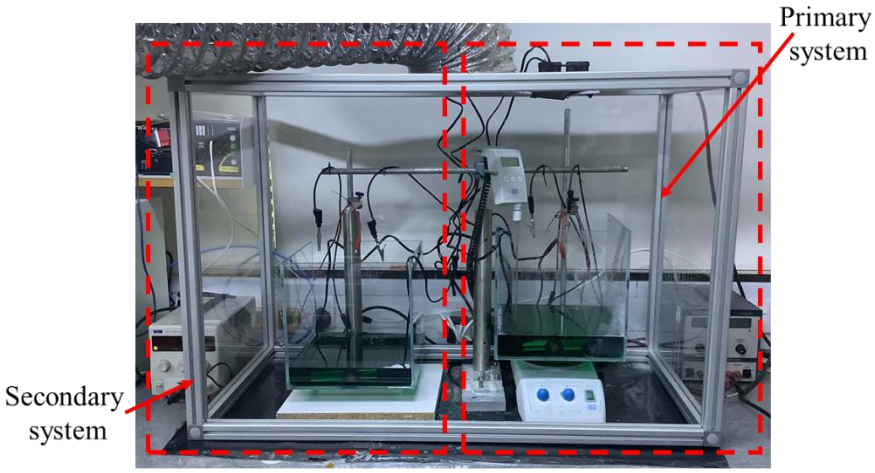

Figure 62 - Modified electroplating system incorporating second tank and power supply for increased yield.

4.4.3 Electroplating Parameter Optimisation

The optimal parameters for electroplating nickel onto chrome coated optical fibres are specific to the electroplating system, electrolyte and surface area being plated. The predication from Faraday's laws of Electrolysis provides a starting point for system optimisation and allows a more focused study of the parameter space.

During operation, it became evident that the process parameters required to achieve uniform coatings need to be balanced against practical deposition time in order to avoid excessive plating times while maintaining suitable coating quality. While the system can operate unsupervised, it requires intermittent inspection to ensure there is the appropriate amount of electrolyte and there are no component or process failures that could pose health and safety risks.

4.4.3.1 Process Parameters for Achieving Uniform Coatings on Fibre Capillaries

Fibre capillaries were used for initial calibration as they provide a larger surface area to be plated than optical fibres. This allows for the system to be checked with cylindrical bodies that can be visually inspected with ease, allowing for initial process characterisation before reducing the size scales to Cr coated stripped optical fibres. Metallising fibre capillaries to allow strain isolated fibres to be embedded. This offers a potential mechanism to measure temperature without the influence of strain, and thereby offer a potential mechanism for temperature compensation of strain sensors embedded in the structure that would be subject to the combined effects of strain and temperature.

A 750μm borosilicate capillary was metallised with the coating thicknesses determined in increments of one hour in order to correlate a deposition rate. The voltage was set at 7V throughout with the current chosen to maintain the current density between 2 - 7 $\frac{\mathrm{A}}{\mathrm{dm}^2}$, as required by the Watts electrolyte composition specifications, see Table 9. The maximum surface area being plated (based on coated fibre diameter of 400µm) is $12 \times 10^{-3} \mathrm{dm}^2$, a factor of three larger than the minimum (130µm). Therefore, so long as the current is maintained below 8mA, changing of the current is required to maintain the current density within this range ($\leq 7 \frac{\mathrm{A}}{\mathrm{dm}^2}$).

This experiment was repeated three times to determine the deposition rate for Ni coating of capillaries with a Cr keying layer, the results of which are highlighted in Figure 63. Figure 64 illustrates the capillary before and after metallisation for a deposition thickness of 73.5µm correlating to a deposition rate of 24.5µm/hr, comparable to the lower limits of the typical deposition rate of Watts nickel plating solutions, [100]. This is slower than deposition rates defined in literature for Ni electroplating onto optical fibre-based sensors, [49, 98, 99].

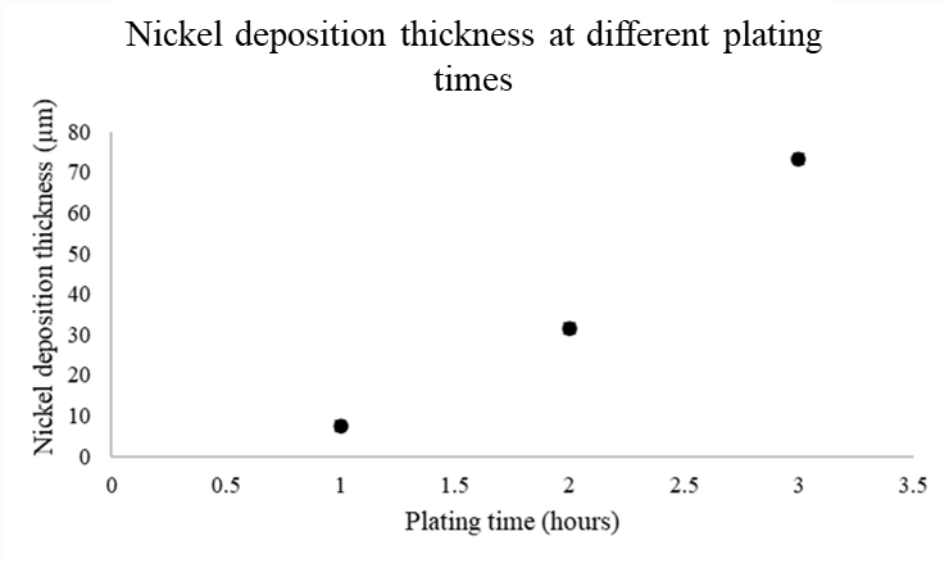

Figure 63 – Graph of deposition thickness against deposition time for electroplating nickel coatings onto 750µm glass capillary tubes.

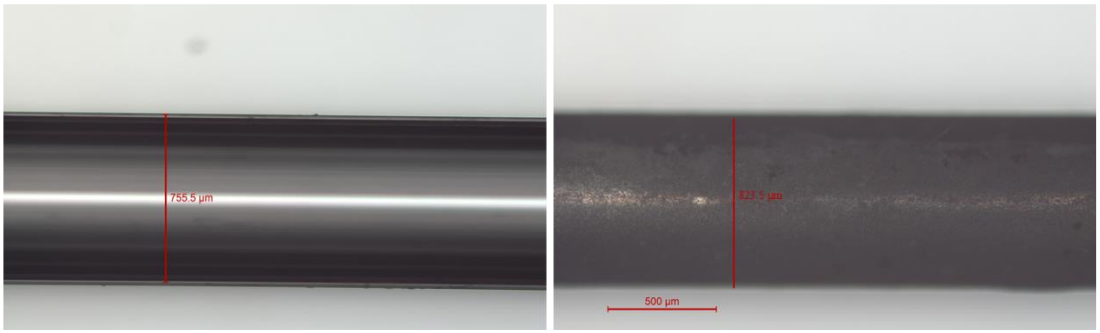

Figure 64 - Image of fibre capillary before and after nickel plating correlating to an increase in diameter of 73µm (from 755.5µm to 823.5µm) at a deposition time of 3 hours. Scale bar represents 500µm. Image taken using a Leica 3D optical surface metrology system.

4.4.3.2 Process Parameters for Achieving Uniform Coatings on Metallised Fibres

Complications arise when reducing the size scales from 750µm capillary tubes to stripped optical fibres with a diameter of approximately 130µm (125µm stripped optical fibre with a 2.5µm Cr coating). At these size scales, it becomes more difficult to house the fibre in the system and detach it from the spindle after the plating procedure due to the brittleness of the stripped optical fibre and susceptibility to breakage during manual handling procedures. Further to this, the reduced conductivity of the Cr layer, smaller plating area requiring a lower current to maintain within the recommended current density range, and smaller points of electrical connection add further complications to the process, combining together to result in a significant reduction in deposition rate.

The primary parameters of interest for achieving uniform nickel deposits on the chrome coated fibres are deposition time, temperature and current. The temperature was set at 40°C, the maximum achievable by the set up and within the recommended range for Watts electrolyte solution [100]. The maximum surface area being plated is approximately $12 \times 10^{-3} dm^2$ which dictates a maximum process current of 8mA in order to maintain a current density below $7 \frac{A}{dm^2}$. In practice, the current was maintained lower (1-3mA) to achieve a good quality, uniform coating. With these parameters, it took 18 hours to deposit a 300µm nickel layer, correlating to an average deposition rate of 16.7µm/hr, slower than the process defined by Li et al., 2006, for Ni electroplating an FBG [98]. A comparison of a nickel-plated, and chrome-coated fibre is given in Figure 65.

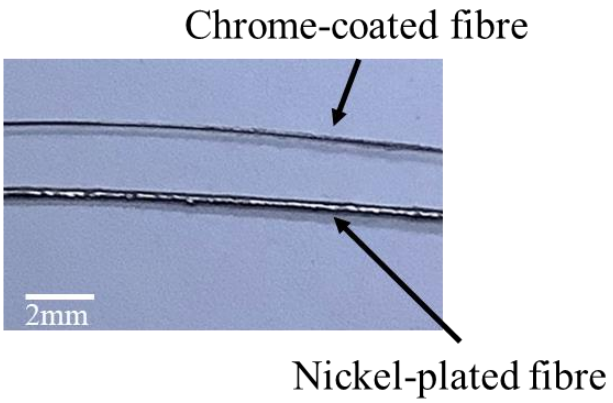

Figure 65 - Comparison of nickel-plated and chrome coated fibres. Nickel deposition = 300µm. chrome deposition = 5µm.

The same preparation, cleaning and metallisation process used for optical fibres was used to coat FBGs, allowing for the FBGs to be embedded into SS-316 coupons, see Chapter 5 Section 2.

4.5 Ductility of Nickel-Plated Fibres

Ductility refers to the deformability of the coated fibre without detriment to the coating of fibre's integrity. This is inherently limited by the bending radius of the fibre ($\approx 10mm$) [103], as deformation beyond this point is likely to result in significant optical loss or fibre breakage. The ability to deform metallised coatings has benefit for applications involving embedding profiles involving design features, such as holes for fasteners or other components. Ductile coatings would be able to bend around these obstacles, as illustrated in Figure 66, improving ease of assembly into complex structures.

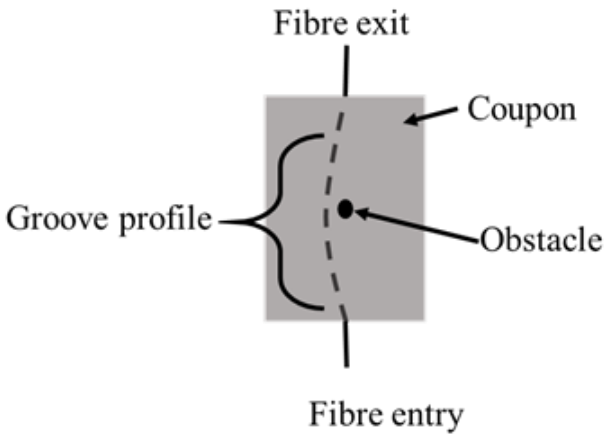

Figure 66 - Illustration of embedding profile around immovable obstacle defined in part design.

Ni coatings deposited using phosphate-based electrolyte solutions typically create brittle depositions with little deformability [50]. Ni layers deposited using the manufactured electroplating system and electrolyte solution similar in composition to the Watts electrolyte solution, retained ductile characteristics, with the ability to hold their deformed position, especially using smaller coating thicknesses.

To demonstrate this, an experiment was conducted in which the metallised fibre section is defined between a FBG which acts as a well-defined reflector and a swept laser FBG interrogation system. This allows a measure of the loss in the fibre between the fibre and the FBG via a measure of attenuation of the reflected FBG signal. This was monitored while the plated fibre was bent around cylinders of varying diameter until failure was observed, see Figure 67 for a schematic illustration of the experimental set up.

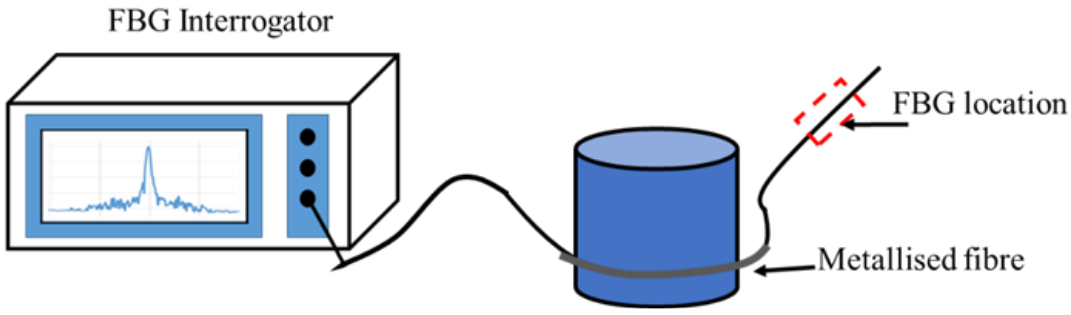

Figure 67 – Schematic of experimental set up for interrogating FBG as metallized fibre length is contorted around cylinders of varying diameter.

An initial test was conducted using a length of uncoated fibre in order to provide a comparison point for future investigations as this will highlight the bend radius at which light propagation is inhibited enough to prohibit sensing capabilities. Figure 68 shows the reflected peak of the reflected peak before the experiment was conducted. To achieve the various bend radii for the uncoated FBG, a loop was made in the fibre around different sizes of cylinder, with radii matching the test cases highlighted in Figure 69. The FBG was then interrogated at decreasing fibre bend radiuses, Figure 69 until the intensity drops to a level where the sensing capabilities of the sensor are inhibited.

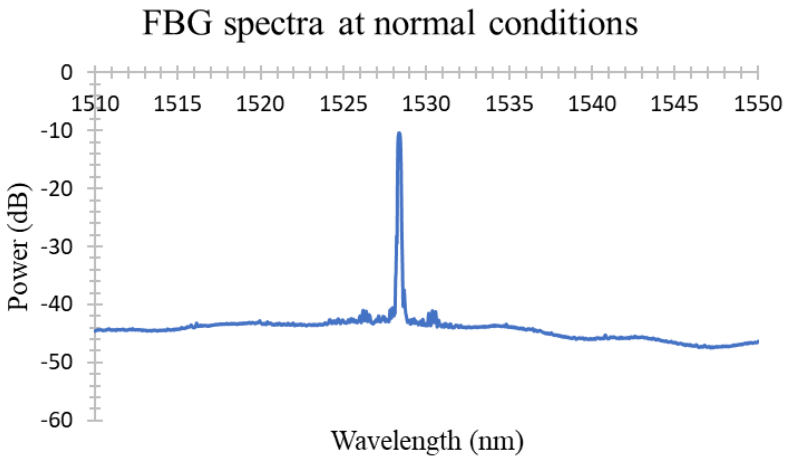

Figure 68 - FBG reflected peak under normal conditions.

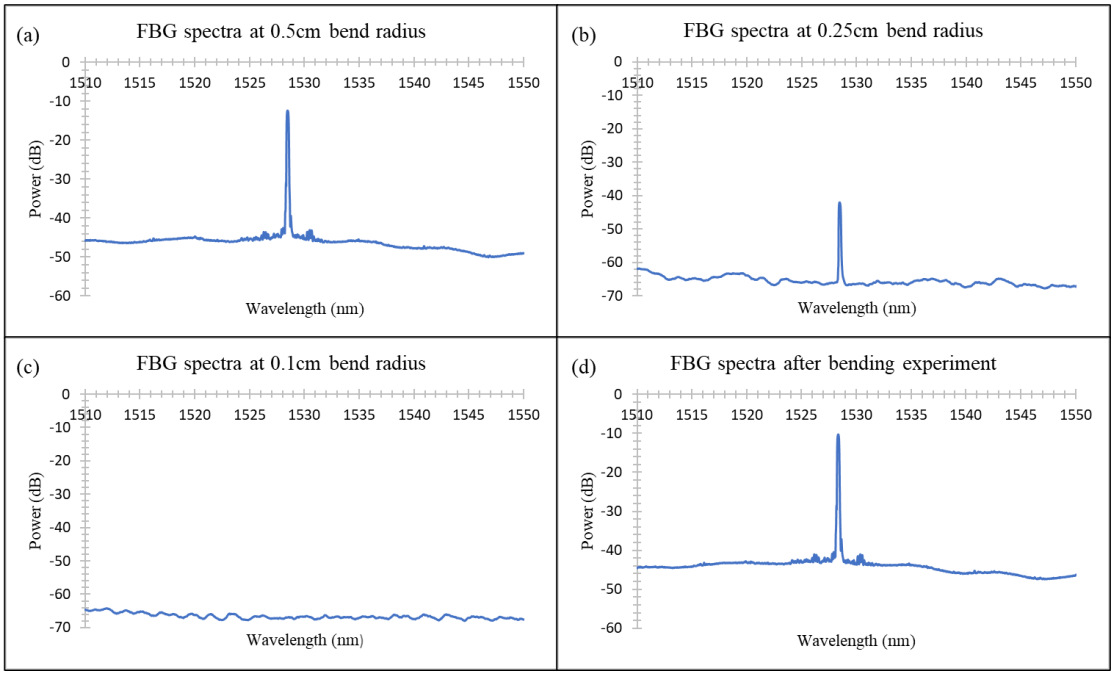

Figure 69 -Spectra of interrogated FBG as fibre is contorted and returned to normal (straight) conditions. Decreasing bend radius to 0.5cm (a), 0.25cm (b), 0.1cm(c).

This approach was repeated for a number of fibres with a range of different thicknesses (150µm and 350µm) to investigate the ductility of coatings with respect to coating thickness. These coatings were then wound around defined diameters until they exhibited failure due to delamination from the fibre. For the 350µm diameter sample, the coating delaminates at a bend radius of 4cm, see Figure 70. This is significantly higher than bare fibre conditions, with little to no discernible deviation in the reflected peak illustrating that the coating failed without damaging the fibre transmission properties.

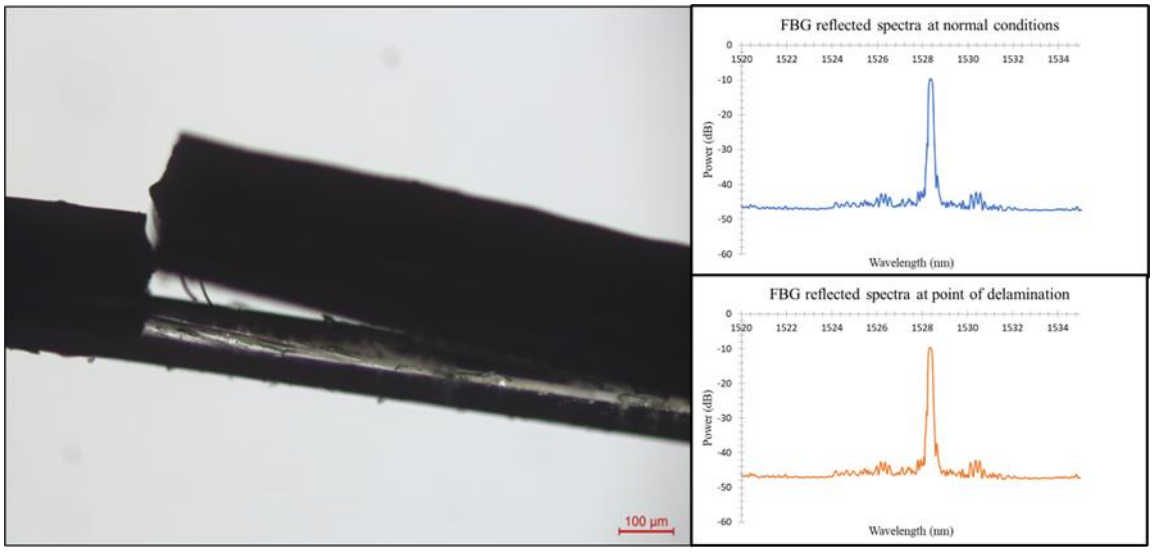

Figure 70 - Image of delaminated coating and spectra at point of delamination (4cm bend radius) compared to normal conditions. Image taken using a Leica 3D optical surface metrology system.

The 150µm sample was more ductile and was able to hold its bend position without detriment to the reflected spectra. Delamination of the coating from the fibre occurred at a fibre bend radius of 0.2cm, see Figure 71, which is below the point the bend inhibits light propagation, Figure 72. This indicates that the limiting factor is the minimum bend radius of the fibre for light transmission with the coating able to operate up to this point without delaminating.

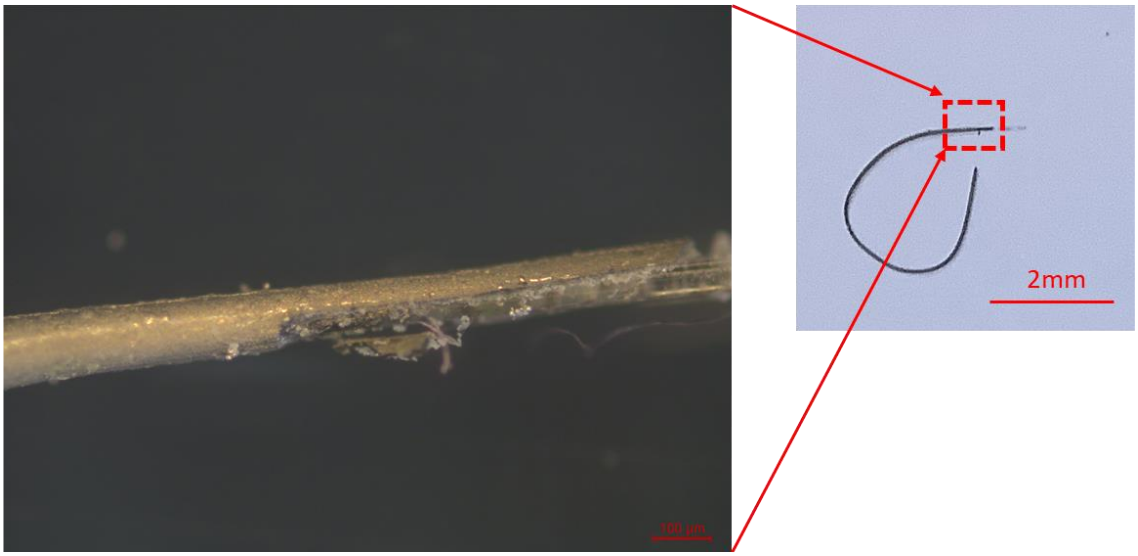

Figure 71 - Delamination point of 150μm coating and image illustrating coating holding bend position. Image taken using a Leica 3D optical surface metrology system.

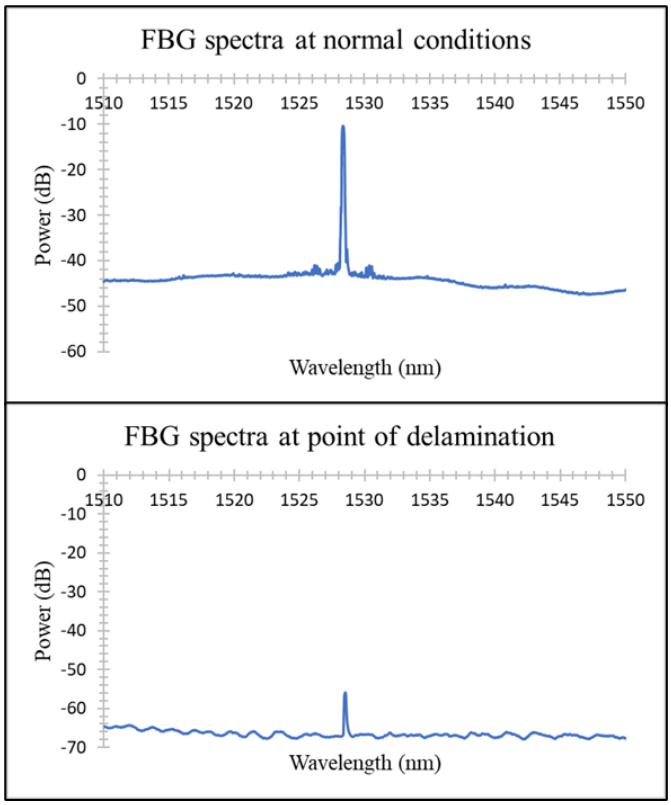

Figure 72 - FBG reflected spectra at point of delamination for 150μm coating and at normal (straight) conditions.

Thicker Ni coatings provide better thermal protection during the embedding process. However, they are less suited for tighter fibre bends which could be of interest for more complex parts. The dominant failure mechanism appears to be delamination of the coating from the fibre as opposed to breakage of the fibre. This has implications for embedding fibres in profiles around obstacles. However, the reduced size scale may be insufficient for protection during the SLM process. It may be possible to combine the benefits of both coatings, by first depositing an initial plating layer ($\leq 150\mu m$) onto a fibre length before continuing the plating process with the shaped fibre to deposit a thicker final coating.

The time extensive metallisation process constrained the investigation to a few samples and would require further investigations to explore in detail. However, the capabilities of the system for achieving ductile Ni coatings are demonstrated, allowing for further investigations into curved fibre depositions and nonlinear embedding profiles.

The same process defined for metallising bare optical fibres was used to successfully deposit protective coatings onto FBGs.

4.6 Chapter Discussion

The purpose of fibre metallisation is to provide shielding against mechanical abrasion and high temperatures that would otherwise damage the optical fibre. For this reason, it is a necessary step for embedding fibres within high melting point metals.

RF sputter deposition is well suited for depositing thin metallic films onto non-conductive materials, such as fused silica glass. Despite other potential processes being applicable for the project requirements, such as dip coating, RF sputter deposition remained the most suitable to the project needs. A fibre rotating assembly was inserted into the vacuum chamber of the RF-sputter deposition system that allowed for uniform chromium coatings to be deposited onto lengths of fused silica fibre. The success of this method is noted, with depositions of around 5µm per hour achieved.

The justification of using chromium rather than nickel is considered in this thesis and reported elsewhere, with specifics relating to its ease of deposition and high deposition rate when compared to other deposition materials [12]. Chromium also exhibits a useful conductivity, which is important for the success of the electroplating process.

The overall success of the RF sputter deposition phase of the fibre-metallisation process is seen within the ability to produce uniform coatings between 5-10µm and is measured by the success of the subsequent electroplating process, as nickel would not deposit successfully onto a chromium layer without adequate electrical conductivity. While chromium depositions higher than 10µm are possible, they unnecessary for the requirements of the nickel electroplating process and require significant deposition times to achieve. It is for this reason that RF-sputter deposition was not used as an "all in one" method for fibre metallisation, and a dual-process involving nickel electroplating is used, which is in line with similar investigations conducted in literature [18, 50].

The ability of the Ni electroplating system to produce Ni deposits up to 500µm is demonstrated. This thickness of coatings has been documented for providing suitable fibre protection during the embedding [12, 50].

The benefits of using a custom electroplating system allow for full flexibility of the electroplating process parameters. This is important within fibre-metallisation exercises as individual systems require extensive calibration to find the optimal processing parameters for operation and the complexity rises with the deposition of coatings onto cylindrical objects on the scale of an optical fibre (130µm in diameter including the RF coating). These size regimes additionally cause the process to take longer than predicted as the process must be operated at the lower echelons of the current range of the power supply (1-3mA) in order to ensure suitable, uniform coating. This meant that deposition times were longer than commercial systems, [50, 100]. However, the custom system allowed for full control of the process, which is not commercially available for such samples.

Using the custom system, every feature of the process could be altered in real time during the deposition such as temperature, level of agitation, substrate orientation/spacing, with the exception of the constitutional chemical components of the electrolyte which remained unaltered throughout. This level of flexibility allowed for a greater understanding of the process and its implementation, including practical issues such as fibre handling, and coating surface finish.

The ability to produce ductile nickel coatings is something that has not been documented or achieved before during similar investigations. This was a welcome by-product of the custom system under the specific operating conditions and processing parameters, as previous studies into the coating of optical fibres in nickel highlight the inherent brittleness of nickel deposits [50]. Therefore, producing ductile nickel coated fibres widens the operational viability of the metallised fibres to include embedding around immovable components, features, or other "obstacles" within the embedding path. While this will require further development, the fundamental ability to deposit ductile nickel coatings onto optical fibres is demonstrated.

There is scope for the adjustment of the system to improve plating efficiency, such as operating the deposition process inside a fully enclosed container with electrolyte circulated inside using a pump. This would not only reduce the loss of electrolyte due to condensation during the electroplating process while providing a means of agitation to reduce the formation of hydrogen bubbles forming on the substrate surface. However, such modifications would be at the detriment of ease of access of the system's components during operation and can only be taken forward now that the process using this specific mechanical and chemical set-up has been clearly defined and investigated in full.

4.7 Chapter Review & Conclusions

A fibre metallisation process was demonstrated using a combination of RF sputter deposition of chromium and electroplating of nickel in order to provide a protective metallic jacket for embedding fibres via ALM. Depositing uniform metallic coatings onto stripped optical fibres is a non-trivial process on account of the dimensional scale of the required coatings. RF sputter deposition allowed for the deposition of thin (micron scale) Cr films to form a keying layer onto a stripped fused silica fibre. This Cr film provides a conductive keying layer for the subsequent Ni electroplating process, which required the design, development and characterisation of a custom electroplating system for the purpose of depositing nickel coatings onto the chrome-coated fibre lengths.

Deposition time remains the main constraining factor for the process as both stages of the metallisation process takes up to 24 working hours in order to complete in full, with various points of failure at every stage. The most prominent of these failure mechanisms occurs during manual handling of the metallised fibre. This form of failure was mitigated by retaining the same fibre-holder used for the rotary system inside the RF sputter deposition chamber. However, elements of risk still exist within the boundary of the stripped fibre length and metal coating. This was mitigated by covering these regions in a removable viscous material, such as petroleum jelly, but this method must be used with caution, as using too much may alter the chemical make-up of the electrolyte that could reduce plating efficiency and coating integrity.

Further to this, full automation of the metallisation phase could not be achieved due to the staged process and requirement of supervision for operational safety. Despite these difficulties, a reliable repeatable process was defined whereby thick coatings ($350 - 500\mu m$) of nickel were deposited onto stripped FBGs, see Chapter 5.

A benefit of the nickel electroplating system was the inherent ductility of the nickel coatings, that allowed for bending of the metallised fibre. This has benefits for applications requiring non-linear embedding profiles such as parts containing operational components than cannot be removed from the embedding path.

Further work would be required to fine-tune the mechanical set up for the plating system, but the investigations highlighted in Chapter 4 illustrate the capabilities of the dual-process approach for fibre metallisation, a vital part of the fibre embedding process for ensuring fibre survivability, without detriment to the sensing component.

Chapter 5 - Embedding Fibre Bragg Gratings in 3D Printed Stainless Steel Components

This chapter brings together work in previous chapters and explores the process of embedding FBG sensors, metallised in accordance with Chapter 4, within SS-316 coupons, manufactured using the SLM defined and calibrated within Chapter 3. The FBG was interrogated in-situ during the embedding process to monitor for any spectral changes which could indicate potential damage to the fibre and/or FBG. The embedded sensor is calibrated in the embedded part, and operation over extended temperature cycling experiments is demonstrated. The chapter then concludes by discussing methods for achieving strain isolation in order to conduct temperature-independent strain cycling experiments.

The small feature sizes achievable by the SLM process are well suited to fibre embedding procedures which take place on the sub-millimeter scale. Appropriate laser parameters are chosen to restrict the melt pool spatially. And thereby the heat affected zone is controlled and minimised to reduce the risk of damage to the embedded fibre. Modifications to the laser power, hatch spacing, and scanning velocity are made to the first layer deposited on top of the metallised FBG to limit the instantaneous heat input to the fibre and limit uneven temperature gradients inducing thermal stresses across the fibre assembly. This must be accomplished without compromising the build quality of the surrounding part.

The incident laser scanning profile is chosen to be parallel to the embedded fibre direction for the first layer printed over the FBG, while the power is reduced by approximately 10% in order to limit the phenomenon of thermal stresses working to push the fibre out of the groove which would be prevalent under a laser scanning profile perpendicular to the embedded fibre, see Figure 73 and Figure 74. Here, the top surface of the fibre is under compression as it cools, with the underside under tension, which pushes the fibre out of the desired embedding profile. This makes the fibre coating susceptible to damage within the fibre coating region now held under tension, see Figure 74.

The fibre metallisation process defined in Chapter 4 is used to protect the fibre during the embedding process and aid bonding of the fibre to the surrounding SS-316 material. Before embedding FBGs, the embedding process was first optimised using nickel wire and then for nickel coated SMF-28 fibres, in order to minimise the number of nickel-coated FBGs used during the experimentation and process calibration.

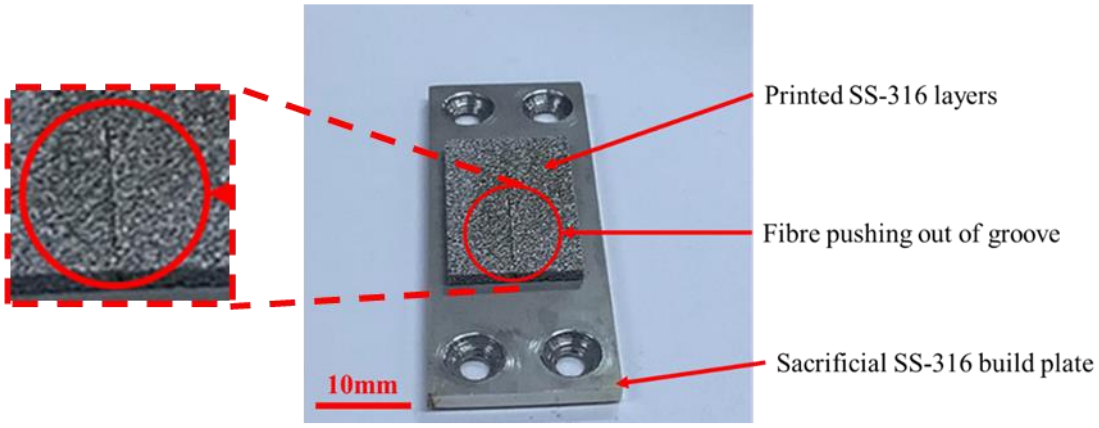

Figure 73 - Embedded sample illustrating fibre pushing out of the groove due to thermal stresses induced by the embedding process.

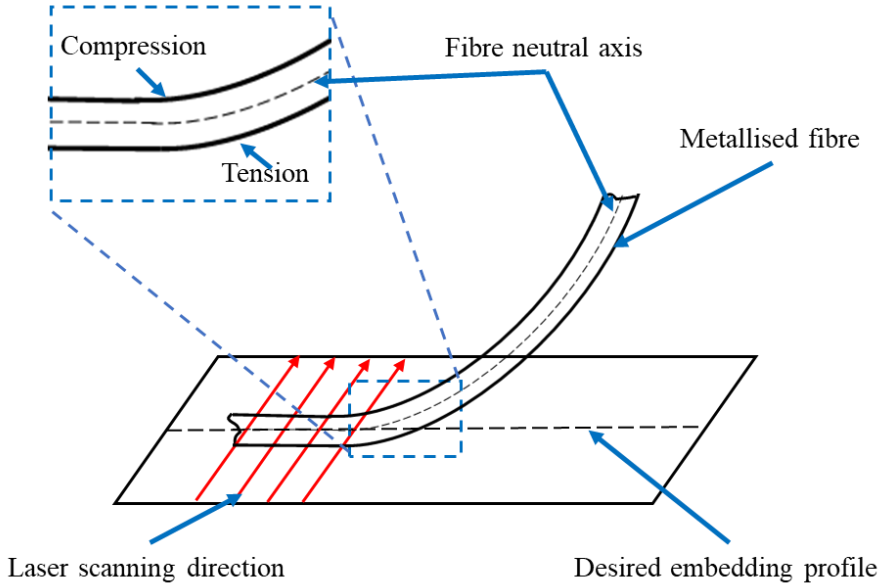

Figure 74 - Graphical representation of fibre being pushed from the groove due to compressive and tensile forces exhibited due to laser scanning direction perpendicular to the embedding profile.

5.1 Embedded Metallised Fibre

Initial embedding tests were conducted with nickel wire of diameter 400µm, which is approximately the same size scales as the metallized fibres, see Figure 75. This allowed experience to be gained inserting and aligning the fibre substitute, as well as initial modification to the build parameters without the need for time-consuming coating steps required when using an actual fibre. As a result of these tests, initial laser parameters for the embedding procedure are defined (laser power: 100W, scan speed: 300mm/s, hatch spacing: 60µm, layer thickness:100µm, laser spot size 100µm), that allow for bonding of the nickel wire/metallised fibre to the top material layer.

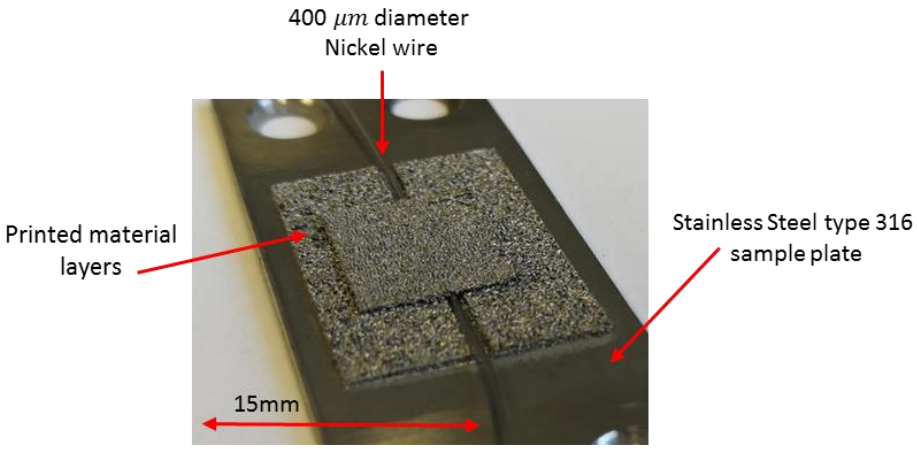

Figure 75 - Nickel wire embedded in printed SS 316 coupon.

Following on from nickel wire, a fibre was put through the metallisation process defined in Chapter 4 and embedded into a SS-316 coupon, see Figure 76.

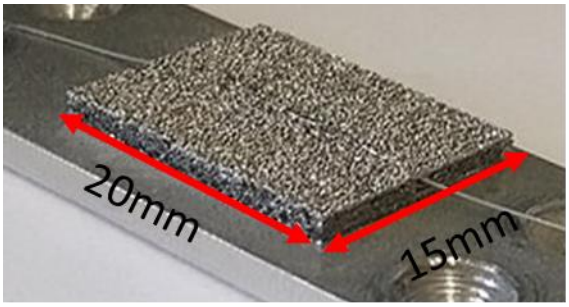

Figure 76 - Embedded metallised fibre inside SS-316 coupon.

Testing the transmission of the fibre was achieved using a visible "fault finder" shown in Figure 77. This provides a quick test to check there has not been complete failure of the fibre due to embedding (i.e., a crack across the fibre).

The coupon was manufactured with the build parameters highlighted in Table 10. As it is required to reduce the laser power above the metallised fibre, the laser power was reduced by 10% of its optimised maximum to 90W and the hatch spacing increased to 0.1mm for the first layer printed over the metallised fibre to ensure that the fibre is not subjected to as many laser scans as a conventional printed layer. Both parameter adjustments aid survivability of the embedded fibre, illustrated by the successful propagation of light through the embedded section, Figure 77.

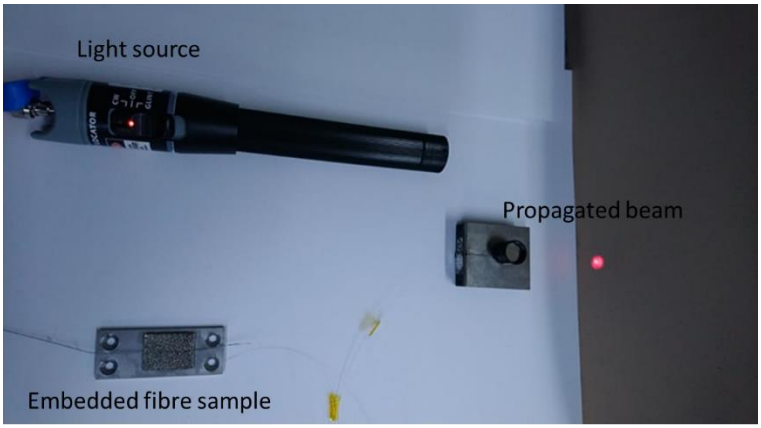

Figure 77 - Experimental set up for determining light propagation through the embedded section.

Parameter	Value
Laser Power	100W
Scan Velocity	300mm/s
Scan orientation	(0°,90°,180°,270°,0°)
Hatch spacing	0.06mm
Layer Height	≈ 100μm

Table 10 – Coupon build parameters used for the embedding of the metallised fibre.

5.1.1 Optical Losses Within Embedded Fibres

The presence of any excess loss within the fibre indicates potential issues in the embedding process. This could be introduction of micro-bends that increase scatter (and hence loss) or could be some form of damage to the fibre resulting in an increase in attenuation. To quantify this, an experiment was conducted where light from a broadband source was coupled into the fibre, and the output monitored using a photodetector, see Figure 78.

In addition to measuring the output power of the entire embedded system, the optical power was measured before the embedded section to determine the power incident upon the embedded region. Using this method, the power excess loss as a result of the embedded section of fibre was measured for four embedded samples ranged from 8% up to 18%, for an average loss of 12.75% and standard deviation of 3.7%. This shows that a significant proportion of the propagated light is being lost, indicating fibre damage or micro-bending induced by the embedding procedure. For short lengths of embedded fibre this may be acceptable, but it limits the usefulness of this process for longer lengths of embedded fibre unless this loss can be reduced.

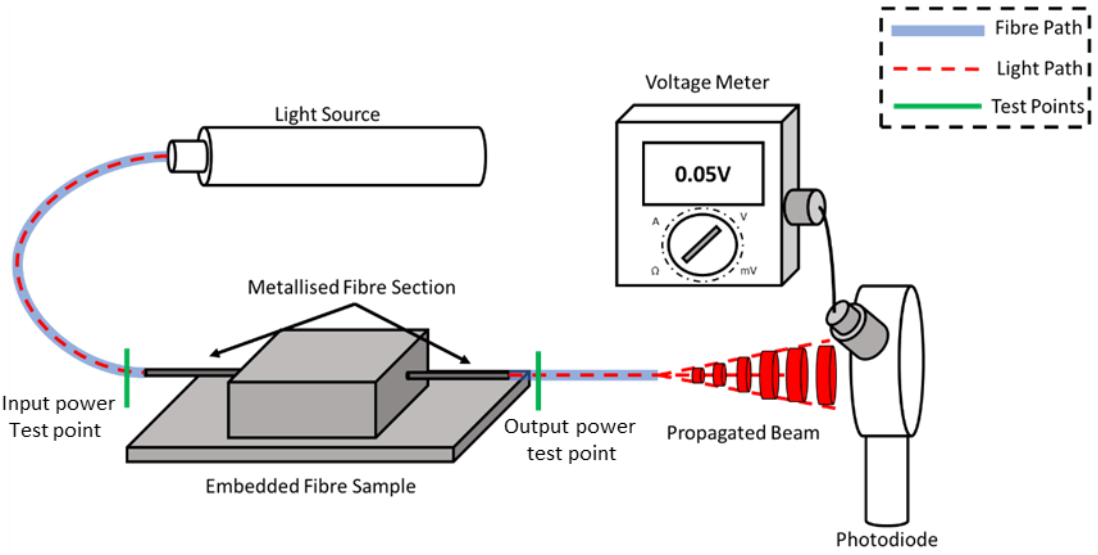

Figure 78 - Schematic diagram of experimental set up to measure optical losses within embedded fibres, where light from a broadband source is coupled into the fibre, and the output monitored using a photodetector.

5.2 Embedded FBG Sensor

The same embedding process as defined in section 5.1 was employed to embed FBGs inside SS-316 coupons. Prior to the embedding process the FBG location needs to be precisely known to ensure that it can be correctly aligned to the sample part. The position of the FBG was identified by using localised heating using a heated soldering iron tip on a translation stage and passing it close to the sensor while its spectra is interrogated, see Figure 79. As the soldering iron tip passes over the FBG location, the reflected spectra distorts in account of the localised heating within this region. The FBG position could then be recorded relative to a reference mark on the fibre.

This technique could determine FBG location to within 2mm. However, as the FBG is far smaller than the metallised section of the fibre, 5mm and 100mm respectively, it is suitable for ensuring that the FBG is approximately within the centre of the metallised section. Therefore, it can be ensured that the FBGs are located within consistent regions far from the edges of the printed SS-316 coupons.

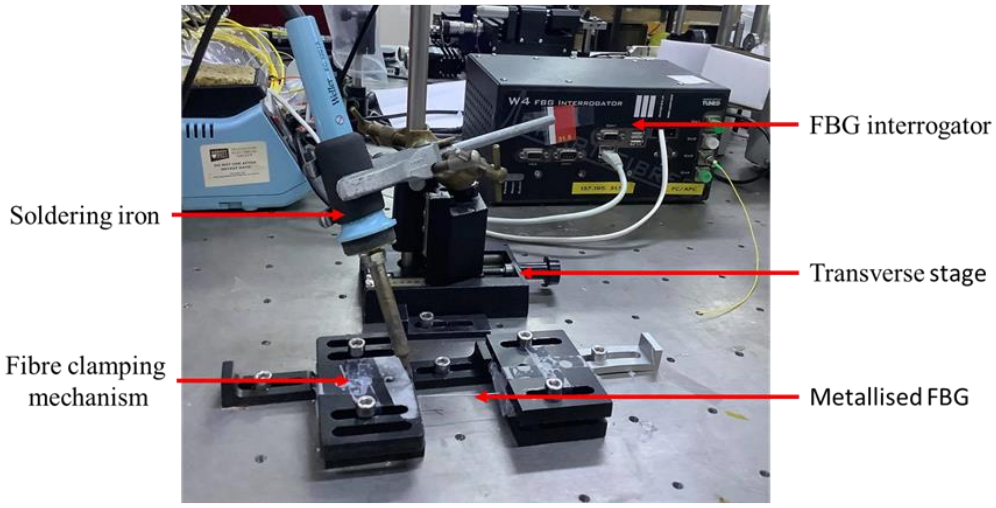

Figure 79 - Photograph illustrating set up for determining the FBG location within a metallised section of fibre.

5.2.1 Spectral Analysis In-Situ of Embedding Process

One of the benefits of using FBG sensors is their ability to be interrogated during the embedding process. This allows for real-time monitoring of the behavior of the reflected spectra during embedding and allows for rapid indication of potential damage that occurs due to the instantaneous heat of the lasing process. As a result, build parameters can be optimised during the embedding process, preventing cumulative damage to the FBG that would inhibit its sensing capabilities.

The investigation follows the schematic diagram in Figure 80 illustrating the experimental set up used to interrogate the FBG during embedding process. This methodology was used to develop the set up shown in Figure 81. One end of the fibre is fixed in place beyond the embedded region, while the opposite end is connected to a Micron Optics (WG4) FBG interrogator. This is a commercially available scanned laser interrogator that allows the FBG reflected spectra to be measured (at a rate of 1Hz) during the embedding process.

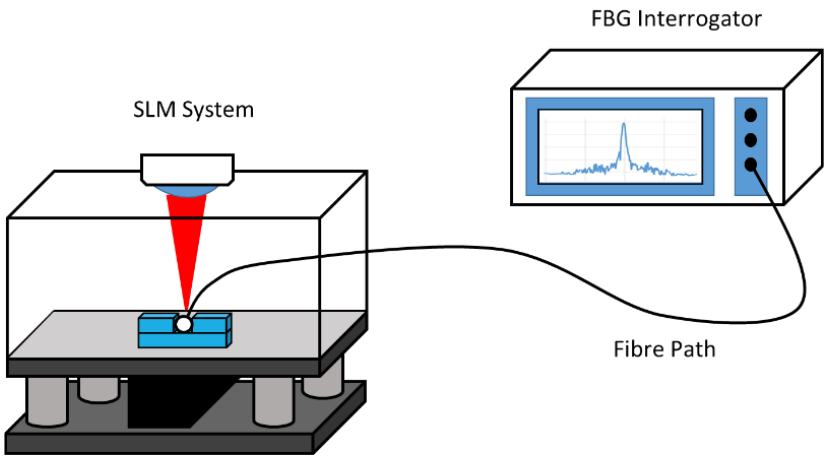

Figure 80 - Schematic illustration of experimental set up for using a Micron Optics (WG4) FBG interrogator to interrogate FBG during the embedding process.

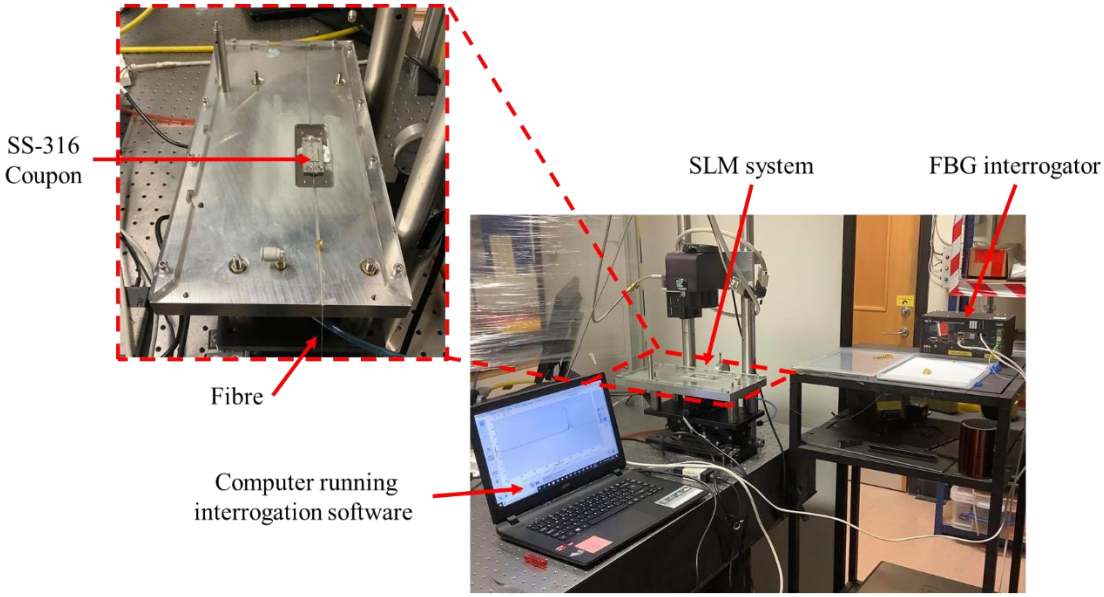

Figure 81 - Experimental set up for interrogating FBG during the embedding process.

Figure 82 shows the reflected spectra as the embedding proceeds. It is observed that the reflected spectra broadens and recovers as the laser passes over the sensor during the embedding process. This phenomenon is attributed to the FBG sensor being subject to a strain or temperature gradient [104]. These gradients arise due to the localised heating during the laser scanning procedure. As the bulk material cools back to ambient conditions, the temperature gradients across the coupon diminish, and with a uniform temperature the spectra to settles down to recover the original distinctive single reflected peak with only a small decrease in power (0.62dB, from Figure 83). This indicates that no significant fibre damage occurred during this embedding process, highlighting that the 400µm diameter nickel coating was sufficient to protect the sensor during the embedding process. This experiment was repeated during subsequent embedding procedures to ensure sensor survivability, with nickel coatings maintained above 400µm.

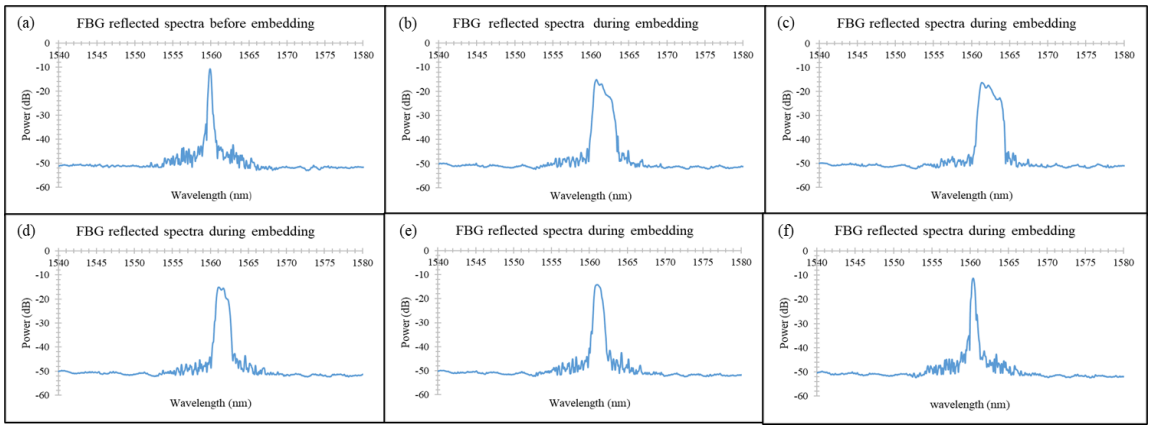

Figure 82 - Reflected spectra measured in-situ of the embedding process, showing the survivability of the embedded sensor with a nickel coating diameter of 400µm. The lasing process follows the order of the graphs in alphabetical order, (a) – (f).

A comparison of the reflected spectra before and after the embedding process is given in Figure 83, highlights a residual wavelength shift as a result of the embedding procedure due to strain induced by the surrounding bulk material. However, this is expected and not in detriment to the FBG's sensing capabilities.

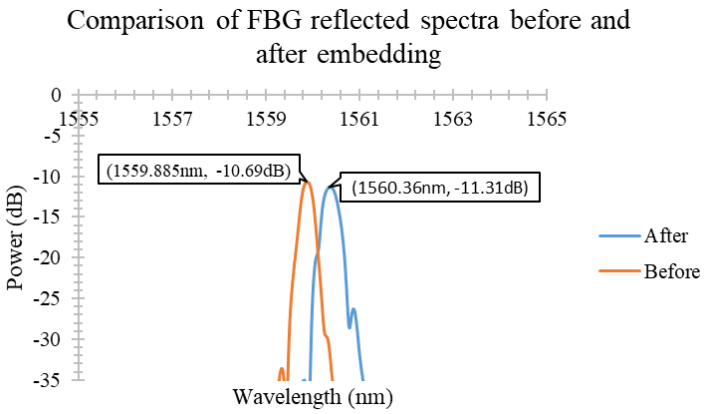

Figure 83 - Comparison of FBG reflected spectra before and after the embedding procedure, illustrating resulting shift in wavelength and intensity.

For comparison a FBG without a protective metal coating was embedded into a SS-316 coupon, and the spectra was recorded during the process in the same manner as before, see Figure 84. Clearly, the intensity of the reflected peak drops to a point where the non-metallised FBG does not return sufficient power for reliable sensing operation due to increased fibre attenuation and FBG annealing affects. This further highlights the importance of the nickel coating in protecting the FBG during the embedding procedure.

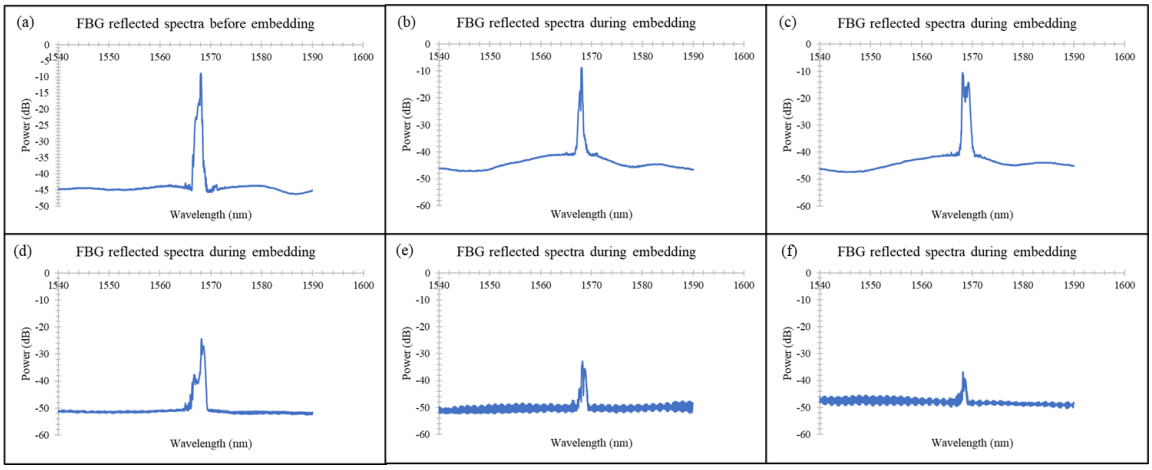

Figure 84 - Reflected spectra of a non-metallised FBG during the embedding procedure. Arrows indicate process flow. The lasing process follows the order of the graphs, going in alphabetical order (a) – (f).

5.3 Temperature Cycling of Embedded FBG Sensor

After the embedding process, a practical sensor requires recalibration, for example by subjecting to it to an extended temperature cycling procedure. This allows for the determination of the sensor's sensitivity, which can be used to convert changings in the reflected Bragg wavelength to temperature. These initial studies also allowed the sensor's performance and survivability at elevated temperatures ($> 100°C$) to be examined.

5.3.1 Experimental Configuration

The experimental set up is highlighted in Figure 85. Heating of the embedded sensor is provided by an oven capable of temperature control within the desired temperature range ($21°C - 120°C$). The coupon housing the embedded sensor is placed inside a bulk block of SS-316 to promote uniform heating and cooling of the coupon with respect to its surroundings. Four thermocouples were placed within close proximity of the FBG to get accurate correlation of the temperature the FBG is subjected to during the temperature cycling process, Figure 86.

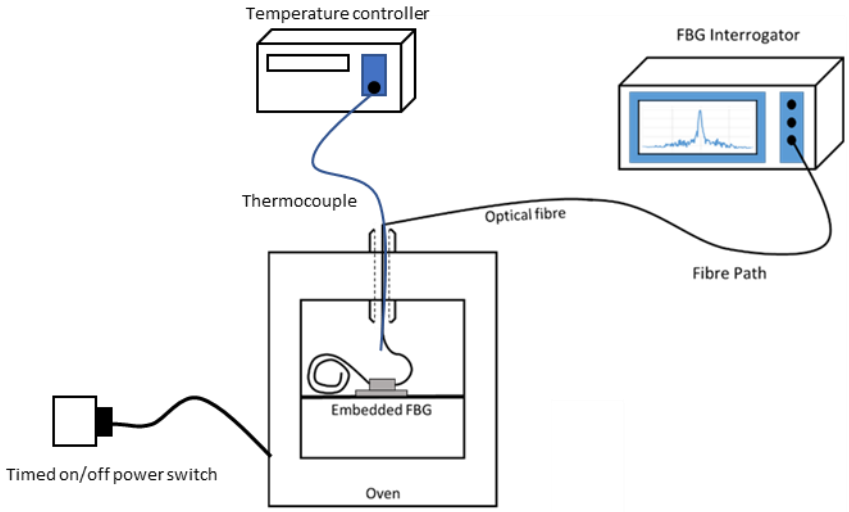

Figure 85 - Schematic diagram of the experimental set up for temperature cycling of the embedded FBG.

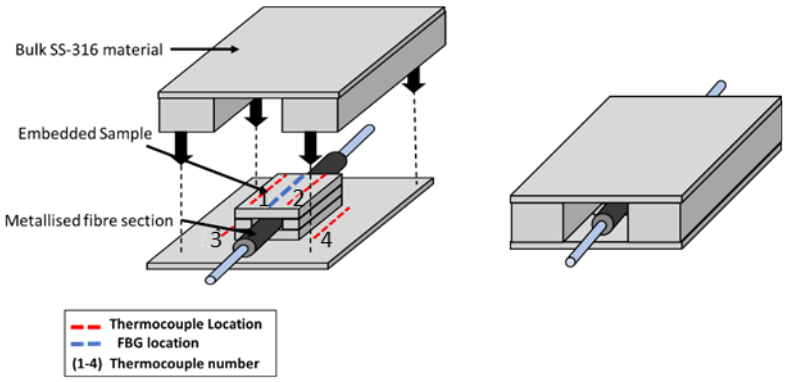

Figure 86 - Illustration of assembly inside the oven, indicating locations of the FBG and thermocouples.

5.3.2 Extended Temperature Cycling

The embedded FBG was subjected to an extended temperature cycling experiment in order to determine the survivability and repeatability of the sensor, whereby the temperature was repeatedly cycled from ambient to 100°C for 44 cycles over 12 days, with a hold time at 100°C of 3 hours for each cycle. These temperature cycles were also used to calibrate the sensitivity of the sensor. Figure 87 illustrates the FBG reflected spectra prior to temperature cycling as a benchmark for comparison. From Figure 87 we can determine the Bragg wavelength at ambient conditions for the grating, 1565.715nm, taken as the peak value of the reflected spectra, which provides a reference point for any deviations in the Bragg wavelength in account of the temperature cycling process.

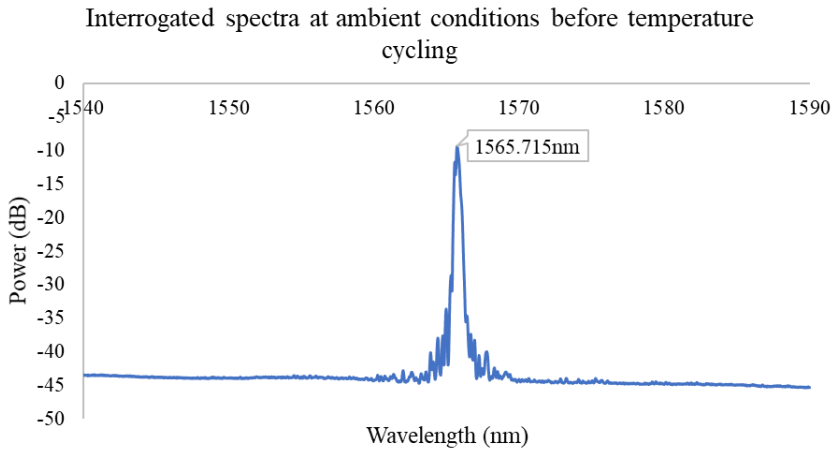

Figure 87 - Reflected Bragg wavelength at ambient conditions before temperature cycling experiments.

The extended temperature cycling experiment was conducted for twelve consecutive days, see Figure 89 - Figure 91, in order to provide enough data for the determination of the sensor's reliability in operation which would not subject the sensor to elevated temperatures as frequently or for as long a time period. The temperature profile given relates to the thermocouple closest to the FBG inside the bulk SS-316 block as it provides the closest match to FBG temperature due to locational limitations inhibiting how close the thermocouples could be placed to the embedded sensor. The temperature cycle is divided into three traces in order to improve data processing efficiency and aid in visualization of the data features. The change in reflected spectra from ambient, low temperature conditions (≈ 21°C) to high temperature conditions (110°C) is provided in Figure 88 , correlating to a Bragg wavelength shift of 1.53nm.

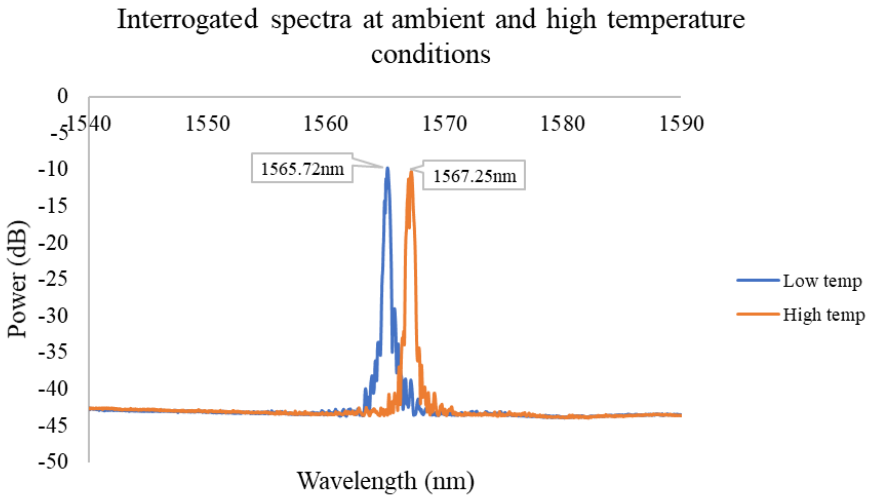

Figure 88 - Change in reflected Bragg wavelength (1.53nm) in account of heating from ambient temperature (≈ 21°C) temperature to 110°C.

During the initial temperature cycle, the peak temperature and wavelength correspond to 100°C and 1567.25nm respectively. As the temperature cycling progressed, the reflected wavelength is seen to decrease with each subsequent temperature cycle, as shown in Figure 89. This suggests that the temperature cycling is affecting the sensing properties of the grating. This continuous degradation visualized in the FBG readings continues as the temperature cycling is extended, Figure 90, Figure 91. This is indicative of change within the embedded grating. However, because it is a slow degradation, this rules out typical fibre failure mechanisms that would result in a sudden drop or change in return intensity of spectral position, such as fibre breakage or slippage within the groove.

The slow degradation may instead be indicative of changes in the sensing properties of the FBG in account of continuous high temperatures, causing annealing affects within the grating known to result in wavelength drifts [42, 105].

Further to this, the repeated temperature cycling may also act as a mechanical annealing process that slowly removes any residual stress frozen into the fibre-coupon assembly, which would also help explain the reduction of this effect over time. The cumulative response of the temperature cycling on the reflected spectra can be visualized in Figure 92, showing the reflected peak before and after the temperature cycling process. The resulting wavelength shift is not ideal, and may result in a sensor calibration issue.

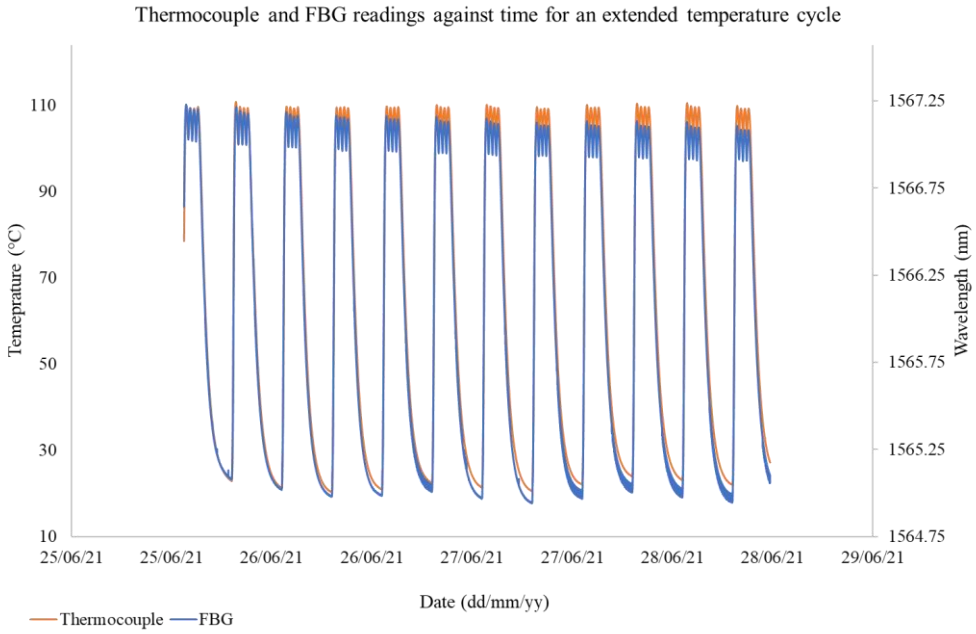

Figure 89 - Thermocouple and FBG readings for extended temperature cycle 25/6/21 - 28/6/21.

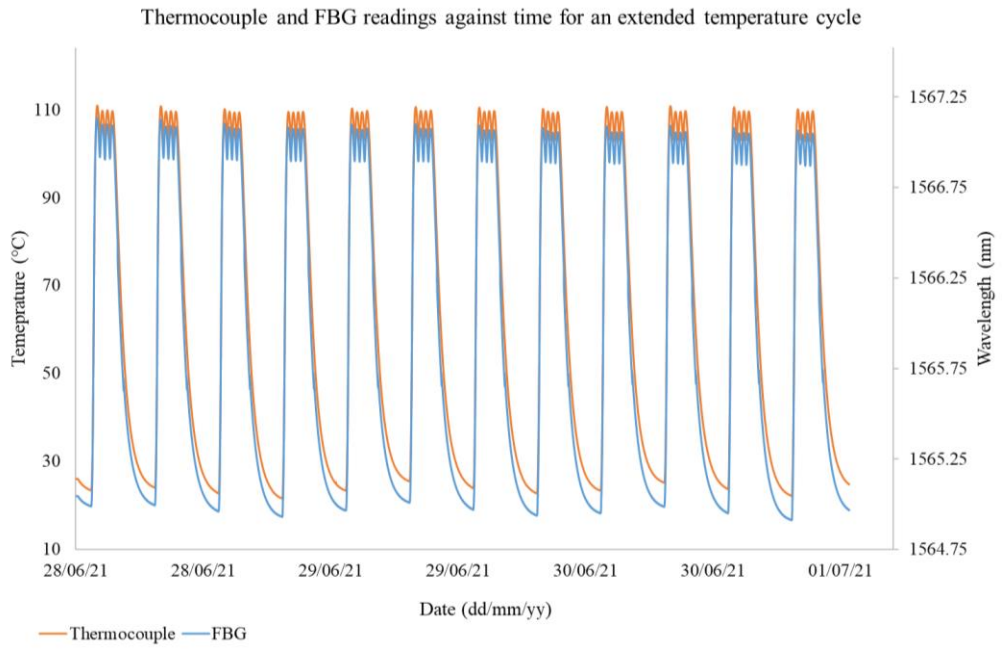

Figure 90 - Thermocouple and FBG readings for extended temperature cycle 28/6/21 - 02/7/21.

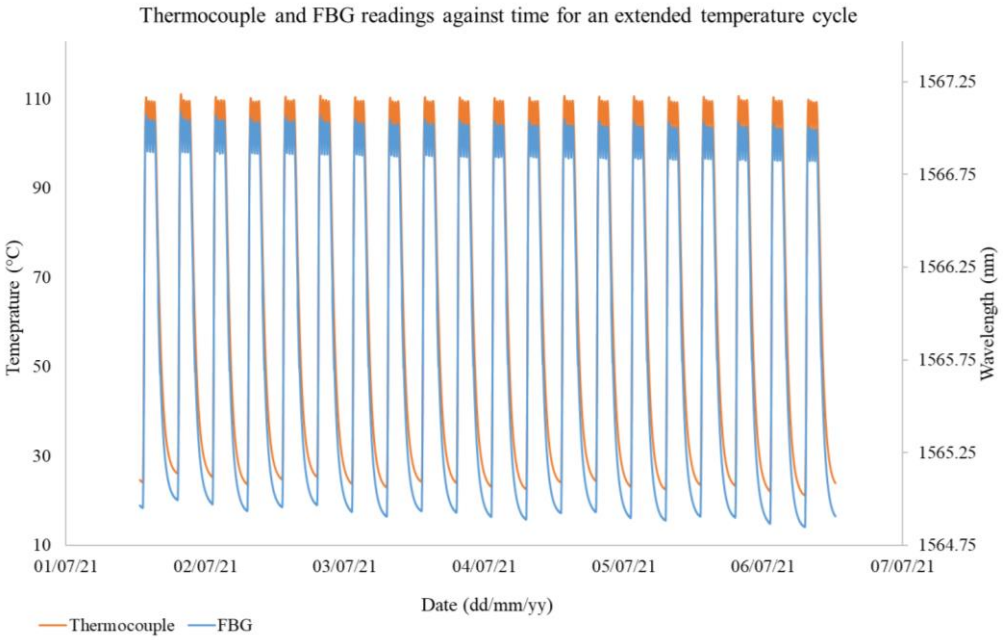

Figure 91 - Thermocouple and FBG readings against time for an extended temperature cycle 1/7/21 - 7/7/21.

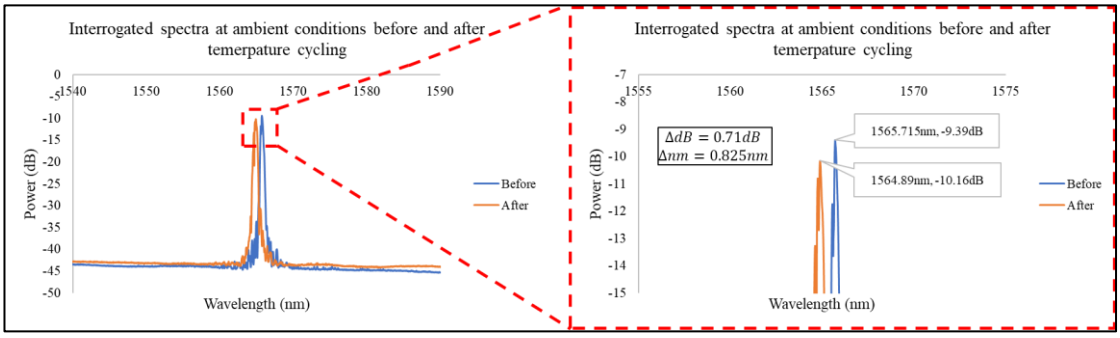

Figure 92 - Figure of FBG reflected spectra at ambient (26°C) conditions, before and after extended temperature cycling, highlighting resulting change in reflected power and wavelength. Laboratory temperature was controlled during the temperature cycling process to maintain consistent ambient (low temperature) conditions.

Noise levels within the temperature cycling experiments were determined from the ambient conditions (26°C). The signal noise is taken to be two times the standard deviation in order to give a measure of the experimental error.

Over a range of measurements taken at ambient conditions, the mean temperature and wavelength readings were determined to be of 26.13°C and 1565.04nm respectively. From this data subset, the standard deviation was calculated, see Table 11, which gives an indication of the data spread around a consistent measurement reading, correlating to the experimental system noise levels. In the case of the 2-sigma error for the temperature and wavelength readings, this can be taken as $\pm$0.4°C and $\pm$1.4pm respectively.

Sigma amount	Percentage of values within sigma boundaries	Standard deviation of temperature readings (°C)	Standard deviation of FBG wavelength readings (nm)
σ	68.2%	0.0187	0.00069
2σ	95.4%	0.0374	0.00139
3σ	99.6%	0.0561	0.00208

Table 11 - Noise levels of experimental equipment, calculated from standard deviation of values from ambient conditions (26°C).

From the thermocouple and FBG data taken during the extended temperature cycle, it is possible to obtain a grating sensitivity from a trace of temperature against wavelength, Figure 93. This is a calibration factor for the embedded FBG which allows for determination of the temperature from a known wavelength reading. From Figure 93, the sensitivity was calculated as approximately $25\frac{pm}{°C}$ taken from a line of best fit through the centre of the data set.

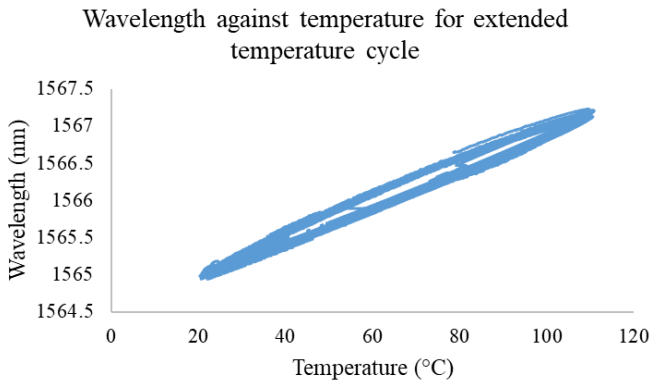

Figure 93 - Wavelength against time for extended temperature cycling experiment.

5.3.3 Elevated Temperature Cycling

From the previous section, it can be concluded that the embedded FBG survives extended temperature cycling between ambient and 100°C. However, subjecting the embedded grating to higher temperatures allows for a better insight into high temperature applications, and also provides additional evidence to demonstrate sensor life. Higher temperatures increase the chance of potential fibre damage and grating annealing effects which result in sensor degradation. Although some evidence of annealing was observed at lower temperatures, it should become more prevalent at higher temperatures.

In order to ensure reliability of embedded sensor performance, and further investigate annealing effects, a new sample was prepared following the same embedding procedure. The spectra of the embedded FBG before it was subjected to a temperature cycle taking it from ambient conditions to 120°C and holding it there for an extended period before letting the FBG cool back to ambient conditions. A further interrogation of the reflected spectra is then carried to determine any changes in account of the temperature cycle.

A trace of the temperature and FBG readings against time is illustrated in Figure 94. As before, thermocouples 1 and 2 refer to the temperature probes within closest proximity to the embedded FBG, as illustrated in Figure 86. The thermocouple and FBG data were matched at the point of high temperature, which allows visualization of the disparity between the respective cooling cycles of the FBG and thermocouples. This is in account of the sensor locations inside the oven with the embedded grating taking longer to cool due to its encapsulation within SS-316. While the sensing block containing the embedded FBG and thermocouples allows for a better temperature match, there remains disparity at the lower echelons of the temperature range due to the respective sensor locations.

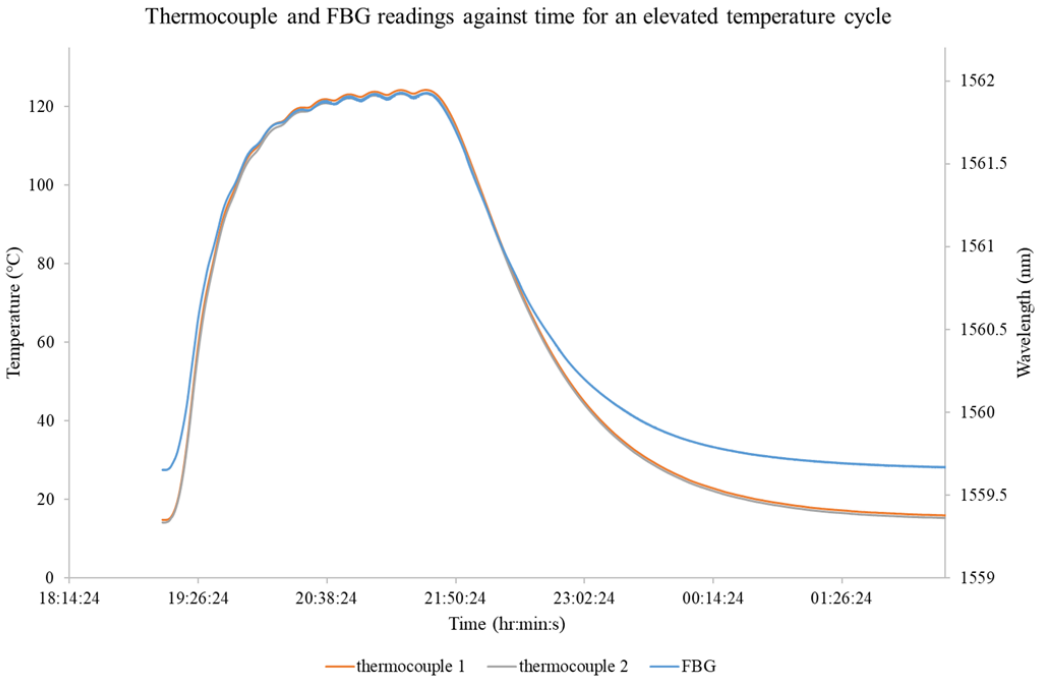

Figure 94 - Thermocouple and FBG readings against time for elevated temperature cycle.

The reflected peak was interrogated before and after the elevated temperature cycle, Figure 95, showing the change in the reflected Bragg wavelength in account of a single elevated temperature cycle experiment.

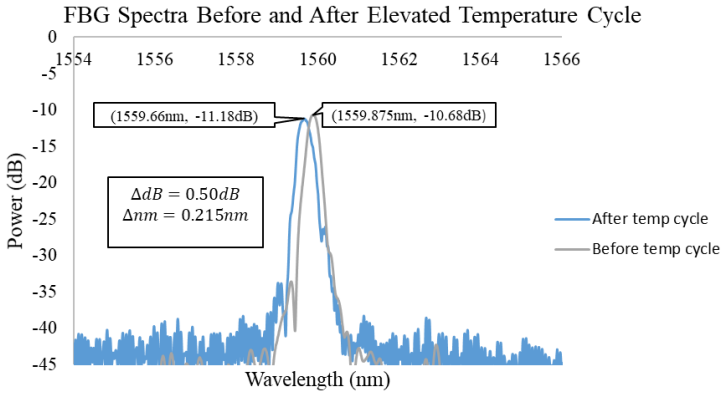

Figure 95 - FBG spectra before and after elevated temperature cycle, taken at ambient conditions (~21°C).

Direct comparison of the sensing capacities of the different FBGs used for the elevated and extended temperature cycling experiments is difficult due variability in the embedding process and sensor performance. However, it can be deduced that degradation of the sensing capabilities of the embedded sensor is more prevalent for extended, repeated temperature cycling, indicating that small changes in the reflected spectra occur within each cycle, with their resulting effect combining to form a larger shift in the reflected spectra.

5.3.4 Temperature Cycling Further Work

Temperature cycling experiments were limited by the number of samples that could be produced due to sample yield and process time. Further experimentation is required to investigate the wavelength creep seen over the course of the temperature cycling experiments. This would require further extended temperature cycling of different samples for longer periods to see if the degradation and settling is consistent throughout multiple embedded FBGs. This would allow for determination as to whether the FBGs used are exhibiting annealing effects of if the degradation was as a result of other mechanisms.

Wavelength drift during temperature cycling is a typical feature of FBG instability due to annealing effects [42]. Therefore, repeating the temperature cycling experiments with pre-annealed sensors that will not anneal over the tested temperature range, and compare with 'normal' un-annealed FBGs. However, the sample size of each case would be limited to the processing time of the embedding process. It is also possible to conduct pre-annealing experiments subjecting, subjecting the FBG to 400℃ until the drift no longer occurs and comparing to a 'normal' embedded FBG [105].

Increasing the temperature beyond that of the elevated temperature cycling (120℃) would allow for better determination of any fibre damage as a result of subjecting the embedded FBG to elevated temperatures. The projected experiment would retain the same experimental set up as defined in section 6.4.1, although the maximum temperature would be increased from 120℃ to 400℃, in line with FBG pre-annealing procedures [105] , with the hold time increased from 3 hours to 6 hours to determine sensor performance within these temperature regimes. Further experiments where the temperature is lowered back to 120℃ will determine if the temperature stability can be increased after pre-annealing [105].

Further to elevated temperature and pre-annealing experiments, investigation into mechanical mechanisms resulting in potential wavelength drift of the embedded FBGs is required. This would further aid in ascertaining the origin of the change in the sensing properties. This experiment could contain purposefully manufactured 'poorly' embedded FBG's containing various known and expected failure mechanisms including oversized grooves, poor bonding of the fibre coating and the SS-316 coupon, and additionally misalignment of the FBG position within the groove profile, so that the FBG is non-centric and partially free of the bulk SS-316 coupon, see Figure 96. These samples will be investigated along with a normal embedded FBG, allowing for comparison of the different potential failure mechanisms for comparison against the slow degradation visualized in Figure 89- Figure 91. In order to reduce processing time required for multiple embedded samples, multiple test cases could be produced on a single printed coupon.

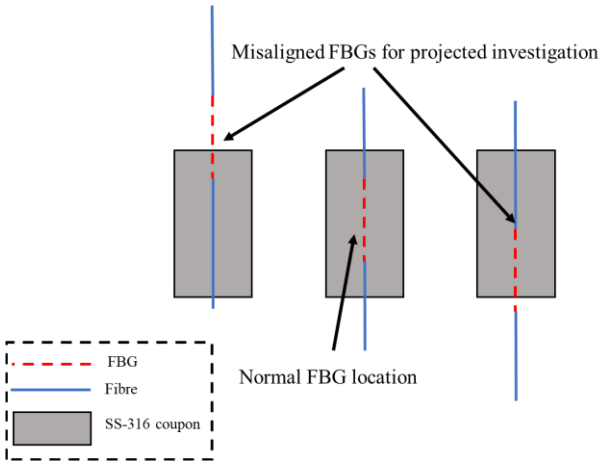

Figure 96 - Illustration of FBG locations within coupon for projected further experimentation.

These further investigations will help troubleshoot the origin of the wavelength drift in account of the temperature cycling process and whether it is due to any of the investigated failure mechanisms, or by potential annealing effects within the FBG, or a mixture of both effects.

5.4 Towards Extended Strain Cycling of Embedded FBG Sensor

There is interest in the ability to perform strain sensing in conjunction with temperature sensing using FBG embedded sensors. For example, if the FBG is not properly bonded into the groove, this could introduce discrepancies within strain readings due to potential fibre slippage within the groove and regions of the embedded fibre being under different modes of stress.

In order to accommodate for strain testing procedures, the sacrificial build plates must be manufactured into 'T-bone' structures, see Figure 97. These shapes are required for strain and tensile testing as they essentially control the failure region within the tested part, ensuring that it is aligned with the material under test, and outside the clamping regions. Shaping the plates into T-bones ensures that deformation is controlled to within the long, thin section of the part, denoted the gauge length. This becomes the region of interest for testing and provides the location for the rectangular printed coupon housing the FBGs, see Figure 97. When defining a tensile test specimen, the size and form of the measurand part must be taken into consideration for defining the size and dimension ratios of the T-bone plate, with the size of each feature governed by ASTM standards [106].

The parts would be tested by insertion into a tensile testing system and subjected to uniaxial loading until failure occurs, or a pre-determined limit is achieved. In order to provide successful strain testing procedures, coupons must be printed with strain isolated FBGs embedded in close proximity to a normal embedded FBG, see Figure 99. Embedding two sensors in parallel in this way allows for temperature and strain discrimination [107].

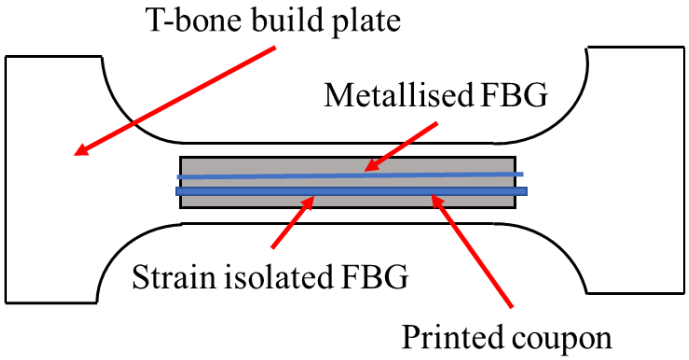

Figure 97 - Illustration of build plate and coupon design for strain testing purposes.

5.4.1 Testing Equipment

A typical system for strain testing procedures is the Instron low force electromechanical universal testing machine capable of performing tensile and compression mechanical tests, Figure 98. This system will allow for straining the embedded FBG both in parallel and perpendicular axes to the embedding profile to provide the full range of stresses expected within operation of the embedded FBG.

Figure 98 – Instron type 3400 electromechanical universal testing machine, [108].

5.4.2 Strain and Temperature Discrimination

FBGs are well known to be sensitive to both temperature and strain simultaneously [44, 107]. In many applications it is necessary to decouple these measurands, and therefore a means of temperature and strain discrimination is required. There are several routes to achieving this, but a common approach is to have two FBGs in close proximity to each other, with one strain isolated to be sensitive to temperature only. For ALM systems, this FBG pair could be achieved by embedding a normal metallised FBG within close proximity to a secondary FBG housed free-floating inside a metallised fibre capillary embedded into the structure, see Figure 99. Here, the capillary will isolate the secondary FBG from strain effects, allowing for measurement of the temperature independent of the strain, which in turn allows for temperature compensation of the strain.

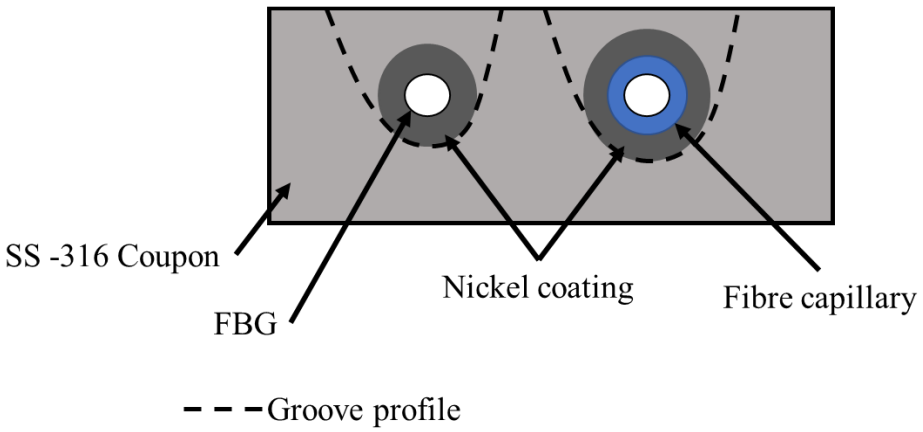

Figure 99 - Schematic illustration of cross section of coupon containing normal metallised FBG and strain isolated FBG housed free-floating inside metallised fibre capillary.

In order to isolate the secondary FBG from strain effects, it is inserted into a fiber capillary one end of the capillary attached to the fibre containing the FBG. Two mechanisms for achieving this attachment were investigated. The first involves using a fusion splicer to collapse the end of a 500µm diameter borosilicate capillary down to the fibre diameter (≈ 125µm) before metallisation, see Figure 100. Inspection of the success of the attachment is achieved by attaching a fibre connector to one end of the FBG and visualizing any light leakage from around the spliced region.

The second strain isolation method involves inserting the FBG inside a 1.5mm diameter SS-316 capillary, with the egress points of the fibre attached to the capillary by depositing small amounts of nickel around these regions using the electroplating set up defined in chapter 4, see Figure 101.

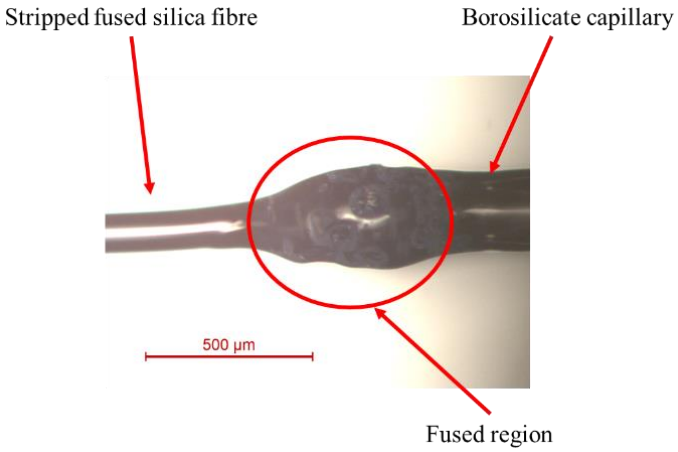

Figure 100 - Borosilicate capillary fused onto stripped optical fibre to achieve strain isolation of FBG. Image taken using a Leica 3D optical surface metrology system.

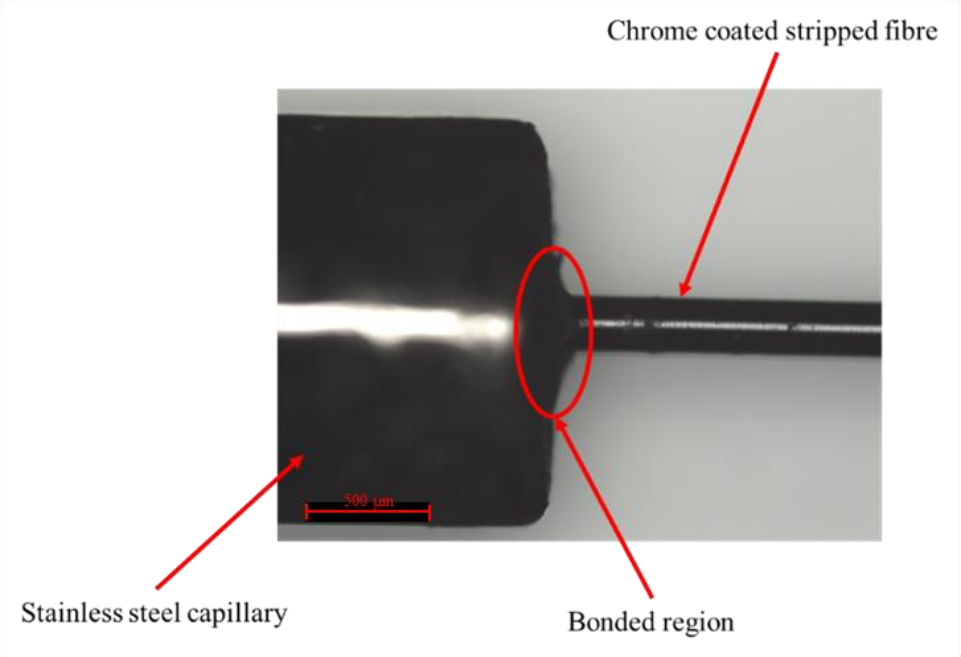

Figure 101 - Fibre inside stainless steel capillary, end point attached using nickel electroplating. Image taken using a Leica 3D optical surface metrology system.

Each proposed method retains benefits in regard to embedding strain isolated FBGs within SS-316 coupons. For instance, the large amount of metal surrounding the FBG within the second method would provide additional protection of the FBG against the heat input of the embedding process, negating the need for extended electroplating times while isolating the FBG from increased levels of strain. However, method one is deemed to most suitable for the project needs as previous analysis shows that an electroplated nickel coating of 300-500µm is sufficient for fibre heat protection purposes while allowing for a smaller form factor, which becomes increasingly important as the strain isolated sensors must be embedded close to the strain measuring FBG in order to realise isothermal operation.

5.5 Chapter Discussion

Chapter 5 follows the natural progression of the fibre embedding process, taking a metallised FBG and embedding it within a SS-316 coupon. The importance of the metallisation phase is clearly demonstrated by comparing in-situ interrogations of the fibre embedding with that of an uncoated (non-metallised) FBG. The result of this investigation is that the metallised FBG survived the embedding process with minimal change in its reflected spectra and sensing characteristics, which is in line with similar experiments conducted in literature, [12]. A slight wavelength shift is observed post-embedding which is expected due to the stressing of the fibre assembly inside the bulk SS-316 coupon.

By comparison, the intensity of the reflected spectra of the non-metallised FBG falls as the heat input by the lasing process induces damage to the fused silica fibre. This enforces the importance of shielding the FBG in a suitable nickel jacket prior to embedding using laser based manufacturing techniques, a virtue echoed by similar investigations in literature, [12, 18, 43, 50].

Survival of the FBG sensor during the embedding process only goes so far in determining the success of the embedding procedure, for the sensor must also retain suitable sensing characteristics for operation in terms of reliability, repeatability and accuracy of sensed stimuli. Therefore, after embedding, the embedded sensors were subjected to extended temperature cycling experiments. During these experiments, the wavelength was seen to drift over the course of the experiment. Wavelength drift of FBGs has been documented before, often being attributed to annealing effects within the grating itself, [42]. In account of this, FBGs are purposefully annealed in order to induce temperature stability, [105]. However, annealing effects are often documented for significantly higher temperatures than the embedded FBGs were subjected to within this project, with thermal stability achieved by annealing FBGs up to 400°C and wavelength drift associated with annealing effects occurring at temperatures between 750-1000°C, [42].

Thermally unstable gratings poses a potential cause of the wavelength shift exhibited by the embedded FBGs, requiring further investigation into FBG annealing effects in line with the projected experiments defined in Chapter 5 Section 4.4 [105].

The proposed future work will help understand this wavelength drift at such low temperatures compared to that seen within literature and additional processing steps such as pre-annealing of the FBG may need to be included into the fibre embedding process chain in order to ensure temperature stability of the embedded FBGs in operation.

The project timeframe, and implications of the covid pandemic, did not permit the strain cycling experiments to take place, however the prerequisite of this work were set up within the literature review and background phase of the research and also by the definition of methodologies for strain isolating FBGs. The suggested approach of housing FBGs strain free inside a glass capillary tube has been known to work for strain isolation purposes, [43, 109]. Further to this, it is easy to accommodate through the fibre embedding process chain with the larger size-scales featured by capillary tubes resulting in faster, less failure-prone metallisation processes. The only additional process required would be fusion splicing of the capillary tubes onto the optical fibres to promote strain isolation of the FBG inside.

Strain isolation by encapsulating within SS capillary tubes is poorly documented within literature, for it is only applicable for embedding within high melting point metals, and for use with the electroplating system defined in Chapter 4. Despite the novelty of this method, housing FBGs inside metallised glass capillary tubes is considered more appropriate for the project needs as it achieves the same effect for a significant reduction in sensor size due to the availability of narrow capillary tubing.

Much like strain cycling experiments, time did not permit for investigations into embedding distributed sensor networks. However, while the optical components would differ, the defined fibre embedding process chain would remain the same, for within this regard, embedding a single sensor is the same as multiple sensors within the same coupon. This process may become different for the incorporation of curved embedding, a novel feature that becomes possible due to the ductile nature of the nickel depositions, see Chapter 4. Therefore, projected future work within this chapter highlights potential steps for investigating this further, with specific relevance to coupon design and limitations of current embedding process and strain isolation mechanisms, which would require extensive investigation to fully understand the applicability of FBGs being used in non-linear embedding profiles.

5.6 Chapter Review & Conclusions

Sensor yield remains one of the most important features of the fibre embedding process. The survivability of optical fibres and optical sensors during the embedding process was demonstrated. For an optical fibre, this was verified by measuring light transmission, with optical losses measured around 18% for a 50mm length of embedded fibre. For the structure considered in this thesis, this is an acceptable loss as it would still allow for a detectable reflected peak from a FBG for sensing purposes. Subsequent embedding procedures for FBGs did not show the same level of loss, presumably because with the gained experience resulting in improved handling and processing parameters of the material layers above the FBG to help minimise losses.

Survivability for optical sensors was determined by the interrogation of FBGs in-situ during the embedding process. This aided an understanding of how the lasing procedure affects the FBG spectra and the difference in reflected peaks before, during, and after embedding. The positive Bragg wavelength shift highlights how the grating is now being stressed by the bulk SS-316 material, going someway to indicate successful bonding of the fibre into the coupon groove.

The comparison of embedding unmetallised and metallised FBGs illustrates the importance of the protective metallic jacket in protecting the FBG during the embedding process. The intensity of the reflected peak of the uncoated FBG dropped off significantly during the embedding procedure, in severe detriment to its sensing capabilities. This was not observed to be an issue with the metallised FBG, which retained a suitable reflected peak for conducting operational sensing.

While survivability of the embedding sensor is major figure of merit, performance of the embedded FBG during extended and elevated temperature cycles is as important for determining the overall success of the fibre embedding process. The embedded FBGs were shown to survive repeated temperature cycling experiments, illustrating the reliability and repeatability of their sensing characteristics. In turn, this allowed for the grating sensitivity to be determined, which is important for correlating temperature from shifts in the Bragg wavelength during operation.

Experimental project time did not permit for strain cycling experimentation to be conducted. However, methods for achieving strain isolation of embedded FBGs was demonstrated, including housing FBGs free-floating in both metallised glass and SS capillaries. The metallised glass capillary method remains the most applicable for the project needs, due to the potential for reduced form-factor of the embedded sensor assembly. This becomes increasingly prevalent as multiple FBGs must be embedded side by side to achieve temperature and strain discrimination.

Additional work required in order to complete the investigations highlighted within Chapter 5 were illustrated, with time constraints inhibiting their inclusion within the experimental phase of the project. This additional work will aid in understanding of the wavelength drift seen during the temperature cycling experiments and help discern its origin at such low temperatures compared to wavelength drifts seen within literature [42]. A byproduct of these investigations is the analysis of the effects of high temperature annealing on the temperature stability of FBGs. Additional future work will be required to understand the applicability of embedding curved FBGs within coupons, that retain their sensing capabilities and allow for temperature and strain discrimination.

Chapter 6 - Induction Brazing

This chapter details the theoretical analysis in order to produce design specifications for an induction brazing system using a 1.75kW induction heating kit for the purposes of brazing Ni coated fibres into SS-316 coupons. It then follows initial testing of the system to ascertain its applicability for the project needs and relevant modifications that would be required for induction brazing using austenitic stainless steels, such as SS-316, required for the embedding material in account of their corrosion resistance and applicability for applications involving electromagnetic fields.

6.1 Introduction – Incorporating Induction Brazing into Embedding Process

Following from the review into incorporating brazing into the fibre embedding procedure, it was decided that an induction brazing system could be inserted into the embedding process sequence. Therefore, an induction brazing system was developed capable of achieving suitable operational temperatures and process atmospheres in order to conduct a feasibility study on the inclusion of induction brazing into the embedding process.

6.1.1 Design Specifications

The design of the induction brazing system is constrained by the use of a 1.75kW draper tools induction power supply with operational parameters provided in Table 12, which was deemed suitable for a feasibility study into induction brazing. The sample holder must be capable of providing an inert gas atmosphere to reduce oxidation and broaden the applicable brazing alloys that can be used. Furthermore, the system must provide localised heating of the metal parts retaining maximum dimensions of 80×20×10mm (length × breadth × height) to suitable temperatures for the use of various brazing filler alloys (600-900°C). The entire process must be conducted within the safety recommendations of the power supply, and measures must be in place in order to conduct brazing experiments safely within a shared lab space. These include limiting the heating time of the induction coils, isolation of the heated components and suitable ventilation.

6.1.2 Induction Heating Principles

In its most basic form, the coil of an induction heating system can be thought of as the ‘primary windings’ of a transformer and the workpiece, i.e. the metal to be heated, can be thought of as the transformer secondary ‘winding’.

A RF power source is typically used to apply a high frequency alternating electrical current within the transformer primary, creating a rapidly alternating magnetic field. By Faraday's law of induction, eddy currents will be induced in the secondary where there is good magnetic coupling between the heating coil and the metal sample [110].

Two mechanisms contribute to the heating process within an induction heating system, eddy current and hysteresis losses. The induced eddy currents flow against the resistivity of the heated part, allowing for localised heating. Hysteresis losses occur in ferromagnetic materials such as steel and Ni. As magnetic parts are heated by induction, the alternating magnetic flux field causes the magnetic dipoles of the material to oscillate due to the changing polar orientation of the magnetic poles with every cycle. Losses in this process result in additional heating of the material [110]. In most cases, heat induced by hysteresis can be ignored as it only occurs in magnetic materials below their Curie temperature (temperature at which magnetic materials experience a significant change in their magnetic properties) and is typically less than heating induced by the eddy current resistance losses. Therefore, for most induction heating processes, it can be assumed that the heat is induced when an alternating eddy current is induced into a workpiece.

6.1.3 Skin Effect and Depth of Penetration

The depth of heating achievable by induction heating processes depends on the frequency of the AC field (ω), electrical resistivity (ρ_R) and relative magnetic permeability of the workpiece (μ), see equation (17). This equation defines the depth in which 86% of the heating due to resistance against the current flow occurs (or the magnitude drops to 1/e = (0.368) of its surface value). This value, termed the penetration depth, can be seen as the minimum depth of heating that a given frequency will produce at a given power and workpiece temperature [110]. It is therefore a useful correlation for ensuring sufficient heat is inducted within the desired locations within the workpiece. It can be seen that the depth of penetration can be increased or decreased by altering the frequency or temperature of the material.

$$\delta = \sqrt{\frac{2\rho_R}{\mu\omega}} \tag{17}$$

6.1.4 Theoretical Calculations

The induction heating system investigated is the Draper Expert Induction heating tool, part number IHT-15. The specifications of this system are outlined in Table 12. The objective of the preliminary calculations is to ensure that the induction heating system provided is viable for use in regard to induction brazing procedures.

Rated voltage	230V
Load factor	50% at 1.5kVA, 100% at 1kVA
Input current (max)	7.5A
Power (max)	1.75kW
Maximum permissible heating time	120s

Table 12 - Draper Expert induction heating tool specifications.

The main limiting parameters in regard to the induction heating process are the maximum power rating of 1.75kW and the maximum heating cycle time of two minutes, requiring the system to cool before initiating again, negating the possibility of sequential heating cycles due to part cooling. The calculation will be based on worst case scenario conditions, which in this case, relates to the materials to be brazed and the brazing temperature they require. Therefore, the calculation will be based on brazing using a Ni based filler alloy, due to it being a high temperature requiring process temperatures in excess of 900℃.

The calculation follows the process outlined by [111]. The mass of metal to be heated is estimated in order for the required power input to be determined via equation (18) where, m is the mass of material to be heated (kg), c is the specific heat (J/kgK), ΔT is the desired temperature change (℃) and t is the heating cycle time (s). A recommended safety margin of 10% was then be added to the determined value to accommodate for radiation losses during the heating process [111].

$$P_t = \frac{mc\Delta T}{t} \tag{18}$$

A temperature change of 900℃ is chosen in regard to the brazing of nickel-based filler alloys when initiating the cycle at room temperature as this was deemed to be the highest temperature change required of the system. The heating cycle time is limited by the recommended maximum permissible time from the manufacturer (120s).

6.1.4.1 Specific Heat Capacity of Stainless-Steel type 316 and Nickel

The temperature dependent specific heat of SS-316 and Ni were estimated using the empirical equations defined in [112]. The author's report inaccuracies in their findings at high temperatures (>800°C), when compared to other sources, but the empirical equations were used to extrapolate data beyond this for the purpose of the calculation.

Equation (19) was used to estimate the specific heat of SS-316 for a range of temperatures ($100°C - 1000°C$) and the resulting smoothed curve is plotted in Figure 102.

$$c = 0.12754 + 3.024(10^{-5})T - \frac{4.81}{(T + 273.15)} \tag{19}$$

Where, in this case, the temperature (T) is input in °C. A similar method was followed for determining the specific heat of nickel and the results are also plotted in Figure 102. However, it is noted by the authors that the uncertainties associated with the smoothed curve increase significantly beyond 600°C in account of insufficient experimental data points beyond this value [112], which could explain the kink in Figure 102 which features at around this temperature. The estimated values of the specific heat are, however, sufficient for use in estimating the required power of the induction heating system.

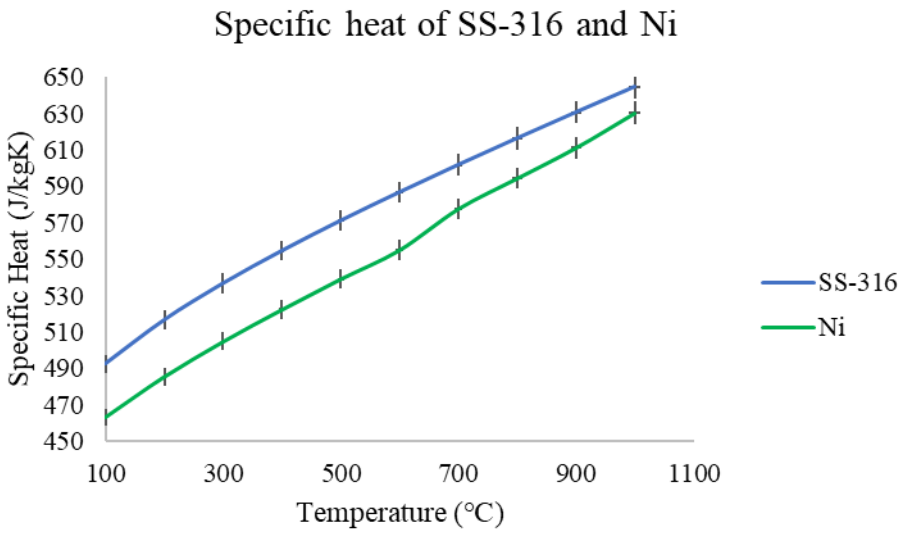

Figure 102 - Specific heat of stainless-steel type 316 and nickel, data taken from [112].

6.1.4.2 Power Input

The specific heat was determined at 100°C intervals and the contribution towards the power was determined for each of these temperature increments extending the full range, with the only variable being the corresponding specific heat value for its respective temperature range. For simplicity, the specific heat was recalculated at 100°C intervals, with the value used for the 100°C interval up to this point to provide a worst-case scenario. This allowed for an estimation of the required power while considering the temperature dependence of the specific heat.

The total power required for various heating cycle times was determined, Figure 103. Although an increasing workpiece length, and therefore heated volume, was investigated, the maximum length of heating achievable by the induction coil is limited to 100mm. For larger workpieces, either a secondary coil and power supply is required or a coil with a larger length will have to be manufactured.

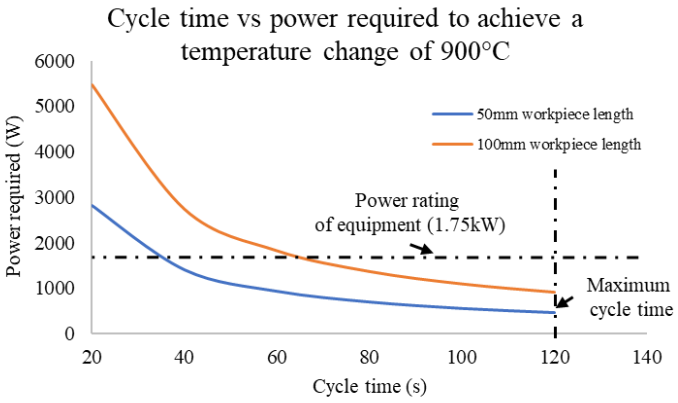

Figure 103 - Cycle time vs power required to heat 50mm and 100mm workpiece sizes for a change in temperature of 900°C.

6.1.4.3 Concluding remarks

The results show the applicable heating times for maintaining the required power below the maximum value of 1.75kW. As is expected, as the volume of the workpiece is increased, the required power increases, implying that modifications to the induction heating system would be required for larger part geometries.

Overall, the simple analysis conducted within this section illustrates the feasibility of using the Draper induction heating tool for induction brazing procedures and is viable for use for a broad range of filler alloys. However, for some of these alloys, such as copper and nickel alloy, an inert gas atmosphere will have to be incorporated into the system for the brazing procedure to be conducted successfully.

6.2 Induction brazing system design

Based upon this preliminary design calculations, an induction brazing system was designed and assembled for initial testing, see Figure 104.

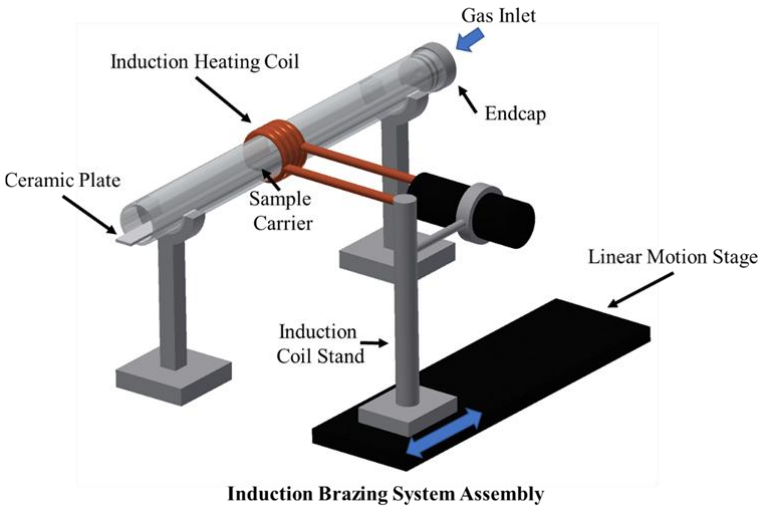

Figure 104 - CAD assembly of the induction brazing system design.

The design in Figure 104 is shown as a lab setup shown in Figure 105. An induction coil was manufactured by bending hollow copper tubing to the outer diameter of a borosilicate pipe with enough coils to cover a typical embedded sample (≈80mm in length). The internal diameter of the coil was chosen in order to provide interference free movement of the coil along the length of the pipe, while keeping it to a minimum in order to provide more efficient induction heating of the substrates located inside. The copper coil is housed inside a heat resistant shield and connected to a draper tools 1.75kW induction heating tool unit.

Aluminium end caps were manufactured to press fit onto the ends of the borosilicate tube with rubber O-rings providing a seal to limit gas leakage from the system. Gas inlets were designed onto these endcaps to allow argon to be fed into the system to provide an inert atmosphere in which to conduct the brazing process. The induction coil is mounted onto a linear translational stage to promote uniform heating and the entire system is surrounded in protective insulation with an extraction hood positioned to extract fumes during the heating process. The system is designed with the ability to use different brazing alloys. Although, for safety reasons, this was in practice limited to low temperature, silver-based brazing alloys which require a brazing temperature upwards of 600°C.

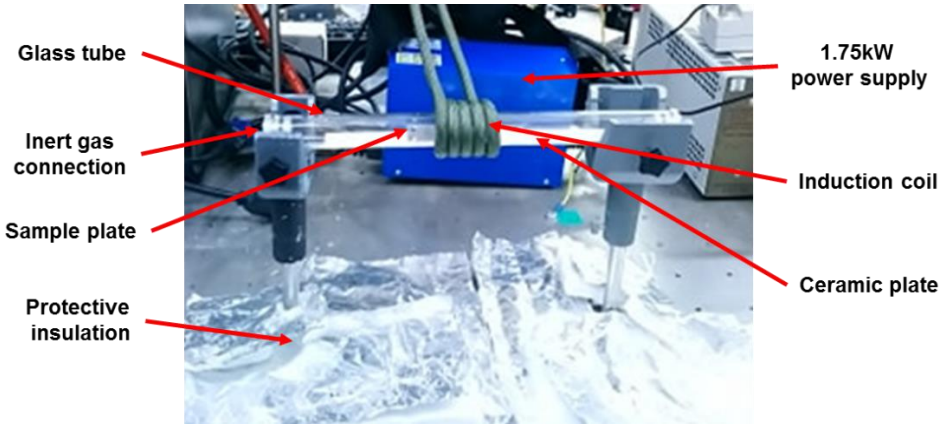

Figure 105 - Induction brazing set up.

6.3 Induction Brazing of Stainless Steels

While the analysis provides a base point for investigation, practical experiments are required to ensure the viability of the induction brazing system for bonding a nickel jacketed fibre into a SS-316 coupon.

An experiment was conducted whereby samples of mild steel and SS-316 were heated by the induction brazing system up to a maximum heating time of 120s with their temperature taken at predefined increments. Temperature determination was provided by an IR temperature probe capable of measuring up to 600°C, as temperatures beyond this value are more than suitable for brazing using silver-based alloys. The cut off heating time of 120s correlates to the maximum permissible heating time of the power supply. Sample size was maintained consistent with expected embedded samples (50mm×15mm×10mm) in order to provide a realistic result in terms of the feasibility of induction heating of mild steel and SS-316 substrates.

The results of the experiment are highlighted in Figure 106. Mild steel is seen to exhibit a rate of heating similar to that of the theoretical calculations, reaching temperatures beyond 600°C within 15s heating time. SS-316, however, only reached around 40°C within the same timeframe and did not exceed 200°C within the maximum permissible heating time. This is in account of the power limitations of the setup and the unique magnetic and induction properties of type 316 stainless steels, which was not considered within the theoretical analysis.

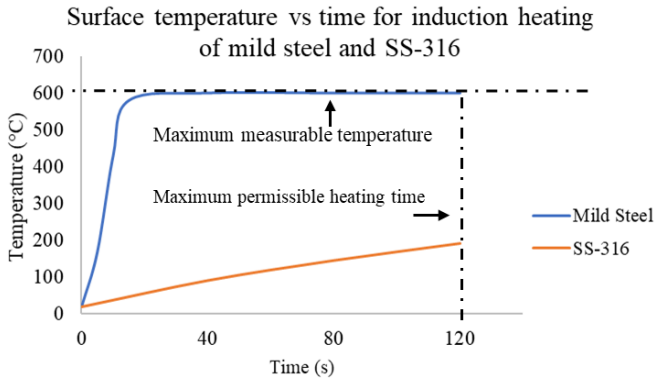

Figure 106 - Surface temperature vs heating time for induction heating of mild steel and SS-316.

The heating effect of mild steel is vastly superior to SS-316 for the same induction heating conditions in account of the respective material's magnetic properties, notably, the drastic difference in relative permeability (around 2000 for ferromagnetic material such as mild steel, and around 1 for austenitic stainless steels such as SS-316) [113]. This illustrates the difficulty in induction heating of austenitic stainless steels, such as SS-316, when compared to other variants of SS that are ferromagnetic. As a result of this, the applicability of this induction brazing system with SS-316 samples was significantly reduced.

6.4 Chapter Discussion

The theoretical analysis of induction brazing stainless steels was conducted using a model that assumed the brazing of ferromagnetic materials, therefore did not consider the magnetic properties of austenitic stainless steels. Ultimately this has significant implications as seen in Figure 106, there is a drastically different response to induction heating of mild steel and SS-316, under the same heating conditions.

The drastic difference in performance can be attributed to the respective material's magnetic properties, specifically considering their response to a magnetic field. Austenitic stainless steels such as SS-316 are classified as paramagnetic with a relative permeability of 1.002-1.005 [113]. This attribute allows them to be used within applications requiring non-magnetic materials and electromagnetic interference. However, it significantly reduces their applicability for induction heating procedures. By comparison, ferritic stainless steels have a relative permeability approaching 2000, which explains materials such as mild steel's vastly superior response to the induction heating process [113]. This has implications for the application of induction heating SS-316.

In order to suitably conduct induction brazing procedures using SS-316, a significantly higher power rated power supply and suitable work environment would be required. Despite this, induction brazing is still deemed a worthwhile addition to the embedding process in order to aid bonding of the underside of the metallised fibre into the groove. This is in account of the significant benefits in terms of fast, localised heating and relative low cost compared to other applicable brazing techniques [69], [73]. This does, however, require operational capabilities outside of the abilities of the draper tools 1.75kW induction heating system available to the project.

6.5 Chapter Review & Conclusions

While time was insufficient to fully develop the induction brazing system and incorporate the process into the fibre embedding process, the work conducted in this chapter sets the foundations for future investigations. The review into dissimilar metal joining processes allowed for determination of the most suitable metal joining technique for incorporating into the fibre embedding process, when considering process needs and viability.

This review led to the development of an induction brazing system and preliminary investigation into incorporating induction brazing into the fibre embedding process. It was found that the current setup (designed around a 1.75kW induction heating kit) did not retain suitable power for induction brazing of austenitic stainless steels such as SS-316. Despite this, induction brazing still retains a desirable addition to the embedding process due to its fast, localised heating, and is still recommended to achieve full bonding of the metallised fibre into the groove.

Chapter 7 – Discussion, Conclusion and Future Work

Embedding optical sensors within high melting point metals allows for condition monitoring of a part/process during operation, which can be implemented into failure prevention schemes. Therefore, this thesis aims to quantify a process for embedding optical fibres within SS-316 coupons manufactured using ALM.

7.1 Thesis Discussion

Each stage of the embedding process was investigated, allowing for system development and parameter optimisation for fibre embedding procedures, leading to the successful definition of a reliable fibre embedding process for embedding FBG sensors within SS-316 coupons.

A fibre embedding process was developed based on an extensive review of the current state of the art of optical sensor embedding within high melting point metals. This involved the design and manufacture of a bespoke SLM system suited to fibre embedding procedures. This was a critical step because it allowed for modification of the build parameters as, and when, necessary, which was unavailable via commercial systems. The system was testing using a fibre delivered laser and high-speed scan head to embed optical fibres containing FBGs within SS-316 coupons. To aid flexibility, the system was designed to be portable such that it could be used with other laser and scan head set-ups with ease, without detriment to its operational viability. This opens the prospect of future work using a higher power laser system if such a system was deemed necessary and become available.

A further benefit of using a custom system is that each stage of the build was adaptable and modifiable depending on the process needs ensured that the best possible layer resolution was achieved while ensuring sensor survivability during the embedding process. The ability to interrupt the build process was needed to install the fibre partway through the build.

While embedding optical sensors within high melting point metals is not new, [12, 18], this thesis developed a bespoke system to allow for all stages of the process to be considered experimentally. This allowed for full investigation into each stage of the embedding process and the required process parameters, so that a reliable and repeatable fibre embedding process could be defined that opens up the possibilities of mass manufacture of instrumented metallic components.

Extensive calibration of the SLM system was carried out, justifying the best build parameters for achieving dense parts with low surface roughness within the operational limitations of using a maximum mean laser power and scan velocity of 100W and 400mm/s respectively. This required the incorporation of laser polishing procedures between each build layer and extensive investigations into other build parameters including hatch spacing, layer thickness and pulse duration, see Chapter 3.

The successful mitigation of detrimental part features that occur during the SLM process such as balling, trenches and elevated edges was demonstrated, ensuring the best possible part density and surface finish using the self-made SLM system. To improve the system performance further would require a laser power and scanning velocity far outside the boundaries of the equipment available to the project [88, 89], however, the portable design of the system means this would be possible to consider in follow-up work. In this work, the ability to conduct laser polishing procedures during the SLM build process allowed for compensation of the hardware limitations of the system in achieving printed layers with good surface quality and low porosity.

The requirement of a fibre metallisation stage within the embedding procedure is a known requirement for embedding processes, [12, 18, 43, 50]. Each stage of this process was investigated in full, and resulted in the development of a custom in-house electroplating system, specifically designed for plating Ni onto chrome-coated fibres. This additionally allowed for investigation into the process requirements for achieving ductile, shapable, uniform nickel depositions onto chrome-coated optical fibres containing FBGs for use in more complex embedding geometries.

Dissimilar metal joining poses an interesting addition to the fibre embedding process chain. A review into applicable technologies was conducted, after which induction brazing was deemed the most suitable for joining nickel coated fibre into SS-316 grooves. A system was designed that would allow for brazing investigations to be conducted. If a higher wattage and frequency power supply was available, these investigations could extend to the use of austenitic stainless steels such as SS-316.

Repeated temperature cycling of embedded FBGs was conducted, illustrating the survivability of the embedded sensor when subjected to high temperatures. The wavelength shift that occurred during the temperature cycling reduced the repeatability of the sensor performance, however, it was possible to define a grating sensitivity which correlated temperature profiles that matched the experimentally measured values. This work highlights that further investigations into this wavelength drift are necessary in order to pinpoint whether they occur due to grating annealing effects or other mechanisms which could include mechanical creep or slippage. The data presented suggests that the effect is reducing with repeated cycling, and that over an extended annealing time a repeatable response may be established. If this is the case, annealing of the embedded FBG may change from being a detriment to sensor operation, to becoming an important additional step in the fibre embedding process, as stable gratings perform better within operation at elevated temperatures ($> 400°C$) [109].

Initial concepts for embedding strain isolated FBGs was discussed and demonstrated, with time constraints limiting strain cycling of the embedded FBGs. The proposed method for strain isolation, by housing a FBG free-floating inside a metallised glass capillary, has the benefit of being easily incorporated into the fibre embedding process chain, with only minor adjustments to process parameters within the metallisation phase required in order to do so effectively.

7.2 Future Work

The study presented in this thesis develops a bespoke in-house embedding process. However, a number of areas have been highlighted as being suitable for follow on research.

7.2.1 Development of Induction Brazing System

Initial investigations into the use of induction brazing are discussed in Chapter 6. This work sets the foundations for further investigations for adopting this metal joining process into the fibre embedding process chain, highlighting the current hardware, safety and spatial limitations surrounding its use.

While there was only limited success in the experimental investigations and theoretical analysis, the usefulness of the addition of brazing is illustrated, although modifications would be required (such as higher power and frequency power supply, larger induction coil) for larger part sizes. If this methodology was taken forward, it would require thorough investigation with suitable equipment. Induction brazing remains the most applicable in terms of balancing functionality and cost.

If the inclusion of metal joining processes was to be investigated in full, it is recommended to additionally develop the means to conduct vacuum brazing, as the analysis carried out in Chapter 6 highlights this as another beneficial brazing method for the project needs. Vacuum brazing would negate the complications of induction brazing austenitic stainless steels like SS-316 and increase resistance to oxidation and corrosion during the brazing process. However, this would require significant capital expenditure to develop a vacuum furnace with high levels of temperature control, and a dual pump process to achieve vacuum, using a rotary pump to initiate the process and a turbomolecular pump to achieve the required levels of vacuum. Therefore, developing a high-power induction brazing system remains the most suitable for further investigation.

7.2.2 SLM system modifications

During operation of the SLM system, it became evident that certain detrimental features, such as balling and trenches, were seen to occur. Despite best efforts to limit these occurrences using laser and build parameters, in order to mitigate them further, modifications to the mechanical design of the SLM system would be required.

The process operates within an inert atmosphere. However, during the lasing process, molten powder material can erupt from the melt pool to fall into other regions of the build area, causing raised surface features which is in detriment to the surface finish of the part and can interfere with the powder deposition process within the SLM build. Process parameters were modified to limit the occurrence of such phenomena. However, this can only be done while maintaining suitable build parameters for successful melting of the SS-316 powder and fully melting material layers. Therefore, it cannot be designed out completely using build parameters alone.

If further time was given to the SLM design, the build chamber would be modified to allow for a narrow yet wide argon gas stream directed perpendicular to the long axis of the system, encompassing the build area. This gas stream would be maintained within close proximity to the build layer and without diffusing into the Z-plane and be directed into a similar dimensioned outlet at the opposing side of the gas chamber. The purpose of this gas stream is to catch molten powder particles and plasma erupted from the lasing process and directed them away from the build area so that they do not interfere with the build process and induce detrimental part features to occur. A schematic illustration of such a design is illustrated in Figure 107.

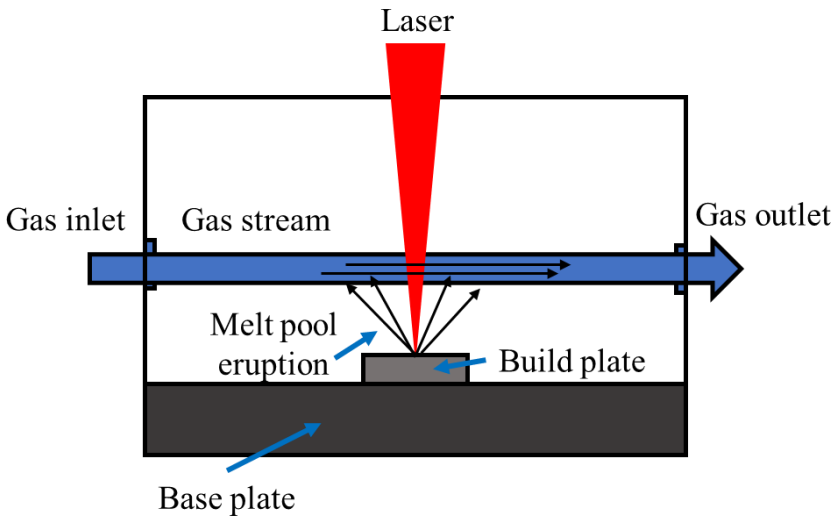

Figure 107 - Schematic illustration of SLM design modification relating to gas stream to divert molten particulates away from build area.

7.2.3 Coupon groove profiles

During the embedding procedure, the thermal stresses of the lasing process work to push the fibre from the groove, as discussed in Section 5.1 While induction brazing poses a possible solution to this problem, additional features are proposed for the groove design itself to mitigate this occurrence. The addition of staggered overhangs into the groove profile would help maintain the fibre inside the groove boundary, see Figure 108, so long as the metallised fibre is ductile enough to be bent around these features prior to the lasing process.

More than other embedding techniques, the SLM process caters for overhanging structures as the un-melted powder behaves as a support material for the formation of these structures. While this method helps keep the fibre in place during the embedding process, it does not resolve the issue of bonding the underside of the metallised fibre into the groove, therefore, induction brazing into the slot still holds promise to provide full bonding. However, the addition of the staggered overhangs is expected to reduce the effect of thermal stresses within this bonded region, adding an additional layer of security into the embedding process for achieving fully bonded parts and can be seen as a cost-effective approach for improving fibre bonding into the coupon groove.

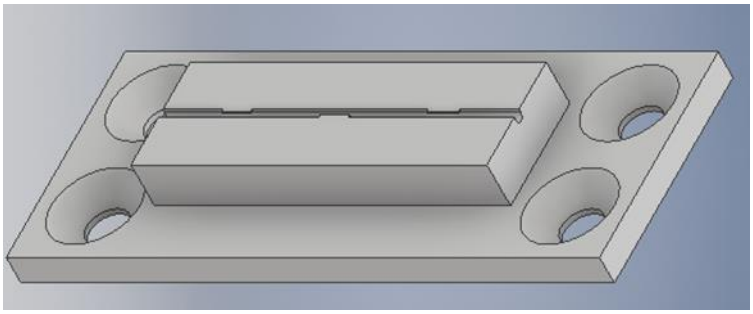

Figure 108 - Groove design with staggered overhanging features to keep fibre inside the groove during the embedding process.

7.2.4 Non-linear embedding profiles

The ductility of the deposited nickel coatings, as demonstrated in section 4.5, allows for the possibility of embedding FBG sensors in shaped groove profiles. This becomes significant if there are components or features that cannot be removed from the embedding profile, such as screws or bolts that require the fibre to be routed around them.

The ability to embed FBG sensors around these features allows for sensor functionality within constrained embedding spaces and can reduce the form factor of the embedded sensor network. Sample illustrations of such embedding profiles are given in Figure 109. The method for producing metallised coatings within curved profiles is highlighted in Section 4.5.

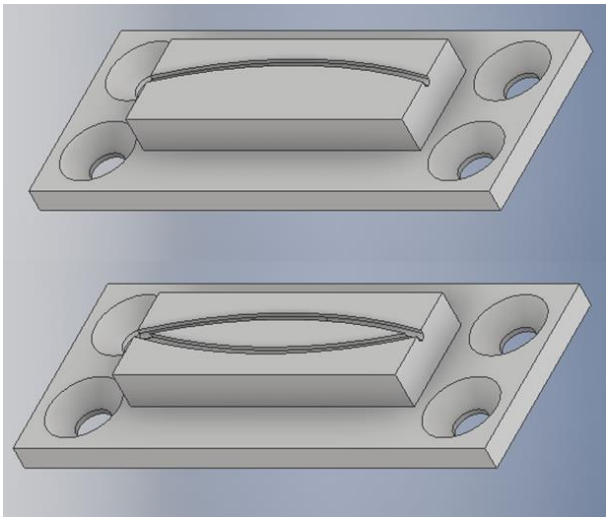

Figure 109 - Examples of potential embedding profiles made feasible due to the ductility of deposited nickel coatings.

Embedding curved FBGs may incur changes in the reflected spectra due to the possibility of different strain across the fibre and birefringence effects. So long as these stresses remain time invariant, they can be accounted for within the sensor calibration. As the sensor is effectively pre-strained, any significant temperature differential will result in relaxation or constriction of the fibre, which overtime may induce issues within the bonding of the metallised fibre in the groove. Furthermore, difficulties will arise in determining an accurate correlation of strain measurements. This is in account of increased levels of thermal stresses, promoting further difficulties in providing temperature and strain discrimination. Not only this, but additional methods for strain isolation must be investigated as the current proposed method of housing an FBG free-floating inside a metallised capillary will no longer be applicable due to the inherent brittleness of glass capillary tubes.

7.2.5 Distributed sensor embedding

Time did not permit for investigations into embedding distributed sensor networks. However, while the optical components would differ, the defined fibre embedding process would remain the same, for within this regard, embedding a single sensor is the same as multiple sensors within the same coupon.

The embedding process may become different for the incorporation of curved embedding, a novel feature that becomes possible due to the ductile nature of the nickel depositions, see chapter 4. Therefore, projected future work within this chapter highlights potential steps for investigating this further, with specific relevance to coupon design and limitations of current embedding process and strain isolation mechanisms, which would require extensive investigation to fully understand the applicability of FBGs being used in non-linear embedding profiles.

Conventional embedded sensors allow for point sensing within a localised region of a part. The accuracy (or relevance of a measurement) decreases as the distance between the sensor and the area of interest increases. A true distributed sensing scheme offers the potential to provide a measure of sensed parameters across the whole part's surface and even internal volume, depending on makeup and orientation of embedded sensors. If the fibre is routed correctly, this could offer meaningful measurement of the component.

Distributed sensing networks opens up the possibility for sensing different parameters at the same time, within the same part, using the same optical source. In this context, optical sensors such as FBGs cater well for the development of distributed sensing networks.

7.2.5.1 Single Sensor Branches

The most basic form of distributed sensing using FBGs is to install multiple sensors in series providing a line of sensing points across a part's surface, see Figure 110. This offers the potential for better spatial resolution for parameter determination than single point-based sensors and allows for strain-isolated FBGs to be located on the same fibre as normal embedded FBGs.

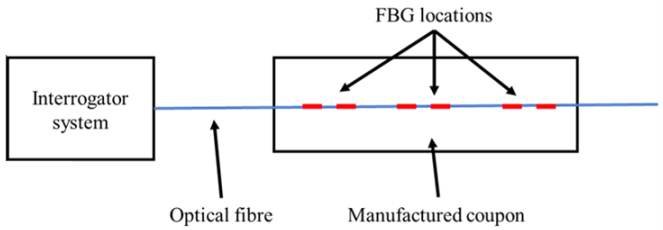

Figure 110 - Schematic illustration of line-based distributed sensing using multiple FBGs stitched together in series.

7.2.5.2 Multiplexed Sensor Network

The incorporation of wavelength division multiplexers (WDM) opens up the possibilities of true distributed sensing by allowing for the production of sensor network "trees" made up of multiple line sensing "branches", with each branch being capable of sensing a different parameter under its own unique wavelength range. An illustrative example of such a network is provided in Figure 111.

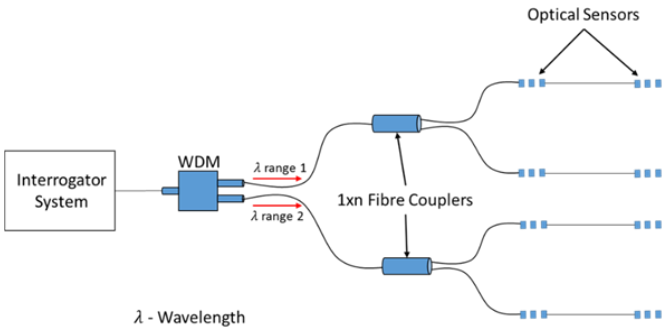

Figure 111 - Illustration of sensing network using wavelength division multiplexer and multiple branches of optical sensors in series to produce distributed sensing capabilities.

The fundamental embedding process remains the same as single point-based sensors, however the number of embedding profiles and the scale of the coupons must be increased to cater for the increased amount of embedded sensor trees. Investigations could include embedding the fibre coupler as well as the sensor networks to reduce the form factor of the sensor system, and the implications this would have on the embedding process and strain isolation of sensors.

It is possible to retain all sensors on a single length of fibre, so long as there is space for looping the excess fibre around the system. However, a branched approach is preferred to reduce clutter in complex systems and for easy changing out of any sensors that fail in operation. As each branch of the sensing tree is interrogated using a unique wavelength range, it is possible to provide temperature, strain and pressure measurements from a single optical source, significantly reducing the form factor when compared to individual, conventional sensors providing the same information. Further to this, the sensing tree can be used to determine a single sensed parameter over a much larger area of the part, providing accurate distributed sensing across an entire part's volumetric body.

7.3 Conclusion

The project work successfully defined a repeatable and reliable fibre embedding process chain for the purposes of embedding FBGs within SS-316 coupons. Each stage of the process was investigated, allowing for optimal processing parameters to be determined and for detrimental features to be investigated and accounted for where possible. These types of investigations were only possible due to the use of custom systems for the fibre embedding process that were designed specifically to allow for full access and modifiability of the embedding process at each stage, traits inapplicable for commercial of-the-shelf systems or outsourcing certain parts of the process such as SLM, metallisation and intermediary metal joining.

As the designed systems were continuously adapted and modified over the course of the project, their operational viability for fibre embedding procedures was developed, and the functionality of these systems can be further refined. This only becomes feasible now that the embedding process is defined in detail and better understood as a whole.

The work of this thesis aided defining process parameters suitable for repeatable and reliable embedding of FBG sensors inside SS-316 coupons. 5µm thick Cr layers are deposited onto lengths of stripped optical fibres containing FBGs using the RF sputter deposition system (RF power 100W, deposition time 30mins, processing pressure 4×10^{-4}mBar). This is followed by a ≥300 µm Ni coating using the developed Ni plating system (current density 2-7 A/dm^2, voltage 30V max, plating time ≥16hrs). The SLM build parameters for building the SS-316 coupon and the modified build parameters for the embedding process are highlighted in Table 13.

Parameter	SS-316 coupon	Embedding layer(s)
Laser Power	100W	90W
Scanning velocity	300mm/s	300mm/s
Layer thickness	100µm	100µm
Hatch spacing	60µm	100µm
Hatch orientation	Rotate by 45-90° at every new print layer	Parallel to fibre profile
Pulse Duration	200µs	200µs

Table 13 - SLM parameters for printing the SS-316 coupon and the parameters during the embedding process.

The repeatability of the embedding process is demonstrated, and testing conducted to illustrate sensor survivability and determine a grating sensitivity. The experimental studies surrounding the definition of this embedding process sets the foundations for future investigations into the field of optical sensor embedding within high melting point metallic structures.

References

[1] X. Li, “Embedded Fiber Bragg Grating Sensors in Polymer Structures Fabricated by Layered Manufacturing,” *Journal of Manufacturing Processes ,* vol. 5, no. 1, pp. 78-86, 2003.

[2] A. H. Stefan Sandlin, “Embedding Optical Fibers in Metal Alloys,” *IEEE Instrumentation & Measurement Magazine,* vol. 6, no. 2, pp. 31-36, 2003.

[3] X. Li, “Embedded Sensors in Layered Manufacturing,” Doctor of Philosophy PhD, Mechanical Enginnering, Stanford, 2001.

[4] M. G. Zubel, K. Sugden and J. W. D, “Embedding silica and polymer fibre Bragg gratings (FBG) in plastic 3D-printed sensing patches,” in *International society for optics and photonics*.

[5] D. W. Olson, S. F. Wolf and J. M. Hook, “The Tacoma Narrows Bridge Collapse,” *Physics Today,* vol. 68, pp. 64-65, 2015.

[6] Hazardous Installations Directorate (HID) Specialised Industries Division, “Investigation of the Explosion at Linfield Street Dundee 22nd of October 2000,” Health and Safety Executive, 2003.

[7] A. Goldsworthy, “The Roman Navy,” in *The Complete Roman Army*, London, Thames & Hudson, 2007, pp. 34-43.

[8] Y. Baudoin and M. K. Habib, Using Robots in Hazardous Environments - Landmine Detection, De-Mining and Other Applications, Elsevier Science, 2010.

[9] I. N. Qader, “A Review of Smart Materials: Researches and Applications,” *El-Cezerî Journal of Science and Engineering,* vol. 6, no. 3, pp. 755-788, 2019.

[10] J. Delsing, J. Ekman and J. Johansson, “Susceptibility of sensor networks to intentional electromagnetic interference,” in *17th international symposium on electromagnetic compatability* , \zurich, 2006.

[11] P. Antunes, “Mechanical Properties of Optical Fibres,” *Selected topics on Optical Fiber Technology,* pp. 537-550.

[12] D. Havermann, “Study on Fibre Optic Sensors Embedded into Metallic Structures by Selective Laser Melting - A dissertation submitted for the degree of Doctor of Philosophy,” 2015.

[13] M. B. Rao, M. R. Bhat and C. R. L. Murphy, “Structural Health Monitoring (SHM) Using Strain Gauges, PVDF Film and Fiber Bragg Grating (FBG) Sensors: A Comparative Study,” in *National Seminar on Non-Destructive Evaluation*, Hyderabad, 2016.

[14] A. Whelan and J. P. Goff, “Polymers for elevated temperature use,” in *Developments in Plastics Technology - 4*, Dordrecht, Springer, 1989, pp. 167-199.

[15] N. V. K. Prasad, K. V. Prasad, S. Ramesh and S. V. Phanidhar, “Ceramic sensors: a mini review of their applications,” *Fronteirs in Materials,* 2020.

[16] M. A. El-Sherif and J. Radhakrishnan, “Advanced Composites with Embedded Fiber Optic Sensors for Smart Applications,” *Journal of reinforced plastics and composites,* vol. 16, no. 2, 1997.

[17] F. Nürnberg, B. Kuehn and K. Rollmann, “Metrology of fused silica,” in *Laser-Induced Damage in Optical Materials*, Boulder, 2016.

[18] J. Mathew, C. Hauser, P. Stoll, C. Kenel, D. Polyzos, D. Havermann, W. N. MacPherson, H. Duncan P, C. Leinenbach, A. Spierings, K. Koenig-Urban and R. R. J. Maier, “Integrating fiber fabry-perot cavity sensor into 3-D printed metal components for extreme high-temperature monitoring applications,” *IEE Sensors Journal,* vol. 17, no. 13, pp. 4107 - 4114, 2017.

[19] T. G. Gawel, “Review of Additive Manufacturing Methods,” *Solid State Phenomena,* vol. 38, pp. 1-16, 2020.

[20] W. E. Frazier, “Metal Additive Manufacturing: A Review,” *Journal of Materials Engineering and Performance,* vol. 23, no. 6, pp. 1917-1928, 2014.

[21] T. G. Giallorenzi, “Optical fiber sensor Technology,” *Transactions of microwave theory and technoqies,* vol. 30, no. 4, pp. 472-511, 1982.

[22] F. Mitschke, Fiber Optics - Physics and Technology, Berlin: Springer, 2009.

[23] T. Patra, “Numerical Aperture of A Plastic Optical Fiber,” *International journal of innovations in engineering and technology,* vol. 2, no. 1, pp. 258-263, 2013.

[24] R. Paschotta, “Plastic Optical Fibres,” RP Photonics, 2021. [Online]. Available: https://www.rp-photonics.com/plastic_optical_fibers.html. [Accessed 09 04 2022].

[25] K.Bhowmik and G. Peng, “Polymer Optical Fibers,” in *handbook of Optical Fibers*, Singapore, Springer, 2019, pp. 1-51.

[26] C. Stabler, A. Reitz, P. Stein and B. Alrbert, “Thermal Properties of SiOC Glasses and Glass Ceramics at Elevated Temperatures,” *materials,* vol. 11, 2018.

[27] P.Dragic, T.hawkins and P.Foy, “Sapphire-derived all-glass optical fibres,” *nature Photonics,* vol. unspecified, no. unspecified, pp. 627-633, 2012.

[28] M. Busch, W. Ecke, I. Latka, D. Fischer, R. Willsch and H. Bertelt, “Inscription and Characterisaton of Bragg gratings in single-crystal sapphire optical fibres for high-temperature sensor applications,” *Measurement Science and Technology,* vol. 20, p. 6pp, 2009.

[29] J. Canning, M. Stevenson, S. Bandyopadhyay and K. Cook, “Extreme Silica Optical Fibre Gratings,” *Sensors,* vol. 8, pp. 6448-6452, 2008.

[30] G. R. Sinha, “Chapter 1 Introduction to sensors,” in *Advanced in Modern Sensors - Physics, design, simulation and applications*, IOP publishing, 2020, pp. 1-3.

[31] A. Barrias, J.R Casas, S. Villalba, “A Review of Distributed Optical Fiber Sensors for Civil Engineering Applications,” *Sensors,* vol. 16, no. 5, p. 748, 2016.

[32] A. Sachdeva, “Wavelength Division Multiplexing,” *International Journal of Advanced Research in Electronics and Communication Engineering,* vol. 5, no. 5, pp. 1516-1522, 2016.

[33] M. A. El-Aesser, “Time Divison Multiplexing and its Applicaiton in High Speed Optical Communication,” University of Connecticut , Connecticut, 2002.

[34] L. Hoffmann, “Applications of fibre optic temperature measurement,” *Proc. Estonian Acad. Sci. Eng,* vol. 13, no. 4, pp. 363-378, 2007.

[35] W. Hong-Hu Zhu, B.Shi, J. Yan, J. Zhang, B. Wang, “Fiber Bragg grating-based performance monitoring of a slope model subjected to seepage,” *Smart Materials and Structures,* vol. 23, no. 9, 2014.

[36] K. O. Hill, “Fibre Bragg Grating Technology Fundamentals and Overview,” *Journal of Lightwave Technology,* vol. 15, no. 8, pp. 1263-1276, 1997.

[37] National Instruments , “White papers - Fundamentals of Fiber Bragg Grating (FBG) Optical Sensing,” National Instruments , 22 01 2016. [Online]. Available: Fundamentals of Fiber Bragg Grating (FBG) Optical Sensing. [Accessed 29 03 2017].

[38] N. Singh, S.C Jain, R.P. Bajpai, “Fibre Bragg Gratings written using Phase Mask Tehnology,” *Journal of Scientific and industrial research,* vol. 64, pp. 108-115, 2005.

[39] G. Lee, K. Kalli, C. Koutsides, Z. Yan, D. Adebayo, “Femtosecond laser inscribed phase masks for fibre Bragg grating sensor inscription,” in *22nd International Conference on Optical Fiber Sensors*, Beijing, 2012.

[40] G.D. Marshall, R. J. Eilliams, N. Jovanovic, M. J. Steel, M. J. Withford, “Point-by-point written fiber-Bragg gratings and their application in complex grating designs,” *Optics Express ,* vol. 18, no. 19, pp. 19844-19859, 2010.

[41] S. Poeggel, D. Duraibabu, K. Kalli, G. Leen, G. Dooly, “Recent Improvement of Medical Optical Fibre Pressure and Temperature Sensors,” *Biosensors,* vol. 5, no. 3, pp. 432-449, 2015.

[42] D. Grobnic, C. Hnatovsky and S.Dedyulin, “Fiber Bragg Grating Wavelength Drift in Long-Term High Tempeerature Annealing,” *Sensors,* vol. 21, no. 1454, 2021.

[43] D. Havermann, J. Mathew, W. N. MacPherson, R. J. Maier, D. P. Hand, “Temperature and strain measurements with fiber bragg gratings embedded in stainless steel 316,” *Journal of Lightwave Technology,* 2014.

[44] C. E. Campanella, A. Cuccovillo, C. Campenella, A. Yurt and V. M. N. Passaro, “Fibre Bragg Grating Based Strain Sensors: Review of Technology and Applications,” *Sensors,* vol. 18, 2018.

[45] S. Capouillet, J. A. Smith, D. J Walter, G. S Glaesemann, G. E. Kohnke, “A Fiber Bragg grating Measurement System for Monitoring Optical Fibre Strain,” [Online]. Available: http://www.corning.com/media/worldwide/coc/documents/Fiber/RC-Fiber%20Mechanical%20Reliability/Mechanical_Reliablilty-Modeling/tr3680.pdf.

[46] J. Canning, “Fibre gratings and devices for sensors and lasers,” *Laser and Photonic Reviews,* vol. 2, no. 4, p. 275–289, 2008.

[47] S. J. Mihailov, “Fiber Bragg Grating Sensors for Harsh Environments,” *Sensors,* pp. 1898-1918, 2012.

[48] S.S. Chong, W. Y. Chong, S.W. Huran, H. Ahmad, “Regenerated fibre Bragg grating fabricated on high germanium concentration photosensitive fibre for sensing at high temperature,” *Optics and laser Technology,* vol. 44, pp. 821-824, 2012.

[49] Y. Lee, Z. Hua, Y. Feng, P. Gang, “Metal coating of fiber Bragg grating and the temperature sensing character after metallisation,” *Optical Fiber Technology,* vol. 15, p. Optical Fiber Technology, 2009.

[50] R. R. J. Maier, D. Hand, W.N. MacPherson, “Embedding metallic jacketed fused silica fibres into stainless steel using additive layer manufacturing technology,” in *Fifth European Workshop on Optical Fibre Sensors*, Krakow, 2013.

[51] J. Xie, “A study of the temperature sensitivity of fiber Bragg gratings after metallization,” *Smart Materials and Structures,* vol. 16, p. 1837–1842, 2007.

[52] AK Steel, “316/316L Stainless steel product data sheet,” AK Steel, 2007. [Online]. Available: http://www.aksteel.com/pdf/markets_products/stainless/austenitic/316_316l_data_sheet.pdf. [Accessed 21 02 2017].

[53] X. Li, “Metal Embedded Fiber Bragg Grating Sensors in Layered Manufacturing,” *Journal of Manufacturing Science and Engineering,* vol. 125, pp. 577-585, 2003.

[54] V. Bhavar, P. Kattire, V. Patil, S. Khot, “ A Review on Powder Bed Fusion Technology of Metal Additive Manufacturing,” Bharat Forge Ltd, Pune, unspecified.

[55] W. J. Sames, F. A. List, S. Pannala, R. R. Dehoff, S. S. Babu, “The metallurgy and processing science of metal additive manufacturing,” *International Materials Reviews,* pp. 1-46, 2016.

[56] K. V. Wong, A. Hernandez, “A Review of Additive Manufacturing,” *International Scholarly Research Network,* pp. 1-10, 2012.

[57] R. Poprawe, Tailoried Light 2: Laser Application Technology, Heidelberg: Springer, 2011.

[58] J. M. William M. Steen, Laser Material Processing, London: Springer, 2010.

[59] H. Gu, H. Gong, D. Pal, H. K. Rafi, “Influences of Energy Density on Porosity and Microstructure of Selective Laser Melted 174PH Stainless Steel,” J. B. Speed School of Engineering, University of Louisville, Louisville, 2013.

[60] I. Yadroitsev, A. Gusarov, I. Yadroitsava, I. Smurov, “Single track formation in selective laser melting of metal powders,” *Journal of Materials Processing Technology,* vol. 210, no. 12, pp. 1624-1631, 2010.

[61] C. Hauser, T. Childs, R. B. Eane, “Atmospheric Control during Direct Selective Laser Sintering of Stainless Steel 314S powder,” University ofLeeds School of Mechanical Engineering, Leeds, 1999.

[62] L. Murr, E. Martinez, J. Hernandez, S. Collins, “Microstructures and Properties of 17-4 PH Stainless Steel Fabricated by Selective Laser Melting,” *Journal of Materials Research and Technology,* vol. 1, no. 3, pp. 167-177, 2012.

[63] B. Zhou, J. Zhou, H. Li and F. Lin, “A study of the microstructures and mechanical properties of Ti6Al4V fabricated by SLM under vacuum,” *Materials science and engineering,* vol. 724, pp. 1-10, 2018.

[64] I. Yadroitsev, I. Yadroitsava, P. Bertrand, I. Smurov, “Factor analysis of selective laser melting process parameters and geometrical characteristics of synthesized single tracks,” *Rapid Prototyping Journal,* pp. 201-209, 2012.

[65] A. B. Spierings, G. Levi, “Comparison of density of stainless steel 316L parts produced with selective laser melting,” in *SFF Symposium* , 2008.

[66] I. Yadroitsev, I. Yadroitsava, P. Bertrand, I. Smurov, “Energy input effect on morphology and microstructure of selective laser melting single track from metallic powder in selective laser melting,” *Journal of Materials Processing Technology,* vol. 213, no. 4, pp. 606-613, 2013.

[67] I. Yadroitsev, I. Yadroitsava, P. Bertrand, I. Smurov, “Energy input effect on the microstructure,Energy input effect on the microstructure, morphology and stability of single track from morphology and stability of single track from metallic powder in selective laser melting,” 11 2012. [Online]. Available: http://www.afpr.asso.fr/content/assises/2012/actes/presentations/s5_6.pdf. [Accessed 02 2017].

[68] N. T. Aboulkhair, N. M. Everitt, I. Ashcroft, C. Tuck, “Reducing Porosity in AlSi10Mg Parts Processed by Selective Laser Melting,” *Additive manufacturing,* Vols. 1-4, pp. 77-86, 2014.

[69] American Iron and Steel Institute, A Designer's handbook (9002) Welding of Stainless Steels and Other Joining Methods, Nickel Development Institute.

[70] Multicore Solders, “Properties of Solders,” [Online]. Available: www.farnell.com/datasheets/315929.pdf. [Accessed 12 2017].

[71] Oerlikon, *An introduction to brazing - issue 4,* 2014.

[72] D. Schnee, “Principles of Brazing and Soldering,” Umicore.

[73] GH Induction Atmospheres - Turnkey Heating Solutions, “The Brazing Guide,” [Online]. Available: www.ghinduction.com/wp-content/uploads/2011/09/GH-Brazing-Guide1.pdf. [Accessed 11 2017].

[74] M. Way, J. Willingham and R. Goodall, “Brazing filler metals,” *Internal Materials Reviews,* vol. 65, no. 5, pp. 257-285, 2020.

[75] P. Stoll, J. Mathew, A. Spierings, T. Bauer, R. R. J. Maier and K. Wegener, “Embedding fibre optical sensors into SLM part,” in *Solid Freeform Fabrication 2016: Proceedings of the 26th Annual International Solid Freeform Fabrication Symposium – An Additive Manufacturing Conference* , Austin, 2016.

[76] British Standard, “Brazing - Part 2:Guide to brazing,” BSI, London, 1986.

[77] A.Lamikiz, A.Sánchez, L. d. Lacalle and J.L.Arana, “Laser polishing of parts built up by selective laser sintering,” *International Journal of Machine Tools and Manufacture,* vol. 47, no. 12, pp. 2040-2050, 2007.

[78] E. V. Bordatchev, A. M. K. Hafiz and O. R. Tutunea-Fatan, “Performance of laser polishing in finishing of metallic surfaces,” *International journal of advanced manufacturing technology,* vol. 73, pp. 35-52, 2014.

[79] E.Yasa, J.P.Kruth and J.Deckers, “Manufacturing by combining Selective Laser Melting and Selective Laser Erosion/laser re-melting,” *CIRP Annals,* vol. 60, no. 1, pp. 263-266, 2011.

[80] X. Song, W. Zhai, R. Huang, J. Fu, M. W. Fu and F. Li, “Metal-Based 3D-Printed Micro Parts & Structures,” in *Encyclopedia of Materials: Metals and Alloys*, Elsevier, 2022, pp. 448-461.

[81] “316L Stainless Steel Powders for Additive Manufacturing: Relationships of Powder Rheology, Size, Size Distribution to Part Properties,” *Materials,* vol. 13, 2020.

[82] Euroinox The european stainless steel development association, “Stainless Steels Tables of technical properties,” [Online]. Available: https://www.worldstainless.org/Files/issf/non-image-files/PDF/Euro_Inox/Tables_TechnicalProperties_EN.pdf. [Accessed 2021].

[83] “SCHOTT BOROFLOAT glass - floated borosilicate glass - technical data sheet,” 04 2012. [Online]. Available: https://www.advancedoptics.com/BOROFLOATTechnicalDataSheet.pdf. [Accessed 03 2022].

[84] R. Li, J. Liu, Y. Shi and L. Wang, “Balling behavior of stainless steel and nickel powder during selective laser melting process,” *International Journal of Advanced manufacturing technology,* vol. 59, pp. 1025-1035, 2012.

[85] E. Yasa, J. Deckers, T. Craeghs, M. Badrossamay and J.-P. Kruth, “Investigation on occurrence of elevated edges in selective laser melting,” *20th Annual International Solid Freeform Fabrication Symposium,* pp. 673-685, 2009.

[86] W. S. Gora, Y. Tian, A. P. Cabo, M. Ardron, R. R. Maier, P. Prangnell, N. J. Weston and D. P. Hand, “Enhancing Surface Finish of Additively Manufactured Titanium and Cobalt Chrome Elements Using Laser Based Finishing,” *Physics Procedia,* vol. 83, pp. 258-263, 2016.

[87] D. N. Aqilah, M. Sayuti and F. Yusof, “Effects of Process Parameters on the Surface Roughness of Stainless Steel 316L Parts Produced by Selective Laser Melting,” *Tesint and Evaluation,* vol. 46, no. 4, pp. 1673-1683, 2018.

[88] A. Laohaprapanon, “Study of optimized parameters of stainless steel 316 powder for rapid prototyping based on selective laser melting technique,” Prince of Songkla university, 2011.

[89] B. Li and T. Wang, “Selective Laser Melting of 316L Stainless Steel: Influence of Co-Cr-Mo-W Addition on Corrosion Resistance,” *Metals,* vol. 11, no. 597, 2021.

[90] T. Larimian, M. Kannan, D. Grzesiak, B. AlMangour and T. Borkar, “Effect of energy density and scanning strategy on densification, microstructure and mechanical properties of 316L stainless steel processed via selective laser melting,” *Materials Science and Engineering: A,* vol. 770, 2020.

[91] S. Greco, K. Gutzeit, H. Hotz, B. Kirsch and J. Aurich, “Selective laser melting (SLM) of AISI 316L—impact of laser power, layer thickness, and hatch spacing on roughness, density, and microhardness at constant input energy density,” *Advanced Manufacturing Technology,* vol. 108, pp. 1551-1562, 2020.

[92] F. Nürnberg, B. Kühn and K. Rollmann, “Metrology of Fused Silica,” in *Laser-Induced Damage in Optical Materials*, Boulder, 2016.

[93] D. Depla and J. Greene, “Chapter 5 - Sputter deposition processes,” in *Handbook of Deposition Technologies for Films and Coatings (Third Edition)*, William Andrew, 2010, pp. 253-296.

[94] D. Mattox, “Chapter 1 - Introduction,” in *Handbook of Physical Vapor Deposition (PVD) Processing (Second Edition)*, William Andrew, 2010, pp. 1-24.

[95] k. Kim, M. Park, W. Lee, J. Lee and C. Lee, “Effects of sputtering power on mechanical properties of Cr films deposited by magnetron sputtering,” *Materials Science and Technology ,* vol. 24, no. 7, pp. 838-842, 2008.

[96] S. Widodo, “Characterisation of Thin Film Nickel (Ni) deposited by sputtering method,” *International journal of innovative science, engineering and technology,* vol. 2, no. 9, pp. 380-385, 2015.

[97] Y. Mikami, K.Yamada, A. Ohnari and T. Degawa, “Effect of DC bias voltage on the deposition rate for Ni thin films by RF–DC coupled unbalanced-magnetron sputtering,” *Surface and Coatings Technology,* vol. 133, pp. 295-300, 2000.

[98] Y. Li, H. Zhang, Y. Feng and G. Peng, “A plating method for metal coating of fiber Bragg grating,” *CHINESE OPTICS LETTERS,* vol. 7, no. 2, pp. 115-117, 2009.

[99] S. Li, Y. Li, X. Liu, X. Li, T. Ding and H. Ouyang, “An In-Situ Electroplating Fabricated Fabry-Perot Interferometric Sensor and Its Temperature Sensing Characteristics,” *Coatings,* vol. 10, no. 12, pp. 1174-1187, 2020.

[100] I. Rose and C. Whittington, Nickel Plating Handbook, Nickel Institute , 2014.

[101] M. Schlesinger and M. Paunovic, “Electrodeposition of Nickel,” in *Modern Electroplating* , Pennington, New Jersey, John Wiley & Sons, 2000, pp. 139-200.

[102] D. Kopeliovich, “Nickel electroplating,” SubsTech -Substances and technologies, 14 12 2013. [Online]. Available: http://www.substech.com/dokuwiki/doku.php?id=nickel_electroplating#sulfate-chloride_solutions. [Accessed 05 2018].

[103] Corning, “Corning SMF 28 Ultra optical fibre - Product information,” Corning incorporated, New York, 2002.

[104] D. Kang and S. Park, “The signal characteristics of reflected spectra of fiber Bragg grating sensors with strain gradients and grating lengths,” *NDTE International ,* vol. 38, pp. 712-718, 2005.

[105] “Performance Evaluation of Fiber Bragg Gratings at Elevated Temperatures,” *NASA/TM,* no. 212888, 2004.

[106] Materion Brush performance alloys, “Tensile Testing,” Bursh Performance Alloys, 2011.

[107] M. Filograno and C. Chudla, “TEMPERATURE AND STRAIN EFFECTS DISCRIMINATION INTO COMPOSITE MATERIALS WITH EMBEDDED DUAL TYPE I-IA,” in *EUROPEAN CONFERENCE ON COMPOSITE MATERIALS*, Venice, 2012.

[108] INSTRON, “3400 SERIES - Universal Testing Systems for Tensile, Compression, and Flexure Testing,” Instron, [Online]. Available: https://www.instron.com/-/media/literature-library/manuals/3400-series/3400-dual-column-table-model-operator-guide.pdf. [Accessed 2022].

[109] E. Boateng and P. Schubel, “THERMAL ISOLATION TECHNIQUES FOR CURE MONITORING USING FBG OPTICAL SENSORS,” in *International conference on composite materials*, Edinburgh, 2009.

[110] R. E. Haimbaugh, “Chapter 2: Theory of Induction heating,” in *Practical induction heating*, Ohio, ASM International , 2001, pp. 5-10.

[111] J.Davies and P.Simpson, “Chapter 4 - Other applications of induction heating,” in *Induction Heating Handbook*, London, McGraw-Hill, 1979, pp. 96-108.

[112] T. Douglas and A.C.Victor, “Enthalpy and Specific Heat of Nine Corrosion-Resistant Alloys at High Temperatures,” *Journal of Research of the national Bureau of Standards -C. Engineering and Instrumentation,* vol. 65C, no. 1, pp. 65-69, 1961.

[113] Engineering Toolbox, “Permeability - Electromagnetism and formation of magnetic fields.,” 2016. [Online]. Available: https://www.engineeringtoolbox.com/permeability-d_1923.html. [Accessed 2022].